Analyzing the Size Effect on Fracture Toughness of Mortar through Flattened Brazilian Tests

By

Hao Kang

B.Sc. (Eng) in Civil Engineering

the University of Hong Kong, Hong Kong, China, 2014

Submitted to the Department of Civil and Environmental Engineering
in Partial Fulfillment of the Requirements for the Degree of

Master of Science in Civil and Environmental Engineering

at the

Massachusetts Institute of Technology

September 2015

Signature of Author: Signature redacted
Department of Civil and Environmental Engineering
August 17, 2015

Certified by: Signature redacted
Herbert H. Einstein
Professor of Civil and Environmental Engineering
Thesis Supervisor

Certified by: Signature redacted
John T. Germaine
Professor of Civil and Environmental Engineering, Tufts University
Thesis Supervisor

Approved by: Signature redacted
Heidi M. Nepf
Donald and Martha Harleman Professor of Civil and Environmental Engineering
Chair, Departmental Committee for Graduate Students

Analyzing the Size Effect on Fracture Toughness of Mortar through Flattened Brazilian Tests

By

Hao Kang

Submitted to the Department of Civil and Environmental Engineering on August 17, 2015 in Partial Fulfillment of the Requirements for the Degree of Master of Science in Civil and Environmental Engineering

ABSTRACT

Much research has been conducted on fracture toughness and there has been a debate about whether the fracture toughness varies with specimen size. The purpose of this research is to investigate the size effect on the fracture toughness of mortar specimens. First, the methods for calculating elastic modulus, tensile strength, and fracture toughness in previous research are discussed. Some of the fracture toughness calculation methods proposed in them are not convincing, since the underlying assumptions have not been verified by experiments. Then, the experimental setup, including the material properties, specimen preparation, and the testing apparatus, are introduced. The mortar specimens were cast from Type III Portland Cement, fine-grained silt, and water. Next, the numerical work on calculating the elastic modulus and the tensile strength is presented.

The experimental results are shown. 107 experimental results at different specimen sizes (two-inch, three-inch and four inch) and different flatness angles (23°, 28°, and 39°) were used to investigate how the elastic modulus E, tensile strength σ_t, averaged compressive stress at local maximum loading σ_A, and averaged compressive stress at local minimum loading σ_B change with size and 2α (flatness angle). The change of fracture toughness, based on the local maximum loading, K_{ICA}, and the local minimum loading, K_{ICB}, with size and 2α was analyzed. K_{ICA} and K_{ICB} appear to be independent of the specimen size; while σ_t, σ_A, and σ_B decrease with increasing specimen sizes. As for the effect of 2α, σ_t appears to be independent of 2α, while σ_A and σ_B decrease with increasing 2α. In addition, High speed videos and high resolution images indicate that the primary crack initiated at the specimen center, and propagated along the vertical center line.

Thesis Supervisor: Herbert H. Einstein

Title: Professor of Civil and Environmental Engineering

Thesis Supervisor: John T. Germaine

Title: Professor of Civil and Environmental Engineering, Tufts University

Acknowledgments

First and foremost, I would like to thank my advisor Professor John Germaine and Professor Herbert Einstein. Without their technical expertise and valuable guidance, my thesis would not have been possible. Their great passion, broad knowledge and rich experience was extremely beneficial to my research and coursework at MIT. Prof. Germaine led me into the flattened Brazilian tests and he was always there to help when I had problems. His rich experience in experiments and his great thoughts helped me overcome a lot of challenges and expedited my research progress. Prof. Einstein provided much critical thinking and valuable guidance, and my arguments and discussions became much more convincing. Both two professors spent a great amount of time modifying my thesis drafts. I would also like to express my gratitude to have the great opportunity to learn from Professor Andrew Whittle.

This thesis would also not have been possible without the help of Stephen Rudolph. I want to wholeheartedly thank Stephen Rudolph for helping me with every experiment. He was always there to help and he was always very generous with his time.

I would also like to thank Rock Mechanics Group – Stephen Morgan, Wei Li, Qiuyi Bing Li and Bruno Silva for their worthy advice and patient guidance. They were always willing to help me in the apparatus setup and numerical analyses.

Finally, I would like to thank my parents, who have been constantly supporting me through every step of my way and helping me to overcome many obstacles throughout the years.

Table of Contents

List of Figures

List of Tables

Chapter 1 Introduction

1.1 Motivation

Hydrocarbon extraction from oil and gas reservoirs, carbon dioxide sequestration, nuclear waste disposal, and underground construction require a comprehensive understanding of rock fracture processes, which include fracture initiation, fracture propagation and fracture coalescence. A comprehensive understanding of fracture processes relies on a detailed understanding of fracture toughness. Thus, fracture toughness has been extensively researched in the past and there has been a debate about whether the fracture toughness varies with specimen size. If fracture toughness is dependent on size it would not be a basic material property. Hence, the size effect on fracture toughness should be adequately researched experimentally.

1.2 Approach

Mortar was used to investigate the size effect on fracture toughness because it was relatively less time-consuming to prepare mortar specimens. The fracture toughness was determined through flattened Brazilian tests since it is relatively convenient to conduct the tests and is less prone to local failure near the loading surfaces (Wang and Xing, 1999; Wang et al., 2004; Keles and Tutluoglu, 2011; Agaiby, 2013). The detailed approaches are discussed in Chapter 2 (Background), Chapter 3 (Experimental Setup), Chapter 4 (Numerical Analysis) and Chapter 5 (Experimental Results and Discussion).

1.3 Objective

The purpose of this research is to verify whether the fracture toughness of mortar specimens varies with the specimen size.

1.4 Organization of thesis

The thesis is organized as follows:

- Chapter 2 – Background. The basic theories of fracture mechanics are reviewed first; this includes Linear Elastic Fracture Mechanics (LEFM), fracture process zone (FPZ), and Griffith theory. Then, conventional Brazilian tests and flattened Brazilian tests are compared, from the prospective of testing procedures, apparatus, analytical work and numerical work.
- Chapter 3 – Experimental Setup. This chapter first introduces the mortar specimen preparation and the flattening processes. It is followed by a description of the loading apparatus and the testing procedures.
- Chapter 4 – Numerical Analysis. This discusses how to determine the elastic modulus and the tensile strength of the specimen, based on the measurements.
- Chapter 5 – Experimental Results and Discussion. Experimental results are presented first. The discussion shows that the fracture toughness of the mortar specimen does **not** change much with specimen size.
- Chapter 6 – Conclusions and Recommendations.

Chapter 2 Background

This chapter presents a general review of basic fracture mechanisms and flattened Brazilian tests. First, fundamental concepts and equations of basic fracture theories (LEFM and Griffith Theory) are briefly discussed. Next, conventional Brazilian test and flattened Brazilian test are briefly described and compared.

2.1 Basic Fracture Theories

2.1.1 Fracture types and fracture processing

Anand (2014) defined fracture as the parting of the solid into two or more pieces. In rock mechanics, cracks are often used to represent small scale rock fractures. Based on failure mode, a crack can be classified as tensile crack or shear crack. In addition, Engelder (1987) classified cracks into three main categories based on crack size: microcracks, mesocracks and macrocracks. A microcrack extends 1 to 10^2 microns, a mesocrack extends hundreds of microns to few millimeters and a macrocrack extends several millimeters to decimeters (Engelder, 1987). In this research project, mortar samples underwent tensile failure so we will focus on tensile crack. Previous research has discovered that rock cracking is quasi-brittle (Irwin, 1961; Dungdale, 1960; Barenblatt, 1959). Anderson (2005) stated that there is a fracture process zone, where plasticity plays a significant role, ahead of the propagating crack tip. The fracture process zone consists of the tractional bridging areas and microcracking areas (See Figure 2.1). Microcracks occur before a macrocrack is formed. To introduce quasi-brittle rock fracture, it is important to introduce brittle failure first, followed by comments on the fracture process zone.

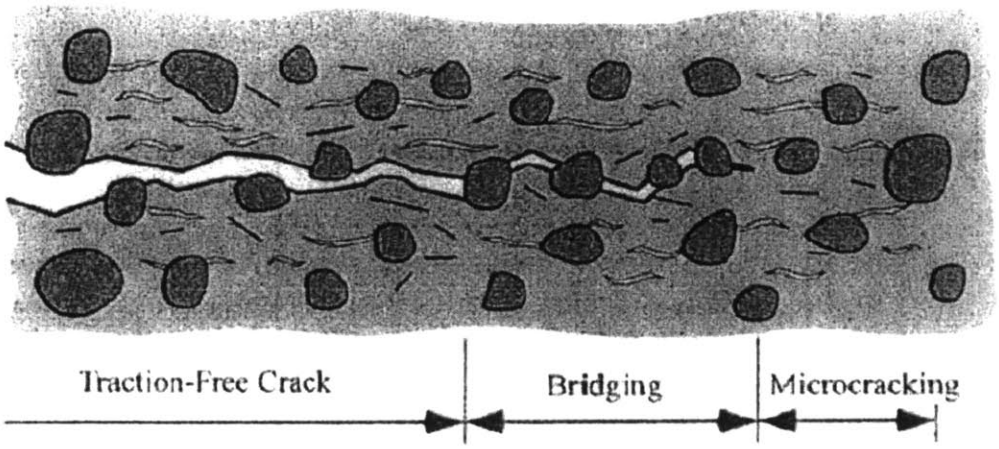

Figure 2.1 Fracture process zone ahead of a crack tip in concrete. The fracture process zone is characterized by tractional bridging and microcracking (Anderson, 2005)

2.1.2 Fracture modes

Irwin (1957) summarized fracture into three modes:

(1) Mode I, the tensile opening mode;

(2) Mode II, the shear mode (or the in-plane sliding mode);

(3) Mode III, the anti-plane tearing mode (or out of plane shear mode).

The three modes are illustrated in Figure 2.2.

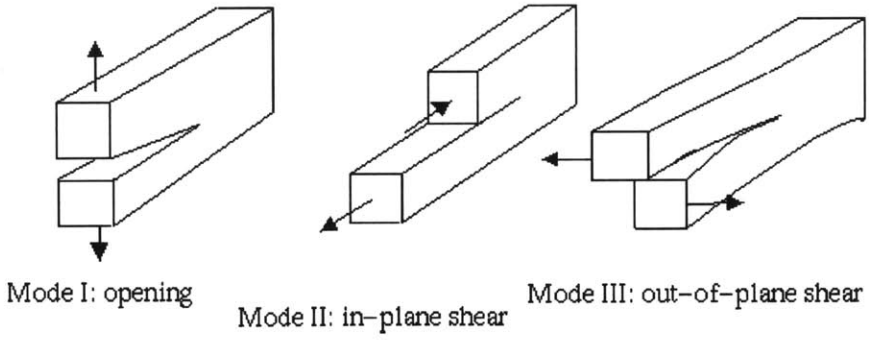

Figure 2.2 Different fracture modes (Whittaker et al., 1992)

2.1.3 Theoretical fracture strength

From an atomistic point of view, fracture involves separation of atomic planes. In dislocation, atomic planes glide past each other and result in shape changes. On the contrary, the fracturing process creates new free surfaces. Therefore, the theoretical fracture strength should be the stress required to simultaneously break all bonds across a plane. According to Anand (2014), theoretical fracture strength can be expressed as

$$\sigma_{theo} = \sqrt{\frac{E\gamma_s}{a_0}} \tag{2.1}$$

where E is the Elastic Modulus, a_0 is the lattice spacing (see Figure 2.3) and γ_s is the surface energy per unit area of the crystallographic cleavage plane. The detailed derivation is complicated so only the final equation is introduced.

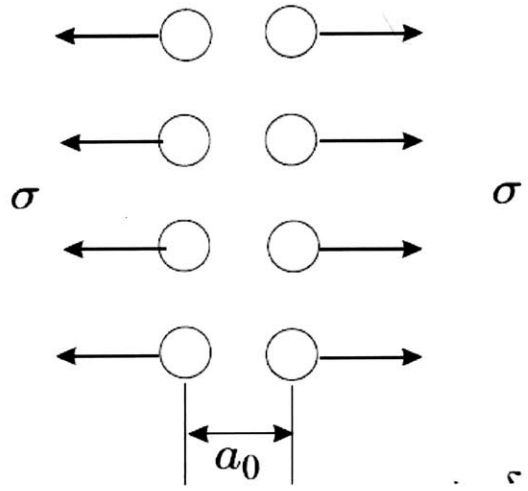

Figure 2.3 Atomistic point of view of fracture (Anand, 2014)

Anand (2014) stated that the specific energy γ_s of most solids is given to an adequate approximation by

$$\gamma_s \approx \frac{Ea_0}{100} \; to \; \frac{Ea_0}{10} \tag{2.2}$$

Substituting Equation 2.2 into Equation 2.1 gives

$$\sigma_{theo} = \frac{E}{10} \; to \; \frac{E}{3} \tag{2.3}$$

Equation 2.3 predicts the upper bound to the fracture strength of a perfect crystalline solid without any cracks. Based on equation 2.3, theoretical fracture strength of rocks and metals should be at GPa level, which is much higher than the measured fracture strength (the measured fracture strength is usually at the MPa level). This discrepancy is because that most rocks and metals contain intrinsic microcracks or crack-like micro-defects (Irwin, 1957; Evans, 2015; Anand, 2014). For a sharp crack or crack-like discontinuity, stress concentration can occur (Irwin, 1957; Demkowicz, 2012; Anand, 2014). The stress concentration can increase the local stress at the crack tip to the magnitude approaching σ_{theo} even though the applied far field tensile stress is very small compared with σ_{theo}. To predict the measured fracture strength, it is important to relate the applied far field tensile stress to local stress at the crack tip.

2.1.4 Macroscopic fracture criterion (Linear elastic fracture mechanics, LEFM)

Consider a sharp elliptical crack of major axis 2a and minor axis 2b ($a \gg b$), within an infinite plate and subjected a far field tensile stress σ_0 (See Figure 2.4). Kolosov (1907) and Inglis (1912) expressed local tensile stress at the crack tip as:

$$\sigma_{local} = \left(1 + 2\sqrt{\frac{a}{\rho}}\right)\sigma_0 \tag{2.4}$$

where ρ is the radius of curve at the crack tip ($\rho = \frac{b^2}{a}$).

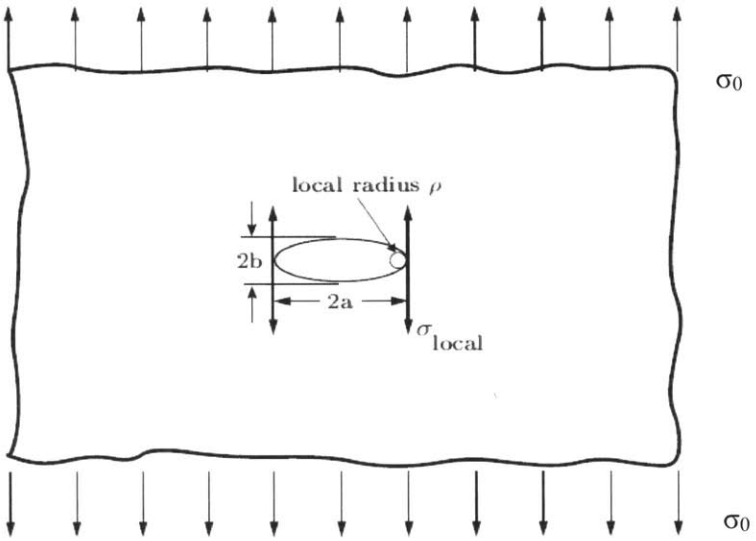

Figure 2.4 An elliptical crack in an infinite plate subjected to far field tensile stress σ_0 (Anand, 2014)

Anand (2014) pointed out that the sharpest physical crack would have a minimum crack tip radius of curvature of around the interatomic spacing (lattice spacing)

$$\rho_{min} \approx a_0$$

where a_0 is the lattice spacing (See Figure 2.3). Anand (2014) assumed that for the sharp crack, $a \gg a_0$ (for a very sharp crack, the crack length is normally much larger than the lattice spacing). Therefore, equation 2.4 becomes

$$\sigma_{local} = 2\sqrt{\frac{a}{a_0}}\sigma_0 \quad (a \gg a_0) \tag{2.5}$$

The local fracture criterion

$$\sigma_{local} \geq \sigma_{theo}$$

becomes

$$2\sqrt{\frac{a}{a_0}}\sigma_0 \geq \sigma_{theo} \tag{2.6}$$

Introduce

$$K_I = \sigma_0\sqrt{\pi a} \tag{2.7}$$

and

$$K_{IC} = \frac{\sigma_{theo}\sqrt{\pi a_0}}{2} \tag{2.8}$$

where K_I is called the mode I stress intensity factor (Irwin, 1957) and K_{IC} is called mode I critical stress intensity factor (Anand, 2014). Substituting Equation 2.7 and Equation 2.8 into Equation 2.6 gives

$$K_I \geq K_{IC} \tag{2.9}$$

For a sharp crack of length 2a within an infinitely wide and infinitely thick plate, $K_I = \sigma_0\sqrt{\pi a}$. Irwin (1957) stated that, for other geometrical configurations, in which the characteristic crack length is a and the characteristic applied far field tensile stress is σ_0, K_I can be expressed as

$$K_I = Q\sigma_0\sqrt{\pi a} \tag{2.10}$$

where Q is a dimensionless factor needed to account for geometry different from that of Figure 2.5. Q is called configuration correction factor and it is usually determined by relevant geometrical quantities (the geometrical quantities are referred as crack length, sample width, sample thickness, sample height, etc).

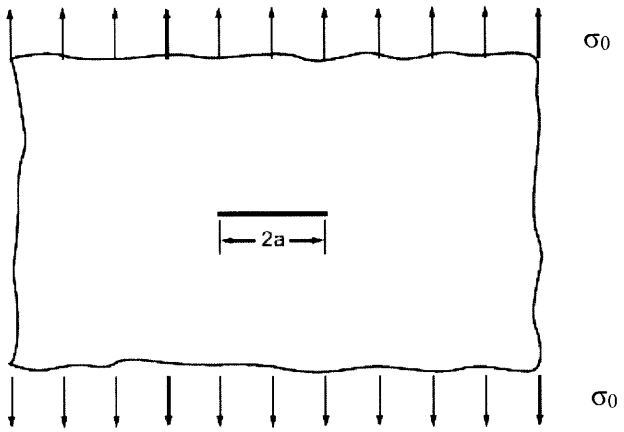

Figure 2.5. Sharp crack of length 2a within an infinite plate (Anand, 2014)

Therefore, the macroscopic failure criterion is that brittle fracture will occur if stress intensity factor K_I is larger than critical stress intensity factor K_{IC}. Mathematically, it can be expressed as

$$K_I \geq K_{IC} \tag{2.11}$$

where

- $K_I = Q\sigma_0\sqrt{\pi a}$ is called the mode I stress intensity factor. It is a function of sample geometry, applied far field tensile stress σ_0 and crack length a.
- K_{IC} is called the mode I critical stress intensity factor. It is also called fracture toughness and it measures the resistance of a material to crack propagation (Irwin, 1957).

Table 2.1 listed fracture toughness value of some typical materials.

Table 2.1 Some typical Mode I fracture toughness values (Whittaker et al., 1992; Zhang et al., 1998; Demkowicz, 2012)

Material	K_{IC} (MPa$\sqrt{m}$)
Epoxy	0.6
Oil Shale	0.6-1.1
Concrete	1.2
Basalt	1.8-3.0
PVC	3.4
Aluminum	24
Steel	66-120

2.1.5 Comments of macroscopic fracture criterion (LEFM)

The macroscopic fracture criterion defines the lower limit on K_{IC} since the plasticity within the fracture process zone is ignored. Demkowicz (2012) and Anand (2014) stated that plasticity makes it more difficult to create new free surfaces as plasticity absorbs a large amount of energy with crack initiation and propagation. Therefore, plasticity increases the fracture toughness. Since we neglect plasticity, the fracture toughness may be underestimated.

For brittle materials (i.e. ceramics, glasses), the inelastic deformation is negligible compared with elastic deformation so the macroscopic fracture criterion is reasonably accurate. On the contrary, for ductile material (i.e. metals, polymers), the inelastic deformation is significant and as a result,

the actual K_{IC} value is much larger than the elastic estimate of K_{IC} value predicted by Equation 2.8. Macroscopic fracture criterion is no longer applicable.

LEFM also has some other limitations. Consider a sharp crack within an infinite plate (See Figure 2.6). Based on LEFM, Westergaard (1939) and Muskhelisvili (1963) derived the equations of stress components near the crack tip:

$$\sigma_{RR} = \frac{\sigma\sqrt{\pi a}}{\sqrt{2\pi r}}\cos\frac{\theta}{2}\left(1 + sin^2\frac{\theta}{2}\right) \tag{2.12}$$

$$\sigma_{\theta\theta} = \frac{\sigma\sqrt{\pi a}}{\sqrt{2\pi r}}cos^3\frac{\theta}{2} \tag{2.13}$$

$$\sigma_{R\theta} = \frac{\sigma\sqrt{\pi a}}{\sqrt{2\pi r}}\sin\frac{\theta}{2}cos^2\frac{\theta}{2} \tag{2.14}$$

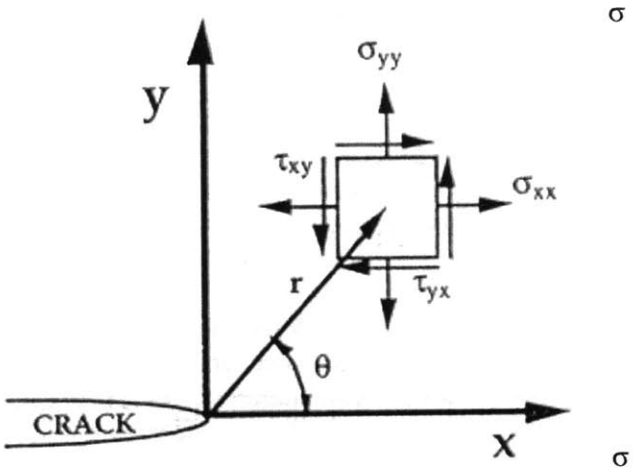

Figure 2.6 Coordinate system of a crack (Backers, 2004). It includes both Cartesian coordinates and cylindrical coordinates

Equations 2.12, 2.13 and 2.14 indicate that the stress near the crack tip will approach infinity if the distance to the crack tip r approaches zero, which is not realistic. Therefore, LEFM fails to predict the stress at the location, which is very near to the crack tip. Barenblatt (1959), Irwin (1960) and Dugdale (1960) postulated that stress very near the crack tip is the yield stress (an intrinsic material property) and the material undergoes plastic deformation. This zone is termed as the Fracture Process Zone (Irwin, 1960) and within this zone, the material deforms plastically. Fracture Process Zone and plastic deformation are very significant for ductile materials (i.e. metals and polymers).

Previous researches indicated that concrete and mortar can be referred to as a quasi-brittle material and plastic deformation is not negligible (Irwin, 1961; Dugdale, 1960; Barenblatt, 1959). Therefore, the plastic zone (fracture process zone) is introduced next.

2.1.6 Fracture process zone (plastic zone)

Irwin (1960) considered an elliptical crack (See Figure 2.6), and reformulated Equation 2.12, Equation 2.13 and Equation 2.14 in terms of polar coordinates:

$$\sigma_{ys} = \frac{K_I}{\sqrt{2\pi r}} f(\theta) \tag{2.15}$$

where K_I is the mode I stress intensity factor ($K_I = \sigma\sqrt{\pi a}$, see Equation 2.7), σ_{ys} is the yield stress and $f(\theta)$ is a function dependent on θ. When $\theta = 0$ (directly in front of the crack), $f(\theta) = 1$. Rearranging Equation 2.15 gives:

$$r_p = \frac{1}{2\pi}\frac{K_I^2}{\sigma_{ys}^2} \tag{2.16}$$

where r_p is the size of the fracture process zone. Here Irwin (1960) approximated the fracture process zone as a circular disc of radius r_p centered at the crack tip. Irwin (1960) stated that by assuming specimen yielding starts when stress σ reaches 88% to 115% of the material yield stress, the actual process zone size ranged from 80% to 130% of the r_p determined by Equation 2.16. Therefore, Equation 2.16 provides a reasonably accurate estimation of the process zone size.

Dugdale (1960) also determined the plastic zone size but with different assumptions than Irwin. Dugdale (1960) assumed that the crack is rectangular and that the material over a distance s beyond the crack would have yielded (See Figure 2.7 on the next page). After derivation, Dugdale (1960) expressed the size of the fracture process zone as:

$$r_p = \frac{\pi^2 T^2 l}{8\sigma_{yield}} \tag{2.17}$$

where T is the applied remote loading. Dugdale's theory is not applicable here because the cracks in flattened Brazilian tests are not rectangular.

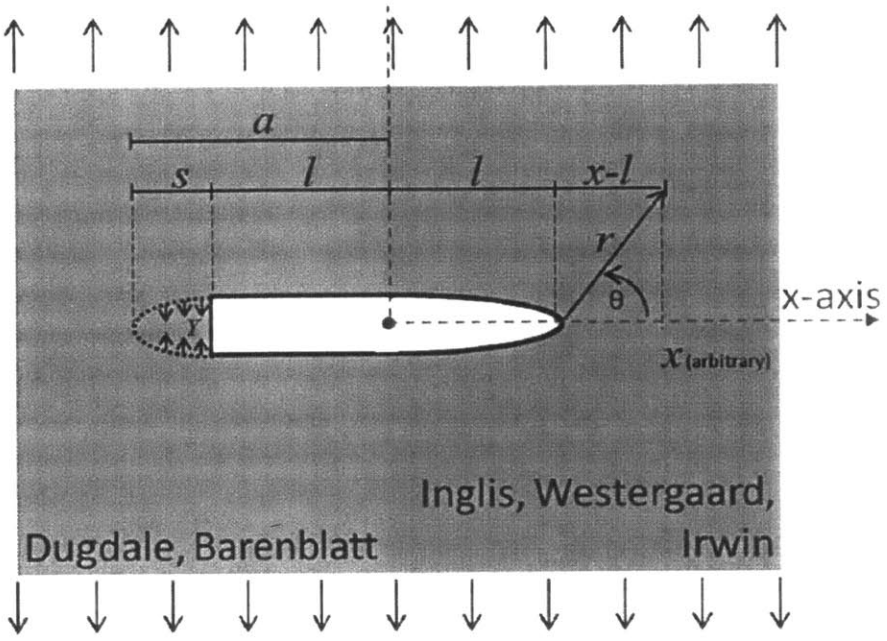

Figure 2.7 The crack shapes considered by Dugdale and Irwin (Brooks, 2013). The left side is Dugdale's model and the right side is Irwin's model.

2.1.7 Original Griffith Theory

Griffith (1921) proposed a thermodynamic criterion (energy-based criterion) for crack propagation in solids. The assumptions of Griffith Theory are summarized below:

1. All materials have a distribution of pre-existing cracks inside them and some cracks are oriented in a way that maximize the stresses at their tip.
2. As the applied stress increases, the stress at the tip of one pre-existing crack exceeds the theoretical strength of the pre-existing crack.
3. There are two energies that determine if a crack can propagate:
   a. Surface energy: fracture creates new surface area and this has a surface energy γ_s (per unit area) associated with it. Thus, increasing surface energy inhibits crack propagation.
   b. Potential energy: elastic energy stored inside the material and the external potential energy due to applied loads. Crack propagation releases the elastic stored energy so a decrease in elastic energy promotes crack propagation.

Griffith (1921) stated that if the rate of potential energy decrease exceeds the rate of surface energy increase, a crack will propagate. Mathematically, it can be expressed as

$$\frac{\partial}{\partial a}(\Delta u_{tot}) = \frac{\partial}{\partial a}(\Delta u_e + \Delta u_s) = \frac{\partial}{\partial a}\left(-\frac{\pi a^2 \sigma^2}{E'} + 4a\gamma_s\right) = -\frac{2\pi\sigma^2 a}{E'} + 4\gamma_S \leq 0 \qquad (2.18)$$

where

- $\Delta u_e = -\frac{\pi\sigma^2 a^2}{E'}$ = Stored elastic energy *and* (2.19)
- $\Delta u_s = 4a\gamma_s$ = Surface energy created by the crack (2.20)

where a is the crack half length in an infinite plate (See Figure 2.5), E' is the elastic modulus of the solid and γ_s is the specific surface energy. From Equation 2.19, Δu_e decreases when σ increases, indicating that increasing σ helps to release the stored elastic energy. Therefore, an increase in σ promotes crack propagation. Substituting Equation 2.19 and 2.20 into 2.18 gives

$$\sigma_{cri} = \sqrt{\frac{2E'\gamma_S}{\pi a}} \qquad (2.21)$$

2.1.8 Comments on original Griffith theory

Original Griffith theory (1921) neglected the inelastic deformation (in other words, only considered the elastic deformation) of the material around the crack front. For brittle materials (glass, ceramic) for which the inelastic deformation is negligible, the original Griffith theory provides excellent agreement with experimental data. On the contrary, for ductile materials (metals, polymers) for which inelastic deformation is significant, the original Griffith theory underestimates the tensile strength (inelastic deformation also absorbs energy during crack initiation and propagation). Thus, for ductile material, plastic deformation needs to be taken into account when we determine γ_s (See Equation 2.21).

Previous research (Irwin, 1961; Dugdale, 1960; Barenblatt, 1959) indicated that concrete and mortar can be referred to as a quasi-brittle material but original Griffith theory is still reasonably applicable. In addition, in flattened Brazilian tests mortar samples failed in tension.

Therefore, original Griffith theory forms the basis of tensile strength prediction and size effect explanation.

2.1.9 Size effect on tensile strength

It is also worth noting that based on Equation 2.21, for the same material, samples with larger crack length (larger flaw) have lower tensile strength. Previous research (Weibull, 1951; Glucklich and Cohen, 1967; Glucklich and Cohen, 1968; Einstein, 1970; Einstein, 1981; Demkowicz, 2012) proved that for the same material, larger samples have lower tensile strength compared with smaller samples (See Figure 2.8). The size effect can be explained by both extreme value theory (Epstein, 1948; Weibull, 1951) and stored strain energy theory (Glucklich and Cohen, 1967).

Extreme value theory (Epstein, 1948; Weibull, 1951) assumes a normal distribution of flaw sizes. The larger the specimen size, the more extreme values occur for the flaw size (both positive extreme values and negative extreme values) (Weibull, 1951). Therefore, larger specimens are more likely to contain larger flaws (Weibull, 1951) and according to Equation 2.21, larger flaws have less tensile strength. The material tensile strength is dependent on the weakest flaw (flaw which has the lowest strength) because it takes only one critical flaw for the entire specimen to fail even though other flaws are stable (Demkowicz, 2012). Thus, larger specimens are more likely to have lower tensile strength (Demkowicz, 2012).

Later, Glucklich and Cohen (1967, 1968) tested notched beams which had identical cross-section area but different lengths so the statistical effect was eliminated. However, they still found that tensile strength was decreasing with increasing specimen size and to explain this phenomenon, they proposed stored strain energy theory (Glucklich and Cohen, 1968). When cracks propagate, stored strain energy is released and it drives the crack propagation together with external work (Glucklich and Cohen, 1968). The larger the specimen size, the more stored strain energy is available (Glucklich and Cohen, 1968). As a result, the crack propagation is accelerated and the tensile strength is lowered (Glucklich and Cohen, 1968).

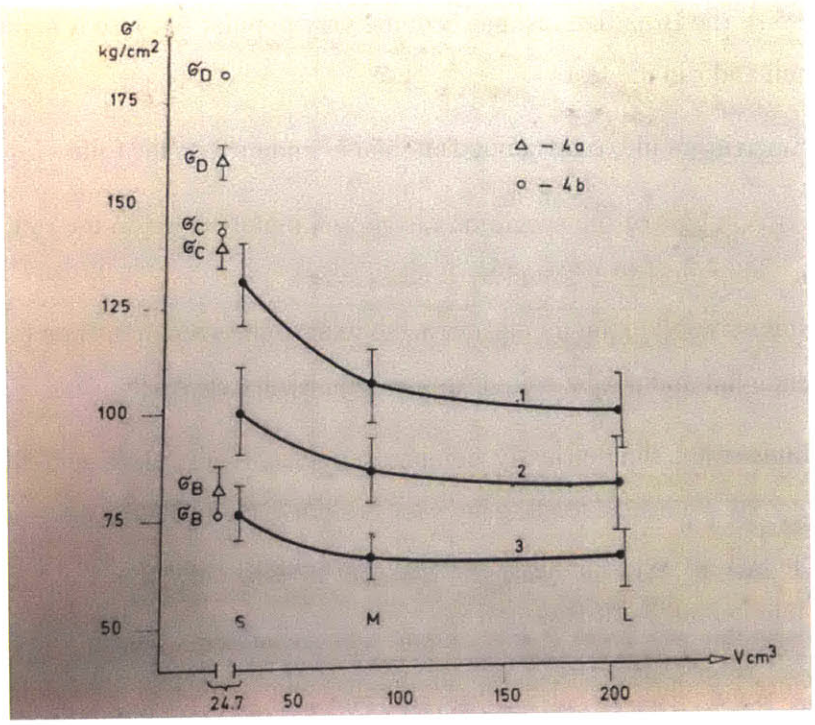

Figure 2.8 Tensile strength decreasing with increasing sample size (Einstein, Baecher and Hirschfeld, 1970)

2.2 Conventional Brazilian Tests and Flattened Brazilian Tests

In this section, the conventional Brazilian test and the flattened Brazilian test are described and compared, from the perspective of testing procedure (including apparatus), analytical work, and numerical work. In addition, the conventional Brazilian tests are compared with uniaxial extension tests.

2.2.1 Basic introduction and testing procedure

2.2.1.1 Conventional Brazilian test

The Brazilian test is a simple indirect testing method which is used to determine the tensile strength of brittle materials or quasi-brittle materials, such as rock and concrete. Since it was developed by Brazilian and Japanese scholars in 1940s (Akazawa 1943; Carneiro, 1943; Barcellos and Carneiro,

1953; Akazawa, 1953), the Brazilian test has become very popular because it is relatively easy to prepare the specimen and run the test.

First, the rock specimen is cut into right-angled circular cylinders with the following characteristics:

- The length (thickness) of the specimen t is approximately equal to the radius (D = 2t, see Figure 2.9). This ratio is suggested by ISRM (1978).
- Specimen sides smooth, straight and perpendicular to the specimen ends (see Figure 2.9).
- Specimen ends flat and perpendicular to the cylindrical axis.

Then, circular cylinders are diametrically compressed (See Figure 2.9), and the apparatus is illustrated in Figure 2.10. Two steel loading jaws are designed to contact the disc-shaped specimen at diametrically-opposed surfaces, and the arc of contact is approximately 10° (ISRM, 1978). The suggested loading rate is 200N/s (ISRM, 1978).

As illustrated in Figure 2.9, during the test the specimen center is under vertical compressive stress and horizontal tensile stress. As a result, the specimen undergoes tensile failure (tensile splitting), and the axial tensile crack should be the primary crack. ISRM (1978) stated that at primary failure, there will be a brief pause in the load increase. The load at primary failure should be recorded and the tensile strength can be determined correspondingly.

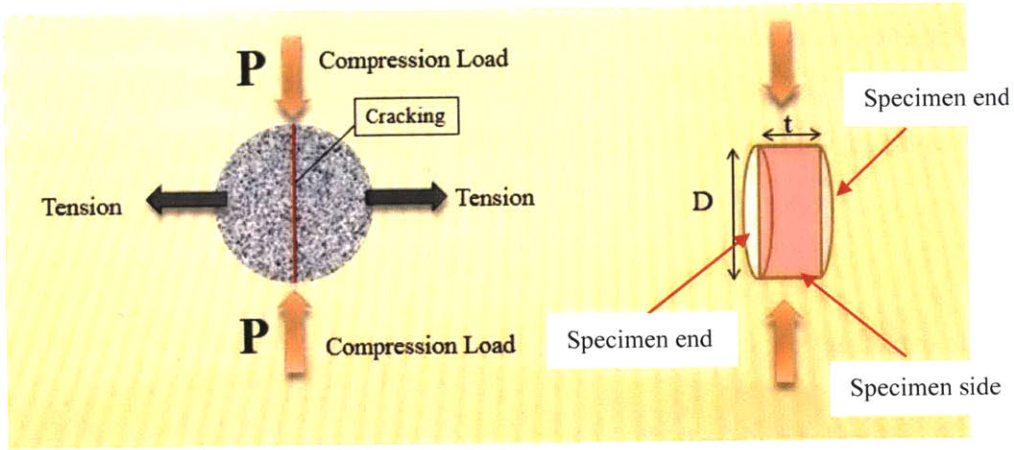

Figure 2.9 Conventional Brazilian tests (Guan, 2013)

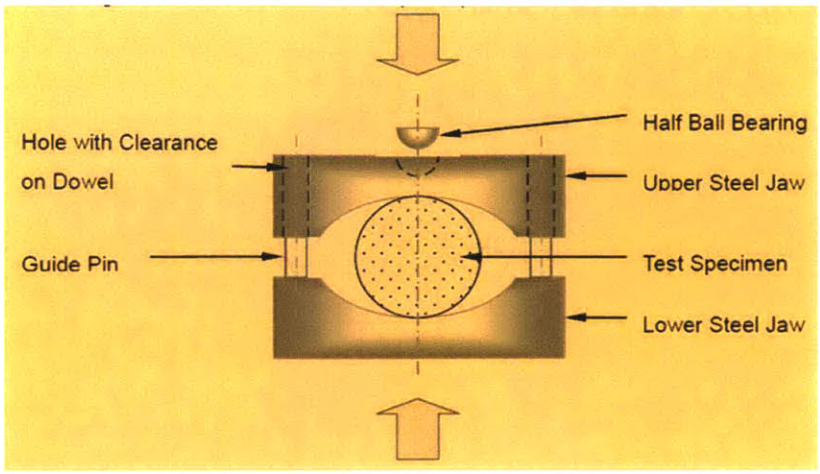

Figure 2.10 Apparatus of conventional Brazilian tests (Guan, 2013)

In conventional Brazilian tests, the applied loading may not be a line load (Yang, 2012; Guan, 2013). As a result, shear or crushing failure near the loading point may occur before the primary tensile crack, and the specimen should be discarded in this case (this will be explained in Section 2.2.6.1). In addition, ISRM (1978) stated that the maximum horizontal tensile stress occurs along the vertical center line (see the red line on the left side of Figure 2.9). Therefore, the primary crack should initiate on the vertical center line and propagate along the vertical center line. If the primary tensile crack initiates at the specimen periphery, or does not propagate approximately parallel to the vertical center line, the specimen should be rejected (ISRM, 1978).

2.2.1.2 Flattened Brazilian test

Wang and Xing (1999) first proposed flattened Brazilian test. By running one test, the elastic modulus E, tensile strength σ_t, and fracture toughness K_{IC} of the specimen can be obtained (How to determine those parameters will be discussed in Chapter 2.2.2 and Chapter 2.2.3). Different from conventional Brazilian tests, two parallel planes of equal width are introduced on the Brazilian disc (See Figure 2.11). First, cylindrical discs are cut according to the specimen requirements of conventional Brazilian tests (see Chapter 2.2.1.1). Then, two parallel flattened surfaces, with a flatness angle of 2α (see Figure 2.11), are cut.

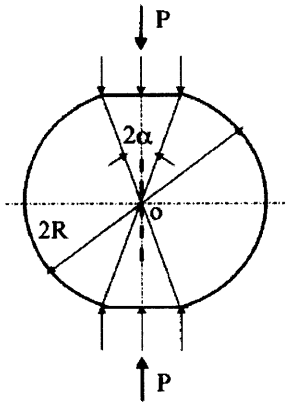

Figure 2.11 Flattened Brazilian test. P is the summation of distributed loading and the dashed line represents the primary crack. (Wang and Xing, 1999)

During the test, the applied loading P is distributed through a loading plate to the flattened surface (see Figure 2.11). Wang and Xing (1999) stated that, similar to the conventional Brazilian test, in the flattened Brazilian test the specimen center is under vertical compressive stress and horizontal tensile stress. The primary crack initiates at the sample center and propagates along the vertical center line (the dashed line, see Figure 2.11).

In flattened Brazilian tests, a curved steel jaw is no longer required since the surface is flattened. Only four papers discuss experimental analysis of flattened Brazilian tests but none of them discusses the apparatus. It is assumed that the basic equipment is a loading frame, two loading plates, extensometers and a data acquisition system. As for the loading rate, only Wang and Wu (2004) suggested that the loading should be displacement controlled (constant displacement rate), but they did not recommend a specific displacement rate. The testing procedure can be divided into three stages, as illustrated in Figure 2.12.

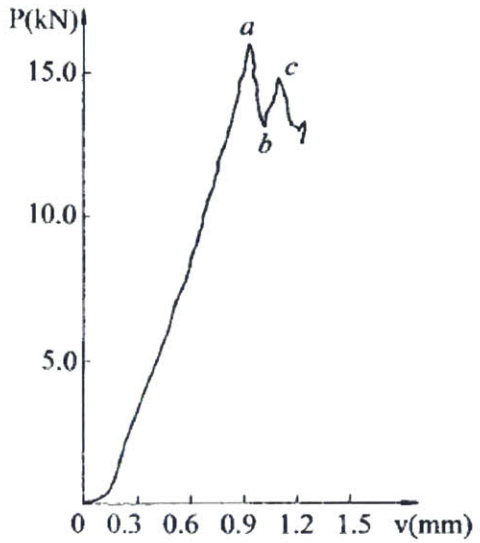

Figure 2.12 A typical load displacement curve (Wang and Xing, 1999)

Stage 1 corresponds to segment oa in Figure 2.12. The applied loading starts from zero to a local peak loading (point a). When the specimen is vertically compressed, the specimen center is under horizontal tensile stress, which is similar to conventional Brazilian tests (Wang et al., 2004) (See Figure 2.13). Wang et al. (1999) stated that when the loading reaches point a, a tensile crack initiates at the specimen center since the horizontal tensile stress is maximum at the center (this will be explained later). The stress at point a is used to determine the tensile strength because it is the stress required to initiate the tensile crack (Wang et al., 2004). In addition, the specimen deforms linearly in stage 1 and the average slope of segment oa is used to calculate the specimen elastic modulus (Wang et al., 2004).

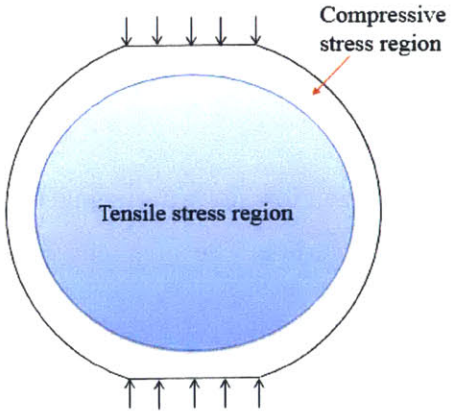

Figure 2.13 Stress distribution within the specimen in flattened Brazilian tests (the boundary is sketched roughly)

Stage 2 corresponds to segment ab in Figure 2.12 and the primary tensile crack (initiated at point a) grows at this stage. The displacement rate is kept the same throughout the test. The loading drop is caused by the crack propagation. Wang et al. (2004) stated that the horizontal tensile stress is the largest along the vertical center line (See Figure 2.14). Therefore, the crack propagates along the center line from the center to the location where the tensile stress intensity at the crack tip is equal to the specimen fracture toughness (See Figure 2.15). Beyond that location, the stress intensity is smaller than the specimen fracture toughness and the crack cannot propagate (the horizontal tensile stress is decreasing when it becomes closer to the flattened surface). The crack propagation causes the loading to drop and the loading reaches the local minimum loading (point b) when the crack propagation stops. Wang et al. (2004) assumed that the primary tensile crack starts to propagate from the crack tip when the loading is very close to the loading at point b so therefore, the loading at point b is used to calculate the fracture toughness. This argument is disputable because whether the crack starts to propagate near point b has *not* been verified by experiments. How to calculate the fracture toughness will be explained in detail in Section 2.2.3.

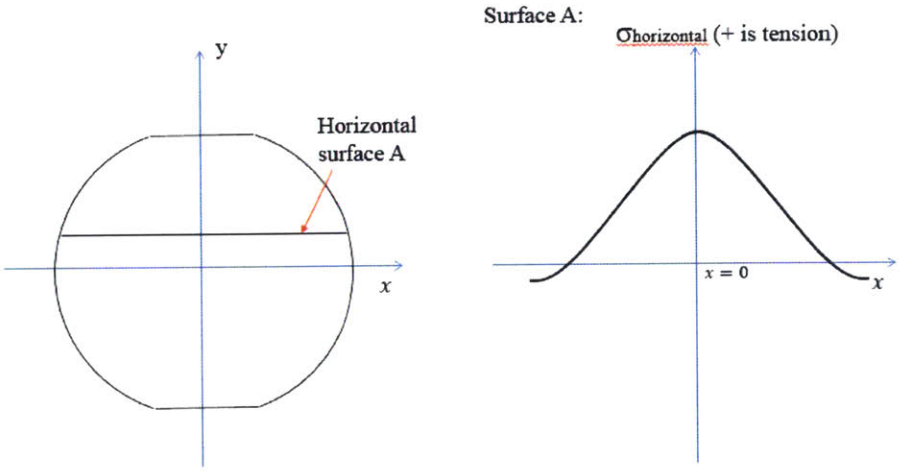

Figure 2.14 Horizontal stress distribution along horizontal surface A. The maximum tensile stress occurs in the centerline. The stress curve is sketched roughly.

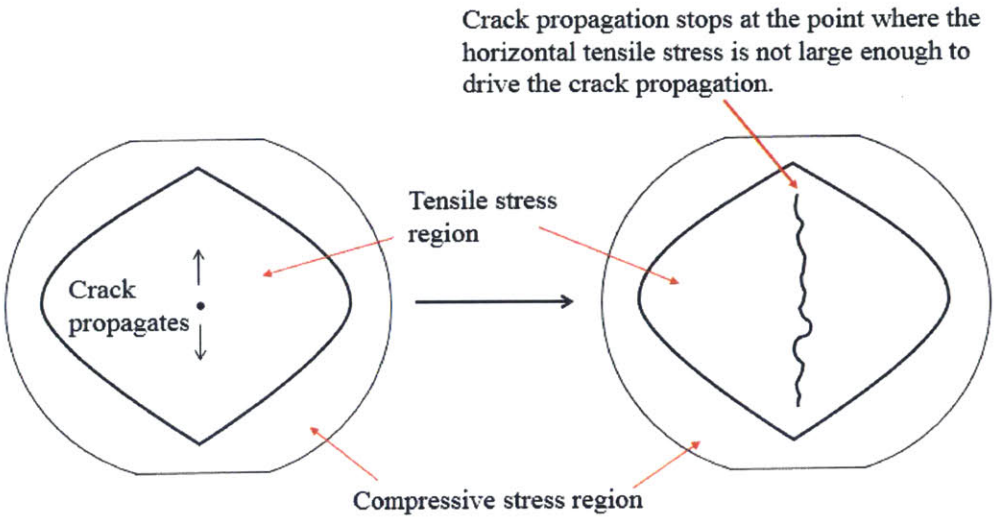

Figure 2.15 Tensile crack propagation. The crack shape and the boundary between tensile stress and compressive stress are sketched roughly

Stage 3 corresponds to segment bc and the primary crack propagation has stopped. Wang and Wu (2004) stated that the specimen undergoes tensile total failure at point c and the loading at point c should be smaller than the loading at point a. However, their statement is considered to be wrong. In the real test, at stage 3 the specimen undergoes compressive total failure and the loading at point c should be larger than the loading at point a. This will be explained in detail in Chapter 5.

2.2.2 Analytical work with conventional Brazilian tests and flattened Brazilian tests

2.2.2.1 Conventional Brazilian test

By assuming that the specimen is under uniformly distributed tensile stress (see Figure 2.16), Carneiro (1953) and Barcellos (1953) stated that the tensile strength can be expressed as:

$$\sigma = \frac{2P}{\pi Dt} \tag{2.22}$$

where P is the applied loading when the specimen fails, D is the cylinder diameter, t is the specimen length (thickness) (see Figure 2.9). Equation 2.22 is used to calculate the tensile strength.

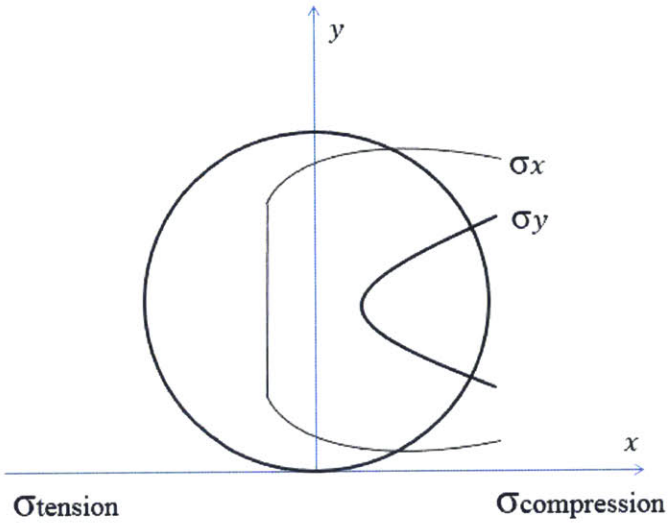

Figure 2.16 Stress distribution of conventional Brazilian tests

2.2.2.2 Flattened Brazilian test

Wang et al. (2004) proposed an analytical formula to calculate the tensile strength. The detailed derivation is presented below.

Hoek and Brown (1980) reinterpreted Griffith's criterion (1924). Some conventional triaxial tests had been done on rock specimens and an empirical Mohr's envelope was plotted. The Mohr's envelope is approximately parabolic (see Figure 2.17) and mathematically, the parabolic curve can be expressed as:

$$\sigma_3 = -T_0\,, \qquad \text{if } \sigma_1 + 3\sigma_3 < 0 \tag{2.23}$$

$$\frac{(\sigma_1-\sigma_3)^2}{8(\sigma_1+\sigma_3)} = T_0, \qquad \text{if } \sigma_1 + 3\sigma_3 > 0 \tag{2.24}$$

where σ_1 is the maximum principal stress, σ_3 is the minimum principal stress and T_0 is the magnitude of the tensile strength (so T_0 is positive). Compressive stress is considered to be positive.

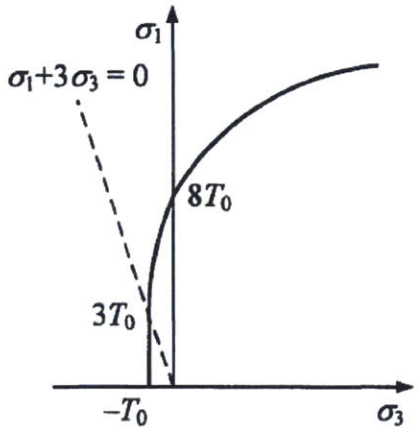

Figure 2.17 The empirical parabolic Mohr's envelope for the Griffith-based criterion (Pei, 2008)

In cylindrical system, the stress inside the sample can be expressed by σ_θ and σ_r (see Figure 2.18). Wang et al. (2004) assumed that there is no shear stress in the direction of σ_θ and σ_r. They also carried out finite element analysis (it will be discussed in detail in Section 2.2.3), and the analysis indicated that σ_θ is always smaller than σ_r. Thus, $\sigma_\theta = \sigma_3$ and $\sigma_r = \sigma_1$. Wang et al. (2004) also stated that their analysis results showed that $\sigma_r + 3\sigma_\theta > 0$. Therefore, and according to equation 2.24, the tensile strength can be expressed as

$$\frac{(\sigma_r-\sigma_\theta)^2}{8(\sigma_r+\sigma_\theta)} = T_0 \tag{2.25}$$

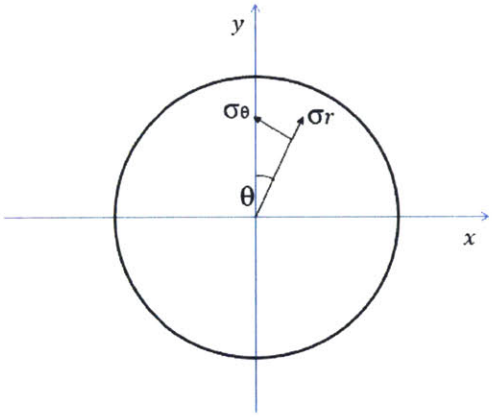

Figure 2.18 Illustration of σ_θ and σ_r

To determine T_0, Wang et al. (2004) derived approximate formulae for σ_θ and σ_r and they assumed that the crack initiates at the specimen center. Wang et al. (2004) expressed a pair of differential forces (see F on the left side of Figure 2.19) applied on the circular boundary (see Figure 2.19) as:

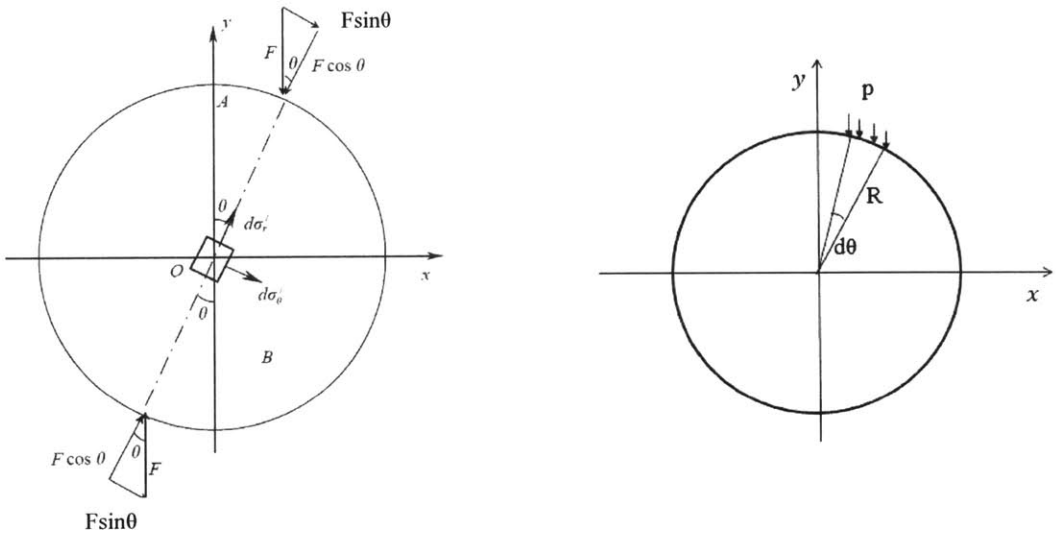

Figure 2.19 The differential stresses caused by a pair of differential forces (Wang et al., 2004)

$$F = pRd\theta = p\left(\frac{D}{2}\right)d\theta \tag{2.26}$$

where D is the diameter, p is the stress, dθ is the differential angle, and F is the summation of the stress p along the arc (see the right side of Figure 2.19, F is the load *per unit thickness*).

Decompose the F into a radial compressive force Fcosθ and a tangential shear force Fsinθ (See Figure 2.19). From Figure 2.19, Fcosθ is pointing to the specimen center so it is a radial compressive force; Fsinθ is tangential to the circular specimen so it is a tangential force. Timoshenko and Goodier (1970) stated that when a Brazilian disc is subjected to a radial compressive force, the stress solution on the loading diameter can be expressed as:

$$\sigma_\theta = -\frac{2P}{\pi Dt} \tag{2.27}$$

$$\sigma_r = \frac{2P}{\pi Dt}\left(\frac{4D^2}{D^2-4r^2} - 1\right) \tag{2.28}$$

where P is the radial compressive force, D is the specimen diameter, t is the specimen thickness and r is the distance to the specimen center. At the specimen center, r = 0. Wang et al. (2004) stated

that from Figure 2.19, Fcosθ is the radial compressive force per unit thickness, so P = Ftcosθ. Substituting P = Ftcosθ into equation 2.27 and 2.28 gives:

$$\sigma_\theta = -\frac{2F\cos\theta}{\pi D} \tag{2.29}$$

$$\sigma_r = \frac{6F\cos\theta}{\pi D} \tag{2.30}$$

Wang et al. (2004) then took the second order derivative of σ_θ and σ_r based on Equation 2.29 and 2.30. $d\sigma'_\theta$ and $d\sigma'_r$ (see the left side of Figure 2.19) are obtained and can be expressed as:

$$d\sigma'_\theta = -\frac{2F\cos\theta}{\pi D} \tag{2.31}$$

$$d\sigma'_r = \frac{6F\cos\theta}{\pi D} \tag{2.32}$$

Wang et al. (2004) also stated that the stresses along the center line (y axis, see Figure 2.19) is the most important because theoretically, the crack propagates along it. The stress components expressed in Equation 2.31 and 2.32 were rotated as illustrated in Figure 2.20 (Wang et al., 2004).

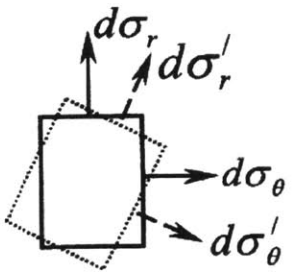

Figure 2.20 Transformation of stress components (Wang et al., 2004)

Taking y axis (see Figure 2.19) as the new radial direction so σ_r is the radial stress and σ_θ is the tangential stress. Wang et al. (2004) integrated $d\sigma'_\theta$ and $d\sigma'_r$ into $d\sigma_\theta$ and $d\sigma_r$ as

$$d\sigma_\theta = \left(\frac{6\cos\theta sin^2\theta}{\pi D} - \frac{2\cos\theta cos^2\theta}{\pi D}\right)F \tag{2.33}$$

$$d\sigma_r = \left(\frac{6\cos\theta cos^2\theta}{\pi D} - \frac{2\cos\theta sin^2\theta}{\pi D}\right)F \tag{2.34}$$

Then, Wang et al. (2004) made an approximation $F \approx pdx$ (see the x axis Figure 2.21), where p is the pressure and x represents the horizontal position on the flattened surfaces. At the vertical center line, x = 0. Therefore,

$$\cos\theta = \sqrt{1 - ({}^{x}/_{R})^{2}} \tag{2.35}$$

$$\sin\theta = {}^{x}/_{R} \tag{2.36}$$

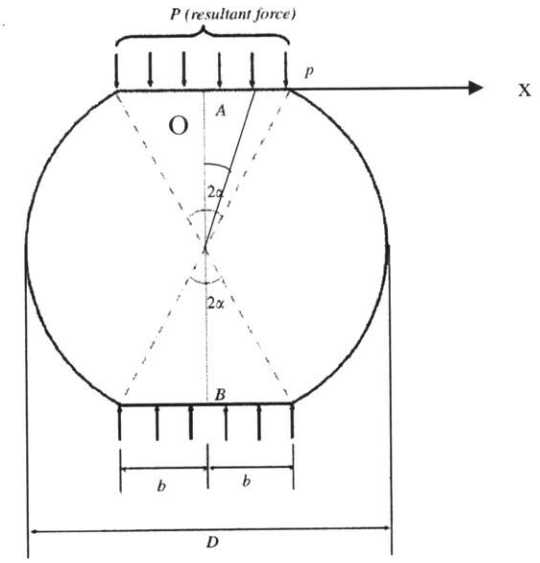

Figure 2.21 Specimen subject to a uniform diametric loading (Wang et al., 2004)

Substituting Equation 2.35 and 2.36 into Equation 2.33 and 2.34 gives:

$$d\sigma_{\theta} = \frac{2F}{\pi D}\left(\frac{3x^{2}\sqrt{1-({}^{x}/_{R})^{2}}}{R^{2}} - (1 - (\frac{x}{R})^{2})^{3/2}\right) \tag{2.37}$$

$$d\sigma_{r} = \frac{2F}{\pi D}\left(3\left(1 - \left(\frac{x}{R}\right)^{2}\right)^{\frac{3}{2}} - \frac{x^{2}\sqrt{1-({}^{x}/_{R})^{2}}}{R^{2}}\right) \tag{2.38}$$

Wang et al. (2004) then integrated Equation 2.37 and 2.38 for x in the interval (-b, b):

$$\sigma_{\theta} = \int_{-b}^{b} d\sigma_{\theta}dx = -\frac{2F}{\pi D}(1 - \left(\frac{b}{R}\right)^{2})^{3/2}\frac{\sin^{-1}({}^{b}/_{R})}{{}^{b}/_{R}} \tag{2.39}$$

$$\sigma_r = \int_{-b}^{b} d\sigma_r dx = \frac{2F}{\pi D}\left(\left(1-\left(\frac{b}{R}\right)^2\right)^{\frac{3}{2}} + \sqrt{1-\left(b/R\right)^2} + \frac{b/R}{\sin^{-1}(b/R)}\right)\frac{\sin^{-1}(b/R)}{b/R} \quad (2.40)$$

Wang et al. (2004) replaced b by α: $\sin\alpha = b/R$ and $\cos\alpha = \sqrt{1-(b/R)^2}$. In addition, since F is the load per unit thickness, P = Ft (P is the total load and t is the thickness) (Wang et al., 2004). Therefore, Equation 2.39 and 2.40 become:

$$\sigma_\theta = -\frac{2P}{\pi Dt}cos^3\alpha\frac{\alpha}{\sin\alpha} \quad (2.41)$$

$$\sigma_r = \frac{2P}{\pi Dt}\left(cos^3\alpha + \cos\alpha + \frac{\sin\alpha}{\alpha}\right)\frac{\alpha}{\sin\alpha} \quad (2.42)$$

Wang et al. (2004) substituted Equation 2.41 and 2.42 into Equation 2.25. Thus, T_0 is expressed as:

$$T_0 = \frac{2P}{\pi Dt}\left[\frac{(2cos^3\alpha + \cos\alpha + \sin\alpha/\alpha)^2}{8(\cos\alpha + \sin\alpha/\alpha)}\frac{\alpha}{\sin\alpha}\right] \quad (2.43)$$

Wang's method makes it convenient to calculate the tensile strength but this method is limited to samples with 2α values smaller than 30°. In the derivation, an approximation $F \approx pdx$ was made. According to Wang et al. (2004), this approximation is invalid when θ (See Figure 2.18) is not small. Wang et al. (2004) stated that when θ is larger than 15° (which means the 2α value is larger than 30°), the approximation is invalid and as a result, Equation 2.35 is not accurate. Therefore, Wang's method is only applicable when 2α value is smaller than 30°.

2.2.3 Numerical work of flattened Brazilian test

2.2.3.1 Elastic modulus

Wang et al. (2004) conducted numerical analysis on elastic modulus, and the only available numerical solution of elastic modulus was proposed.

The 'ANSYS' software was used to determine the elastic modulus. Several numerical analyses with different sample sizes and different sample geometries were run and the empirical equation was obtained by curve fitting:

$$E = \frac{2P}{\pi \Delta w t}\left[(1-\mu) - ln\left(1 + \frac{4}{(\sin\alpha)^2}\right)\right]\frac{\alpha}{\sin\alpha} \tag{2.44}$$

where E is the elastic modulus, P is the applied loading, Δw is the end-to-end displacement of the sample, t is the specimen thickness, μ is the Poisson's ratio, $\sin\alpha = 2b/D$ (2b is the width of flat surface and D is the specimen diameter, see Figure 2.21).

Equation 2.44 is not applicable in this research project. During the test it was very difficult to measure the end-to-end displacement because it was almost impossible to install extensometers near the flattened surfaces. The machine reading was also not the end-to-end displacement because the machine reading included the compressive displacement of the loading plate and the hydraulic jack. Actually, the extensometers were installed in other positions (See Section 3.4.2) and additional numerical analysis was conducted to determine the elastic modulus from the extensometer readings (See Chapter 4).

2.2.3.2 Tensile strength

Wang et al. (2004) not only derived analytical formula for tensile strength but also carried out numerical analysis. They used the 'ANSYS' software to determine σ_θ and σ_r along the y axis of the specimen (see Figure 2.18), and the flatness angle 2α varied from 5° to 30°. The simulation results indicated that σ_θ is always smaller than σ_r, and $\sigma_r + 3\sigma_\theta > 0$. Therefore, from Equation 2.25, the tensile strength can be expressed as

$$\frac{(\sigma_r - \sigma_\theta)^2}{8(\sigma_r + \sigma_\theta)} = T_0,$$

Where T_0 is the magnitude of the tensile strength.

In flattened Brazilian tests, the primary tensile crack should initiate at the specimen center, and Wang et al. (2004) analyzed the central crack initiation condition. They introduced a new parameter σ_G and they expressed σ_G as:

$$\frac{(\sigma_r-\sigma_\theta)^2}{8(\sigma_r+\sigma_\theta)} = \sigma_G = T_0 \tag{2.45}$$

Wang et al. (2004) stated that σ_G must reach a maximum value at the specimen center to produce the central crack initiation. They used Equation 2.45 to calculate σ_G along the y axis based on their results of σ_θ and σ_r, and the result of σ_G is plotted in Figure 2.22 below.

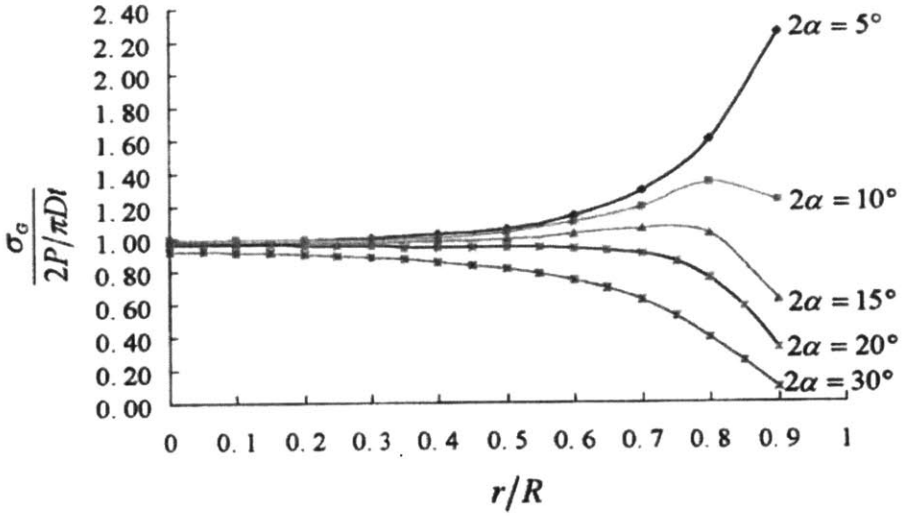

Figure 2.22 Numerical simulation results of σ_G (Wang et al., 2004). r is illustrated in Figure 2.23.

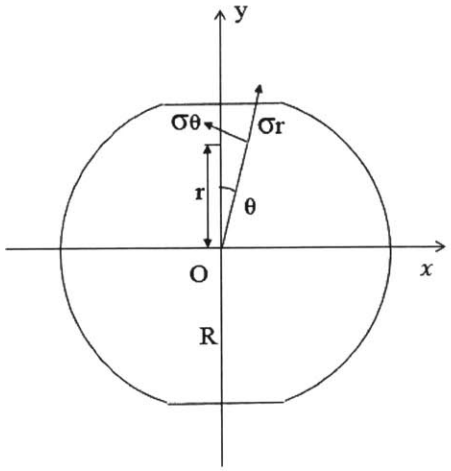

Figure 2.23 Illustration of r.

The vertical axis represents the dimensionless stress ($\frac{\sigma_G}{2P/\pi Dt}$), where P is the applied load, D is the specimen diameter and t is the specimen thickness. The horizontal axis represents the distance between a point on y axis and the specimen center (see r in Figure 2.23). In the simulation, they tried different 2α (flatness angle) values. For each 2α value, P, D, and t were kept constant. r was increased from 0 (the specimen center) to 0.9R and by changing r, different σ_G values were obtained. From Figure 2.22, when 2α is equal or larger than 20°, $\frac{\sigma_G}{2P/\pi Dt}$ reaches maximum value when r = 0, which means that σ_G reaches maximum value at the specimen center. Therefore, Wang et al. (2004) stated that when 2α is equal or larger than 20°, the primary tensile crack will initiate at the specimen center.

Based on Wang's results (2004), when 2α is very small (i.e. 5° and 10°), the maximum stress does not occur at the specimen center. This is similar to the results reported by Trollope and Brown (1965). Trollope and Brown (1965) stated that for conventional Brazilian tests, the maximum stress occurs on the compressive diametrical line but is away from the specimen center. Wong and Li (2013) carried out numerical analyses, and the results are in excellent agreement with Trollope's statement. The numerical results of Wong and Li (2013) are illustrated in Figure 2.24 below.

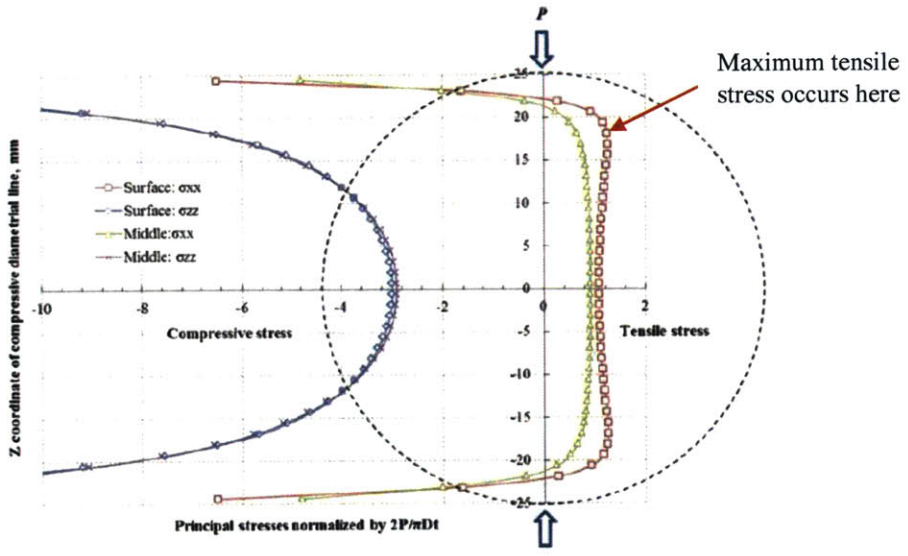

Figure 2.24 Numerical simulation results for the principal stresses distribution along the compressive diametrical line. The red line represents the horizontal tensile stress. From the figure, the maximum stress occurs away from the specimen center.

Wang et al. only conducted numerical analysis and analytical derivations (see Section 2.2.2.2), for 2α value smaller than 30°. Later, Keles and Tutluoglu (2011) expanded the numerical analysis to 2α value larger than 30° by using the 'ABAQUS' software. Approximate formula for T_0 were determined by curve fitting.

Keles and Tutluoglu (2011) also stated that in their numerical analysis $\sigma_1 + 3\sigma_3 > 0$ was always valid so therefore, Equation 2.24 is valid based on the Hoek-Brown criterion (1980). Keles and Tutluoglu (2011) determined formulae for σ_1 and σ_3 to calculate T_0. In their numerical analysis, the 2α angle value was varied between 15° and 60° while applied loading P, specimen diameter D, specimen thickness t were kept as constant. For each 2α value, Keles and Tutluoglu (2011) determined σ_1 and σ_3 at the center. Next they determined the dimensionless principal stresses at the center $\overline{\sigma_1}$ and $\overline{\sigma_3}$ as:

$$\overline{\sigma_1} = \frac{\sigma_1}{2P/\pi Dt}$$

and

$$\overline{\sigma_3} = \frac{\sigma_3}{2P/\pi Dt}$$

For each 2α, $\overline{\sigma_1}$ and $\overline{\sigma_3}$ were obtained and seven 2α values were tried in total. Then, $\overline{\sigma_1}$ versus 2α and $\overline{\sigma_3}$ versus 2α were plotted. By curve fitting, the relationship between $\overline{\sigma_1}$ and 2α, and the relationship between $\overline{\sigma_3}$ and 2α, were obtained. They are expressed as:

$$\overline{\sigma_1} = \frac{\sigma_1}{2P/\pi Dt} = 1.08\cos\alpha + 1.92 \tag{2.46}$$

and

$$\overline{\sigma_3} = \frac{\sigma_3}{2P/\pi Dt} = -0.94\cos\alpha - 0.04 \tag{2.47}$$

Substituting Equation 2.46 and 2.47 into Equation 2.24 gives

$$\overline{T_0} = \frac{T_0}{2P/\pi Dt} = 0.83\cos\alpha + 0.15 \tag{2.48}$$

and Equation 2.48 can be used to determine the tensile strength. The method proposed by Keles and Tutluoglu (2011) makes it very convenient to calculate the tensile strength when 2α value is larger than 30°. Nonetheless, both Wang's method and Keles' method should be used with caution. Both methods assumed that the flattened specimen is subjected to a uniformly distributed loading (uniform stress over the flattened surface). In the experiments of this research project, however, the loading may not be a uniformly distributed loading (it will be discussed in Chapter 4) so therefore, additional numerical analysis is required to determine tensile stress accurately.

2.2.3.3 Fracture toughness

Wang and Xing (1999) stated that the fracture toughness could be determined by the flattened Brazilian tests. Their numerical work will be introduced first, followed by the comments on their method.

Wang and Xing (1999) proposed the equation below to calculate the fracture toughness:

$$K_{IC} = \frac{P}{\sqrt{R}t}\emptyset(\alpha, \frac{a}{R}) \tag{2.49}$$

where K_{IC} is the fracture toughness, P is the applied loading, R is the specimen radius, t is the speicmen thickness and ϕ is a constant depends on the 2α value and a/R ratio (a is the half length of crack).

Wang and Xing (1999) then studied how ϕ changes with the a/R ratio using the boundary element method. In their numerical analysis, they rearranged Equation 2.49 to determine ϕ:

$$\emptyset = \frac{K_{IC}\sqrt{R}t}{P} \tag{2.50}$$

K_{IC}, t, α and R were kept constant in the numerical analysis while for each calculation, the crack half length a was varied. As a result, P varied correspondingly, and ϕ was determined based on Equation 2.50. ϕ versus a/R was then plotted in Figure 2.25 below. They stated that based on Figure 2.25, when a was increasing from zero, ϕ increased to a maximum value first and then decreased. In addition, they stated that ϕ_{max} is only dependent on 2α, and it can be determined numerically

before the test. They have done all this for two values of 2α: when 2α was 20°, ϕ_{max} = 0.78 and a/R = 0.8; when 2α was 30°, ϕ_{max} = 0.58 and a/R = 0.73.

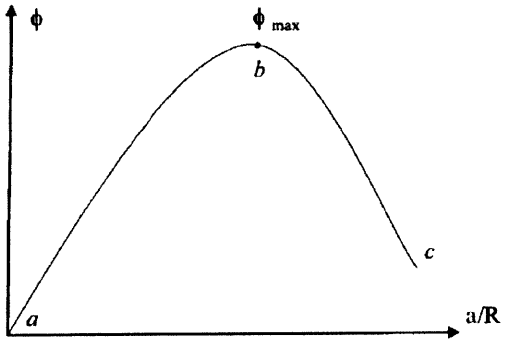

Figure 2.25 ϕ value changing with half crack length a (Wang and Xing, 1999)

Figure 2.12 (the load displacement curve) shows that in flattened Brazilian tests, the loading increases to a local maximum value at tensile crack initiation. The loading drops as crack propagates and the loading drops to a local minimum value when the cracking stops. Then, the loading increases again. Based on Figure 2.12 and Figure 2.25, Wang and Xing (1999) formulated a *hypothesis* which relates the change of ϕ to the change of load. They stated that the fracture toughness K_{IC} is a material property so during one test, the right side of Equation 2.49 should be constant. In addition, during one test, the specimen radius R and the specimen thickness t do not change; only the loading P and ϕ change. Thus, to keep $\frac{P}{\sqrt{Rt}}\emptyset$ (the right side of Equation 2.49) a constant, a decrease in P must lead to an increase in ϕ; and vice versa (Wang and Xing, 1999). In Figure 2.12, the loading starts to decrease at point a and increases again at point b (loading at point b is the minimum loading after the crack initiation). Therefore, ϕ should start to increase at point a, reach maximum value (ϕ_{max}) at point b, and then decrease (Wang and Xing, 1999).

Wang and Xing (1999) stated that based on their numerical analysis (Figure 2.25), ϕ_{max} is only dependent on 2α and ϕ_{max} corresponds to point b. Therefore, the fracture toughness can be determined based on 2α and the loading at point b:

$$K_{IC} = \frac{P_B}{\sqrt{Rt}}\emptyset_{max}(\alpha) \tag{2.51}$$

They also stated that only ϕ_{max} is independent of a (the half length of the crack). If loadings at other points are used, ϕ becomes dependent on the crack length so the crack length needs to be measured.

As a result, the testing becomes more complicated and time-consuming. Therefore, they suggested that the loading at point b should be used.

Later, Wang et al. (2004) used the finite element method to calculate ϕ (they only showed the results without providing other details). When 2α was 20°, $\phi_{max} = 0.7997$ and a/R = 0.81; when 2α was 30°, $\phi_{max} = 0.5895$ and a/R = 0.73 (see Figure 2.26) (Wang et al., 2004). They stated that the results for the finite element method (Wang and Xing, 1999) and the boundary element method (Wang et al., 2004) were very similar.

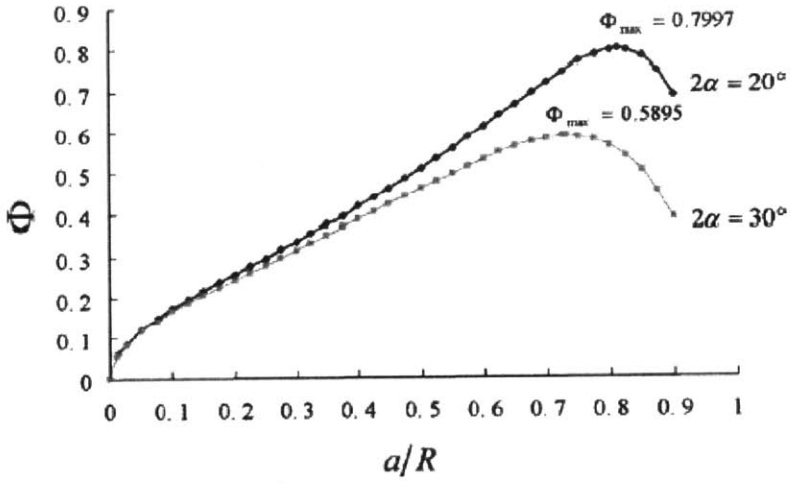

Figure 2.26 ϕ changing with a/R (Wang et al., 2004)

Wang's method (2004) is not convincing. The loading at point b (see Figure 2.12) can be used *only if* the crack starts to propagate very close to point b. However, this has not been proven by any experiments. In addition, the ϕ versus a/R curve (see Figure 2.25) has not been verified by any tests. In other words, the trend that ϕ increases first, reaches maximum at point b, and then decreases has not been verified by experiments. In Figure 2.25 (or Figure 2.26), at point a (a=0, where the crack initiates), $\phi = 0$. Based on Equation 2.49, the fracture toughness at crack initiation becomes zero, which is not realistic. Therefore, the initial part of the ϕ versus a/R curve (the segment close to point a) is wrong.

2.2.4 Comparison of conventional Brazilian test with uniaxial tension test and three-point bending test

2.2.4.1 Uniaxial tension test

The uniaxial tension tests directly measure the tensile strength of a rock specimen. As illustrated in Figure 2.27 and Figure 2.28, tensile stress is applied by a universal testing machine with cylindrical metal caps cemented to the specimen ends.

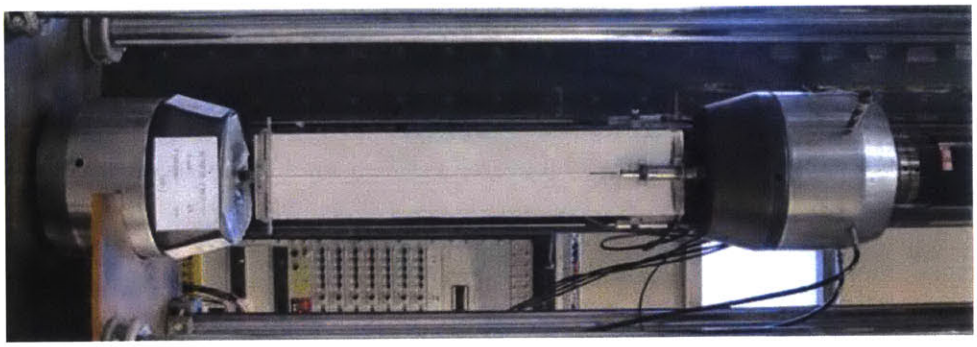

Figure 2.27 Uniaxial tension test (Deluce, 2011)

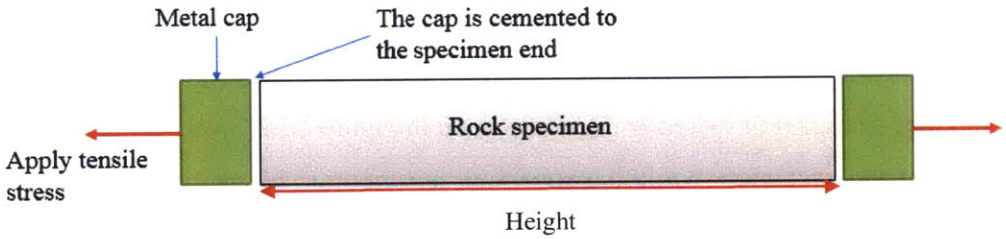

Figure 2.28 Illustration of uniaxial tension test

ISRM (1978) suggests that the specimen should be a right-angled cylinder, with a height to diameter ratio between 2.5:1 and 3.0:1. The diameter should be no less than 54mm (ISRM, 1978). In addition, to reduce the eccentricity, the ends should be smooth and 'shall not depart from perpendicularity to the axis of the specimen by more than 0.001 radians (about 3.5min) or 0.05 in 50mm' (ISRM, 1978). ISRM (1978) also recommended that the loading rate should be between 0.5MPa/s and 1.0 MPa/s.

The direct tensile strength is expressed as:

$$\sigma_t = \frac{P}{A} \tag{2.52}$$

where P is the maximum loading applied to the specimen (loading at failure) and A is the specimen original cross-section area.

Uniaxial tension tests often predict lower tensile strength compared to conventional Brazilian tests or flattened Brazilian tests (Wright, 1955). The discrepancy can be explained by the "weakest link" theory, which states that under uniformly distributed tensile stress, the specimen fails at the weakest flaw (Epstein, 1948). In uniaxial tension tests, the stress distribution within the specimen is uniform so the specimen fails at the weakest flaw. However, in conventional Brazilian tests or flattened Brazilian tests, the tensile stress distribution is non-uniform (Wong and Li, 2013), which indicates that the weakest flaw may not be under the maximum tensile stress. As a result, the specimen may not fail at the weakest flaw if the weakest flaw is not near to the locations where the tensile stress reaches a maximum. Therefore, the measured tensile strength in conventional Brazilian tests or flattened Brazilian tests is often higher than the measured tensile strength in uniaxial tension tests.

2.2.4.2 Three-point bending test

The three-point bending test is used to determine the bending elastic modulus and bending tensile strength (flexural strength) of materials. As illustrated in Figure 2.29, a vertical loading is applied on the middle of the specimen, while the specimen is supported by two rollers at the specimen ends (see Figure 2.29). Maximum compressive stress occurs at point A and maximum tensile stress occurs at point B.

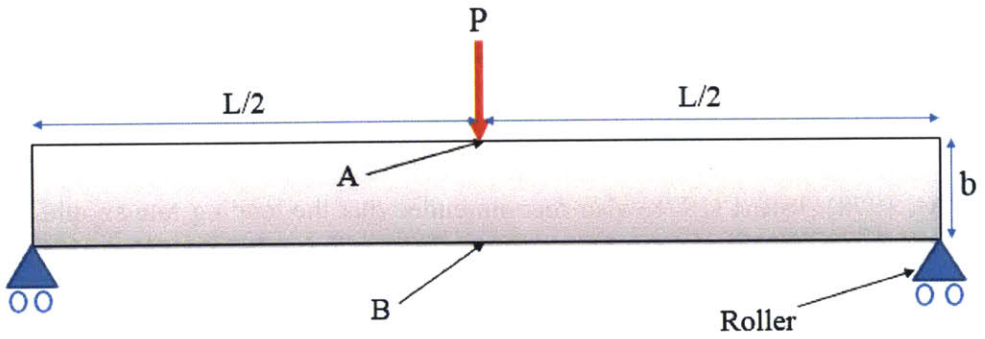

Figure 2.29 Illustration of three-point bending test

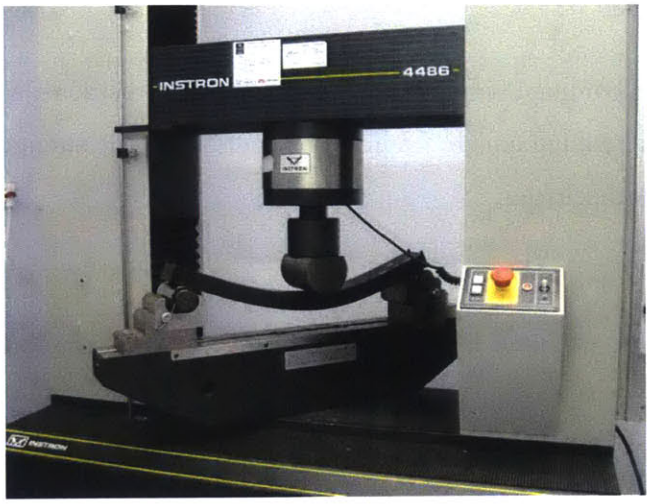

Figure 2.30 Three-point bending test (Wikipedia, 2014)

ASTM D790-10 (2002) recommends that the specimen should have a rectangular shape and the *strain* rate should be 0.01mm/mm/min. ASTM (2002) expresses the specimen bending tensile strength as:

$$\sigma_f = \frac{3PL}{2bd^2} \tag{2.44}$$

where P is the loading at failure, L is the support span, b is the specimen width (see the right side of Figure 2.29) and d is the specimen depth (d is perpendicular to the paper so it is not in Figure 2.29).

The bending tensile strength obtained in the three-point bending test is often higher than the tensile strength obtained in the uniaxial tension test (Whitney and Knight, 1980; Leguillon et al., 2015). The discrepancy can again be explained by the "weakest link" theory, which states that under uniformly distributed tensile stress, the specimen fails at the weakest flaw (Epstein, 1948). In uniaxial tension tests, the stress distribution within the specimen is uniform so the specimen fails at the weakest flaw. However, in the three-point bending tests, the maximum tensile stress occurs at point B (see Figure 2.29), and the tensile stress decreases from point B to the rollers (see Figure 2.29) (Whitney and Knight, 1980; Leguillon et al., 2015). As a result, the specimen will not fail at the weakest flaw if the weakest flaw is not near to point B (Whitney and Knight, 1980; Leguillon et al., 2015). Therefore, the measured tensile strength in the three-point bending test is often higher

than the measured tensile strength in the uniaxial tension test (Whitney and Knight, 1980; Leguillon et al., 2015).

Although some articles compare bending tensile strength to direct tensile strength, it appears that the difference between bending tensile strength and indirect tensile strength (the strength obtained by Brazilian test) is not discussed.

2.2.5 Comments on conventional Brazilian test and flattened Brazilian test

2.2.5.1 Comments on conventional Brazilian tests

The conventional Brazilian tests are much easier to perform compared with other tests, such as the uniaxial tension tests and the three-point bending tests. However, conventional Brazilian tests also have some disadvantages. First, the applied loading may not be a line load. During the experiment, the specimen may deform and the contact surface between the specimen disk and the jaw may be enlarged so therefore, the loading is no longer a line load (see Figure 2.31, the upper loading is not a line load) (Yang, 2012; Guan, 2013). When the loading is not a line load, shear or crushing failure near the loading line can occur, which is not desirable (Yang, 2012; Guan, 2013).

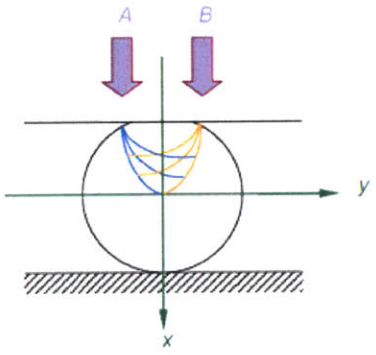

Figure 2.31 Non-point load due to enlarged contact area (Guan, 2011)

In addition, in Equation 2.22, it is assumed that the tensile stress in the x-direction (σ_x, see Figure 2.16) is uniformly distributed (Wong, 2013). However, this assumption may be invalid because σ_x distribution may be non-uniform (Wong, 2013). Also, the specimen may be heterogeneous, which

will cause the non-uniform distribution of σ_x (Wong, 2013). As a result, Equation 2.22 may be inaccurate (Wong, 2013).

2.2.5.2 Comments on flattened Brazilian tests

The flattened Brazilian tests provide a convenient way in determining the fracture toughness for rock specimen. In flattened Brazilian tests, it is relatively easy to prepare the flattened circular discs and run the tests. In addition, on a single specimen, tensile strength, fracture toughness and elastic modulus can be determined. Thus, flattened Brazilian tests can help to save time and effort in rock laboratory testing.

Also, Wang et al. (2004) pointed out that flattened Brazilian tests can help to avoid local failure near the loading line. In conventional Brazilian tests, the contact area between the specimen and the loading jaw is small so therefore, when loading is applied, the local stress concentration can be very large. On the contrary, in flattened Brazilian tests, the contact area between the flattened surfaces and the loading plate is relatively large (the contact area is the whole flattened surface). Thus, when the surface is flat, the local stress near the flattened surfaces in flattened Brazilian tests can be much lower than the local stress near the loading line in conventional Brazilian tests, if the applied loadings are similar. Therefore, flattened Brazilian tests reduce local failure near the loading point by reducing the stress concentration.

In flattened Brazilian tests, it is of vital importance that the flattened surfaces are really flat and parallel to each other. If the flattened surfaces are bumpy, the contact area between the loading plate and the flattened surfaces will be reduced and as a result, calculation errors will be generated (All previous numerical analyses assumed that the flattened surfaces are ideally flat). In addition, Wang and Wu (2004) stated that if the surfaces are not flat enough, after crack initiation, there might be a total failure of the specimen (see Figure 2.32).

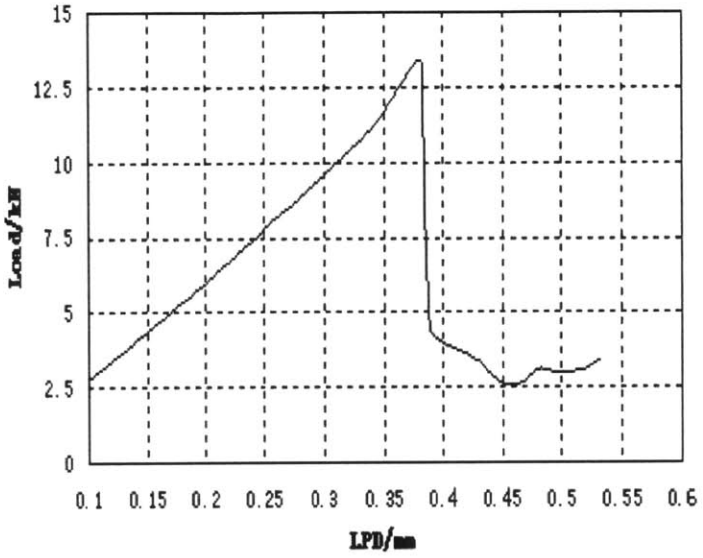

Figure 2.32 An invalid test result (Wang and Wu, 2004). The loading dropped drastically and did not increase again, indicating that the test was unstable and total failure occurred after crack initiation.

Wang and Wu (2004) also stated that if the flattened surfaces are not parallel to each other (see Figure 2.33), the maximum horizontal tensile stress may not occur along the vertical center line of the specimen. Therefore, the primary crack may not initiate at the specimen center and for this case, the specimen should be rejected.

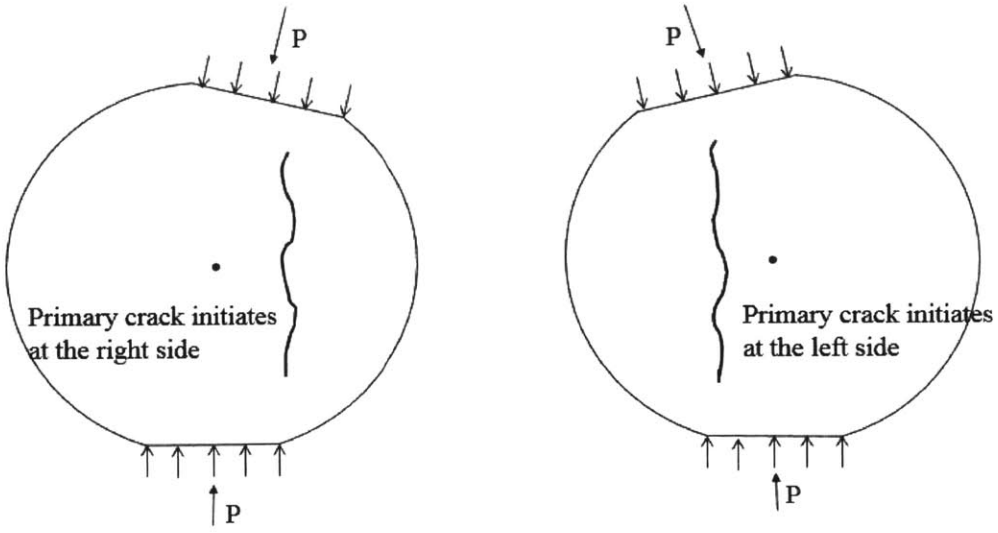

Figure 2.33 Illustration of non-parallel flattened surfaces. As a result, maximum tensile stress may not occur along the vertical center line so the primary crack may not initiate at the specimen center.

Chapter 3 Experimental Setup

3.1 Introduction

To verify whether Mode I fracture toughness of rock varies with specimen size, flattened Brazilian tests were performed on mortar specimens. These mortar specimens vary in size and flatness angle. In total, 126 tests were performed, and for two tests among them, a high speed camera and a high resolution camera were used to observe the crack propagation. This chapter describes the material properties, sample preparation, and apparatus.

3.2 Material properties

Type III Portland Cement (C25), fine-grained silt, and water were used to cast mortar specimens. This type of cement was used to reduce the time for specimen preparation. Concrete made of Type III Portland Cement gains 90% of its ultimate strength after seven days, while concrete made of Type I Portland Cement (the most commonly used cement in construction) gains only 70% of its ultimate strength, even after 28 days (Fowler, 1985; Kwan, 2012). Thus, mortar cutting and testing can be carried out only one week after mortar specimens are cast. As a result, the time between specimen casting and specimen testing will not affect the fracture toughness, so the specimen testing schedule becomes more flexible. However, it is worth noting that not all the cement was in fine powder form. Before the mortar was cast, the cement had already absorbed some water vapor (the cement was not perfectly sealed), so some cement powder had clumped together. As a result, some clumps were formed beforehand and could be felt by the fingers.

The inclusion effect can play an important role in concrete fracture toughness (Irwin, 1960; Fowler, 1985; Anderson, 2005). In this research project, fine-grained silt (see Figure 3.1) was used instead of aggregates to reduce the inclusion effect. The fine-grained silt was mainly industrial quartz, and the particle size distribution is illustrated in Figure 3.2.

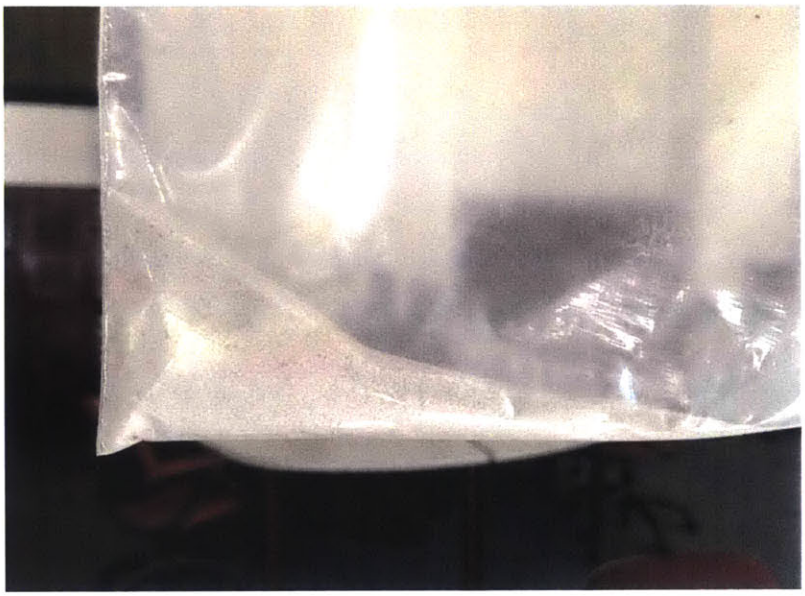

Figure 3.1 Fine-grained Silt

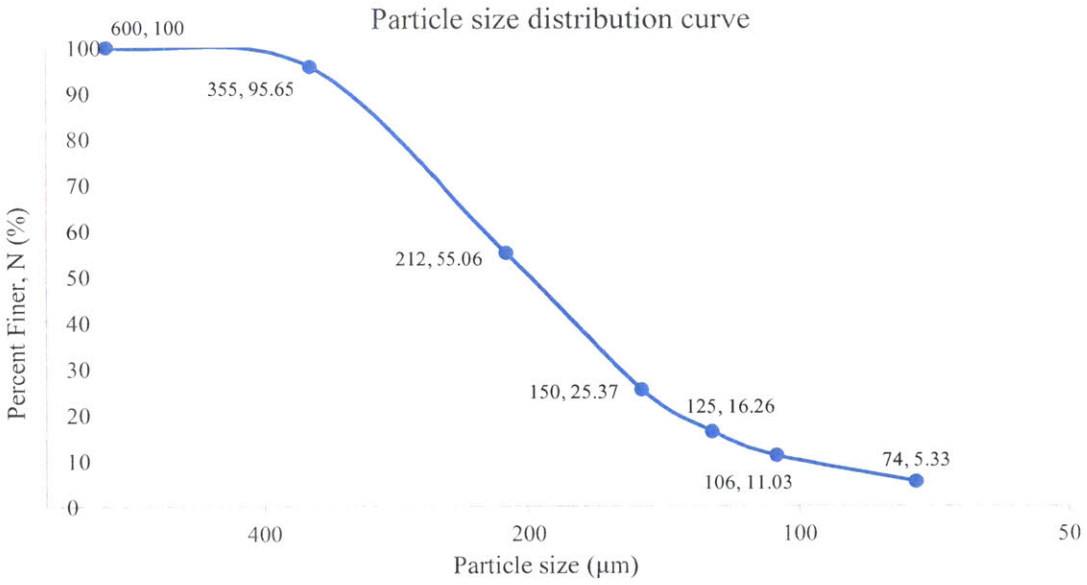

Figure 3.2 Particle size distribution curve for fine-grained silt

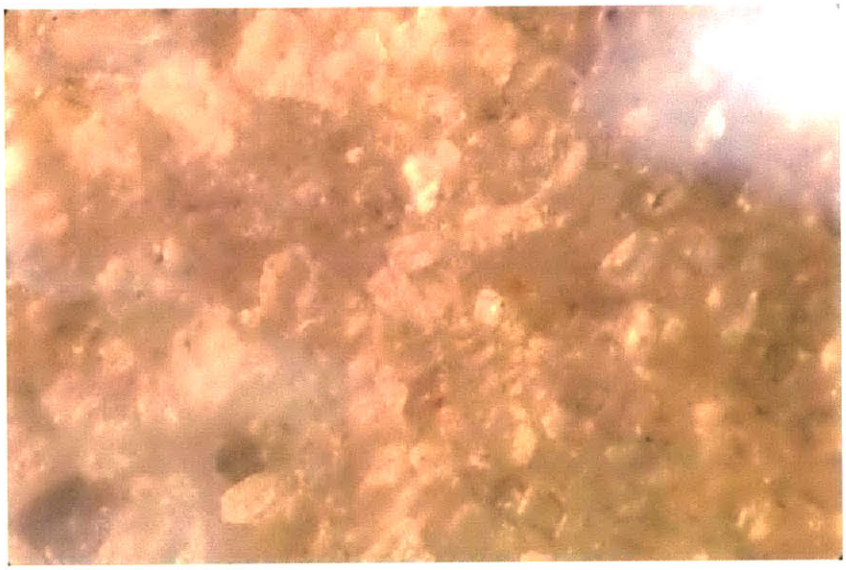

Figure 3.3 Microscopic view of the silt

3.3 Specimen preparation

Cement, silt, and water were mixed at a weight ratio of cement: silt: water = 2:2:1, which is commonly adopted in the construction industry (Kwan, 2006; Kwan, 2012). Cement, silt, and water were mixed manually for 20 minutes before the mixture was vibrated. 20-minute mixing was relatively long, to guarantee that they were mixed evenly. Each time, 8kg cement, 8kg silt, and 4kg water were used.

After 20-minute mixing, mortar was poured into cylindrical molds (see Figure 3.4) and was vibrated on a vibration table (see Figure 3.5). The mortar was vibrated to get rid of the air bubbles; the vibration process is illustrated in Figure 3.6. Cylindrical molds had three different sizes: two-inch, three-inch, and four-inch diameter. First, approximately one-third of the cylindrical mold volume was filled with mortar and the mortar was vibrated for 8 minutes. Then, some additional mortar was poured into the cylindrical mold until two-thirds of the cylindrical mold volume was filled up and the mortar was again vibrated for 8 minutes. Finally, the last one-third of the cylindrical mold volume was filled with mortar and the mortar was vibrated for a final 8 minutes.

Figure 3.4 Two-inch, three-inch and four-inch cylindrical molds

Figure 3.5 Vibration table

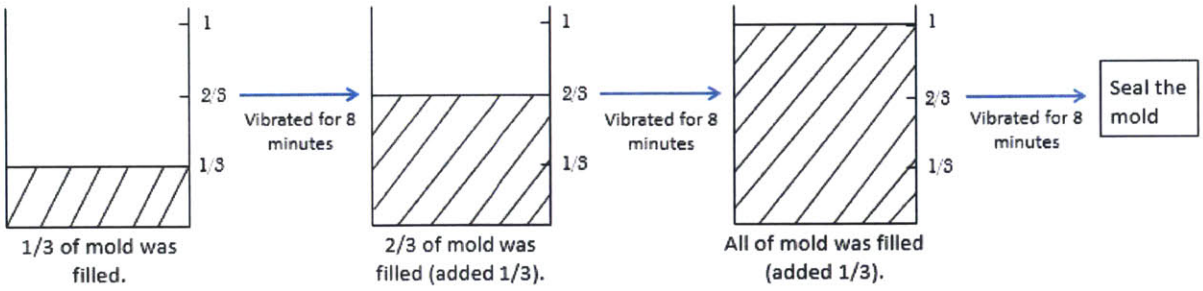

Figure 3.6 The vibration process in mortar casting

After vibrating, the cylindrical molds (filled with mortar) were covered by lid (to reduce evaporation) and left in the concrete room. After six or seven days, hydrated mortar specimens were extruded from the cylindrical molds and the mortar specimens were stored in water. At this time, the mortar specimens had a long cylindrical shape.

Then, the mortar specimens were cut by the wetsaw (see Figure 3.7). First, the long cylindrical mortar specimens were cut into right-angled circular cylinders with the following characteristics:

- The length of the specimen, t, was approximately equal to the radius (D:t = 2:1; see Figure 3.8). This ratio is suggested by ISRM (1978).
- The specimen sides were smooth, straight, and perpendicular to the specimen ends (see Figure 3.8).
- The Specimen ends were flat and circular.

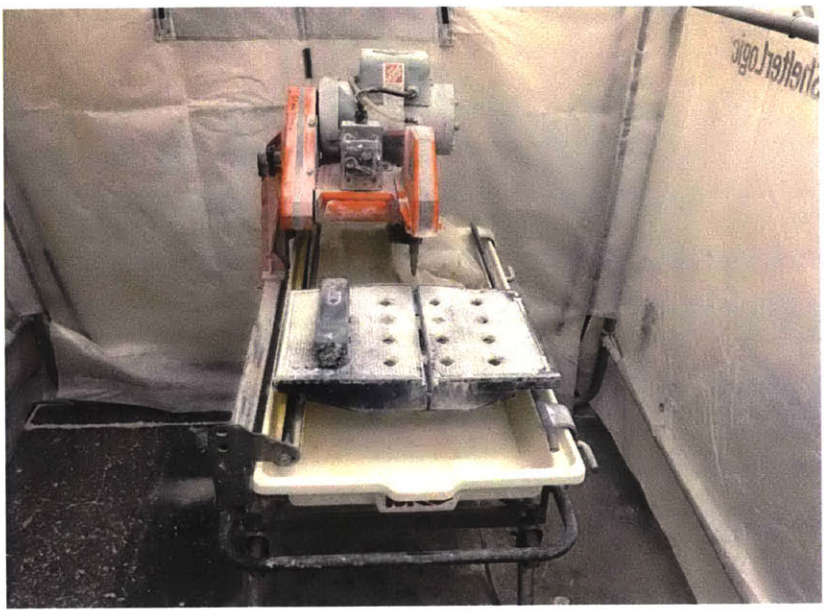

Figure 3.7 Wetsaw

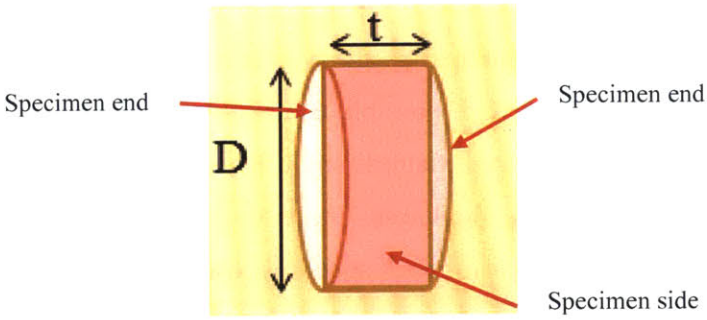

Figure 3.8 Geometry of circular cylinders of mortar

For each batch of mortar, six cylinders were obtained with two-inch, three-inch, and four-inch diameters, respectively (six cylinders for each size). It is worth noting that, after cutting, we can see black dots at the specimen ends (see Figure 3.9). The black dots are the clumps (cement powder that absorbed water vapor and then hydrated prior to mixing) mentioned in 3.2. The clump size is not very large (the maximum diameter is around four millimeters), so the clumps did not lead to serious inclusion effects during testing.

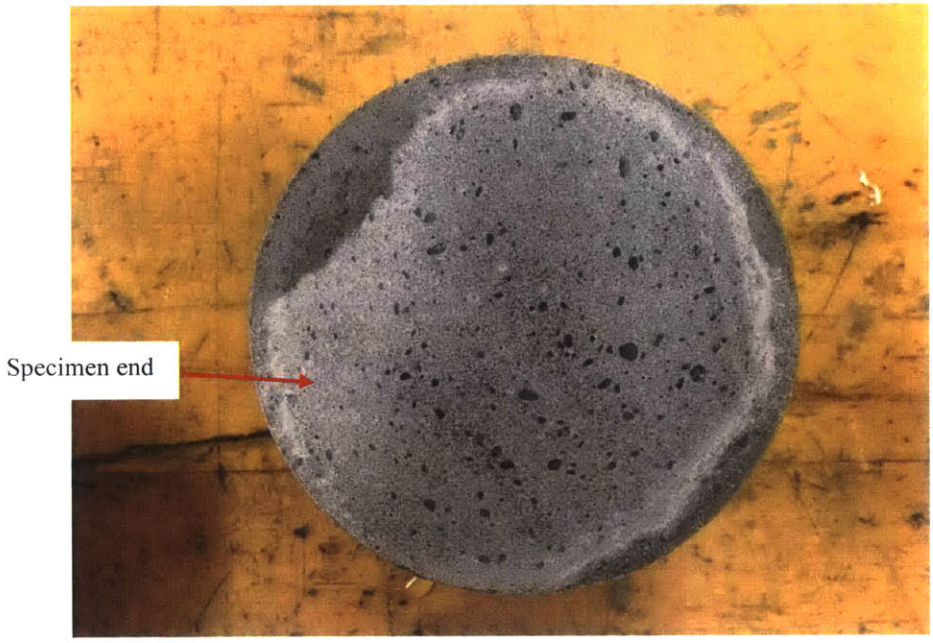

Figure 3.9 Clumps within mortar specimen (the black dots on the surface)

Next, the circular cylinders were flattened by the wetsaw, and the flattened sample geometry is illustrated in Figure 3.10. There are two possible factors that might affect the measured fracture toughness: specimen size (diameter) and flatness angle 2α; however, this study is mainly aimed to investigate the size effect on fracture toughness. Therefore, to control the variables, for each batch of mortar, the flatness angle value 2α for each specimen was controlled not to deviate too much. For the first three batches of mortar, the 2α angle was around 28°; for the fourth and the fifth batches, the 2α angle was around 40°; for the sixth and the seventh batches, the 2α angle was around 23°. The 2α angle for each batch of mortar is shown in Table 3.1 below. The flatness angle 2α for different batches was varied to verify whether the flatness angle would affect the fracture toughness. The experimental results will be discussed in Chapter 5 (Experimental Results and Discussion). After flattening, the mortar specimens were stored again in water.

Table 3.1 Planned flatness angles for each batch of mortar

Batch number	Angle 2α (°)		
	2-inch	3-inch	4-inch
1	28	28	28
2	28	28	28
3	28	28	28
4	39	39	39
5	39	39	39
6	23	23	23
7	23	23	23

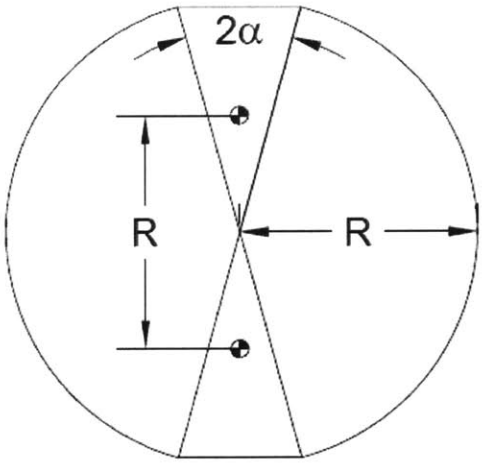

Figure 3.10 Sample geometry after flattening

3.4 Testing Apparatus

The testing apparatus includes: a loading frame (Instron, MODEL 1331), two extensometers (Extensometer 9212 and Extensometer 10520), a data acquisition system, a high speed camera, and a high resolution camera. The schematic and the photo of the setup are shown in Figure 3.11 and Figure 3.12 below.

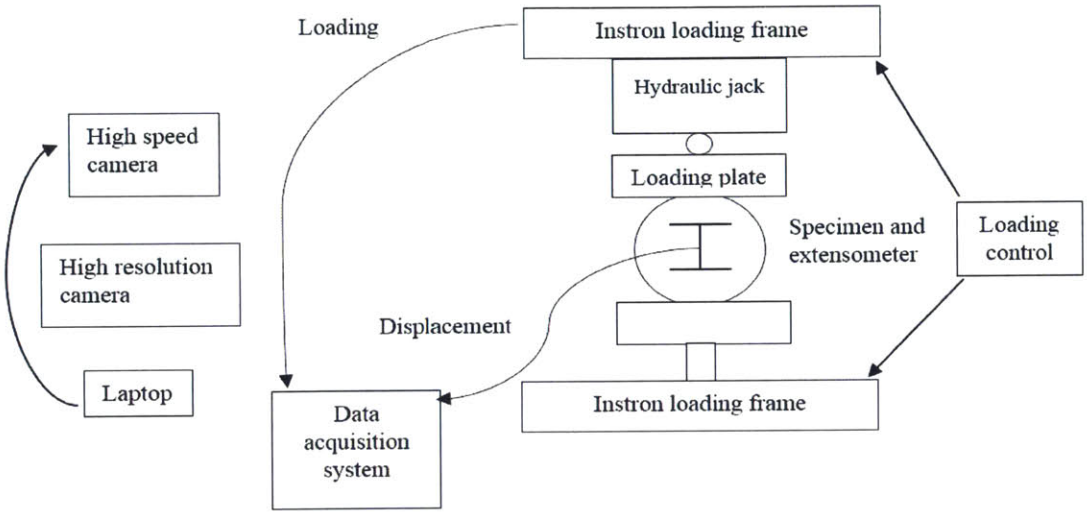

Figure 3.11 Schematic illustration of the experimental setup

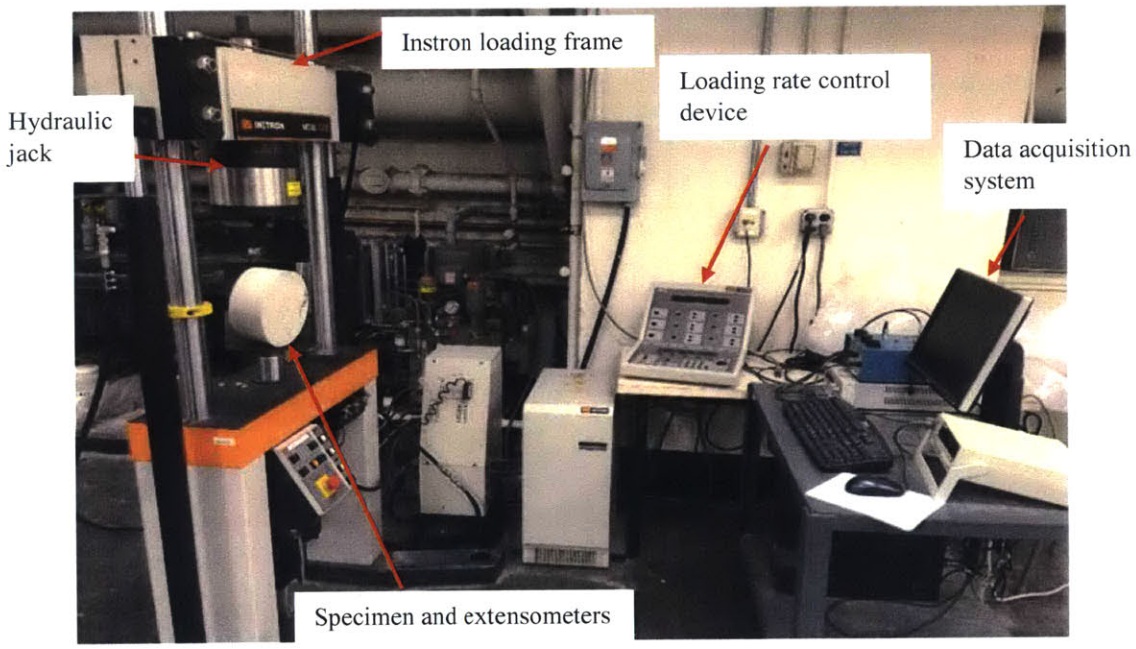

Figure 3.12 Photograph of the experimental setup

3.4.1 Loading frame (Instron)

The Instron (MODEL 1331), with a capacity of 100kN, was used as the loading frame for flattened Brazilian tests (see Figure 3.13).

Figure 3.13 Loading frame (Instron)

The loading rate can have either constant displacement increase or constant loading increase. According to Rudolph and Germaine (2015), the specimen will be more stable if the loading rate has a constant displacement increase. Therefore, the initial loading rate was chosen to be 0.2mm/min (the possible loading rate of the Instron is between 0.1mm/min to 1mm/min). After testing five batches of mortar, the loading rate was decreased to 0.1mm/min. The loading rate was reduced so the loading right after the crack initiation (which was used to determine the fracture toughness) could be measured more accurately. The load drop for the sixth and seventh batches of mortar is larger than the load drop for the first five batches of mortar, which means that the loading right after the crack propagation may be more accurately captured (this will be explained in detail in Section 5.9). However, as a result, tests became much more time-consuming.

During the test, the Instron measured the load and the machine displacement in the form of voltage. The voltage change was recorded by the data acquisition system and was converted into kN and mm. The conversion factors are 10kN/1V and 5mm/1V. The sampling frequency of the data acquisition system can be chosen between 1Hz and 10 Hz. For the testing of the first five batches

of mortar, the sampling frequency was 2Hz, and for the last two batches, the sampling frequency was increased to 10Hz to improve the measurement accuracy.

The only disadvantage of the Instron is that it cannot measure the end-to-end displacement of the mortar sample. The displacement measured by the Instron includes the displacement of the hydraulic jack. In addition, seating errors may occur. Thus, extensometers are needed to determine the sample displacement.

3.4.2 Extensometers

Two extensometers (Extensometer 9212 and Extensometer 10520) were used to measure the specimen displacement. The gauge length of both extensometers can be adjusted to 1 inch, 1.5 inch, or 2 inch. Each extensometer was installed in the center line of the specimen and its gauge length was set to the specimen radius, R (see Figure 3.10 and Figure 3.14. In Figure 3.9, the two small circles represent the top and the bottom of the extensometer, and in Figure 3.14, two arrows point to the top and the bottom of the extensometer).

Extensometers measured the displacement in the form of voltage. The voltage was recorded by the data acquisition system and was converted to mm. For Extensometer 9212, the conversion factor is 216.35mm/V and for Extensometer 10520, the conversion factor is 201.325mm/V. The sampling frequency can be chosen as either 1Hz or 2Hz, and 2Hz was selected to improve the measurement accuracy.

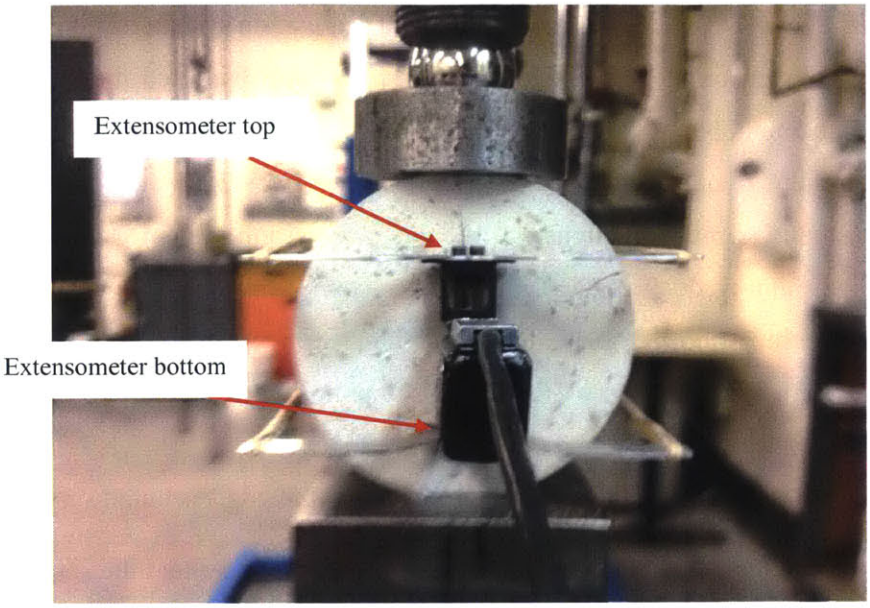

Figure 3.14 Extensometers

3.4.3 Data acquisition system

The data acquisition system recorded the voltage change from the Instron and two extensometers. The sampling frequency of the Instron and two extensometers was controlled by the data acquisition system. For the testing of the first five batches of mortar, only one data acquisition system was used, but for the testing of the last two batches, two data acquisition systems were used (see Figure 3.15).

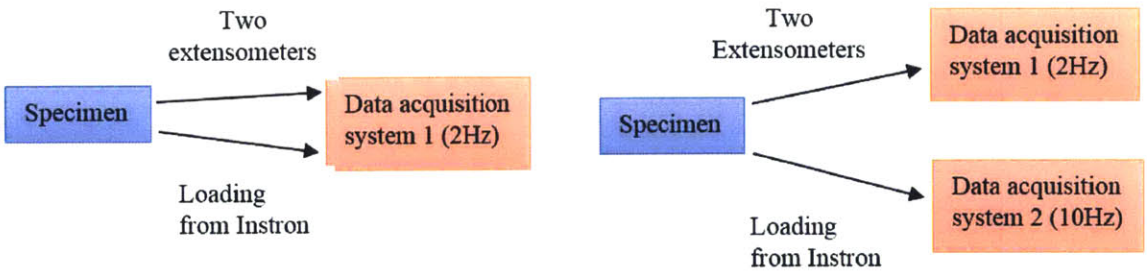

Figure 3.15 The left half represents the data acquisition system for the first five batches of mortar and the right half represents the data acquisition system for the last two batches

In the testing of the first five batches of mortar, the data acquisition system received voltage change from both the two extensometers and the Instron. The Instron exported the voltage change for loading and displacement, but only the voltage change for loading was used. As mentioned above, the possible maximum frequency of the two extensometers was 2Hz and for the Instron it was 10Hz. However, the maximum frequency of the data acquisition system was determined by the least possible maximum frequency of all the devices connecting to it. For instance, if one data acquisition system controls both extensometers and the Instron, the maximum sampling frequency the acquisition system can set is only 2Hz. If the sampling frequency is 5Hz (between 2Hz and 10Hz), it works well for the Instron but it does not work for extensometers. Therefore, in the testing of the first five batches of mortar, the sampling frequency of the data acquisition system was 2Hz.

After the testing of the first five batches of mortar, it became evident that the sampling frequency of the Instron needed to be raised to measure the applied loading more accurately. Therefore, in the testing of the last two batches of mortar, two data acquisition systems were adopted. One data acquisition system monitored two extensometers, and the sampling frequency was 2Hz. The other data acquisition system monitored the Instron, and the sampling frequency was 10Hz (see Table 3.2). For the last two batches of mortar, the load displacement curve is plotted based on the data from data acquisition system 1. Then, the peak loading and the loading right after the crack propagation is replaced by the peak loading and the loading right after the crack propagation obtained by data acquisition system 2.

Table 3.2 Sampling frequency for different batches of mortar specimens

Batch number	Data acquisition system 1		Data acquisition system 2	
	Sampling frequency (Hz)		Sampling frequency (Hz)	
	Extensometer (Displacement)	Instron (Loading)	Instron (Displacement)	Instron (Loading)
1	2	2	-	-
2	2	2	-	-
3	2	2	-	-
4	2	2	-	-
5	2	2	-	-
6	2	2	10	10
7	2	2	10	10

Figure 3.16 Data acquisition system

3.4.4 Camera

In two flattened Brazilian tests, both the high speed camera and the high resolution camera were used to detect the primary crack initiation and propagation. A Photron™ SA-5 high speed camera with a Tamron™ 90mm lens was used to capture high speed video (see Figure 3.17). The camera captured 5,000 frames per second and the number of the frame can be adjusted by the laptop controlling the camera. The camera was continuously recording and once it was triggered, the last 1.25 seconds of high speed frames were stored. The pixel resolution was 512 × 512. In addition, a Nikon™ D90 high resolution camera with a 105mm lens was also used to get high resolution images (See Figure 3.18), and the shooting frequency is 2Hz.

Figure 3.17 Photron™ SA-5 high speed camera (Morgan, 2015)

Figure 3.18 Nikon™ D90 high resolution camera (Morgan, 2015)

Chapter 4 Numerical Analysis

4.1 Introduction

As stated in Chapter 2, Wang and Xing (2004) used the 'ANSYS' software to determine the elastic modulus of a flattened Brazilian specimen. Several numerical analyses with different specimen sizes and different specimen geometries were conducted and the *empirical* equation was obtained by curve fitting:

$$E = \frac{2P}{\pi \Delta w t}\left[(1-\mu) - ln\left(1 + \frac{4}{(\sin\alpha)^2}\right)\right]\frac{\alpha}{\sin\alpha} \tag{5.1}$$

where E is the elastic modulus, P is the peak loading (the loading when crack initiates), Δw is the end-to-end displacement of the sample, t is the specimen thickness, μ is the Poisson's ratio, α is the flatness angle.

However, it is very difficult to measure the end-to-end displacement of the specimen, and it is much easier to measure the displacement between the points on the center line of the specimen (See Figure 4.1. Two small circles represent the above mentioned points, which are also the top and the bottom of the extensometers). During the experiments the extensometer displacement was measured instead of the specimen end-to-end displacement. Thus, a finite element analysis was carried out to determine the elastic modulus of the specimen from the peak loading and the extensometer displacement.

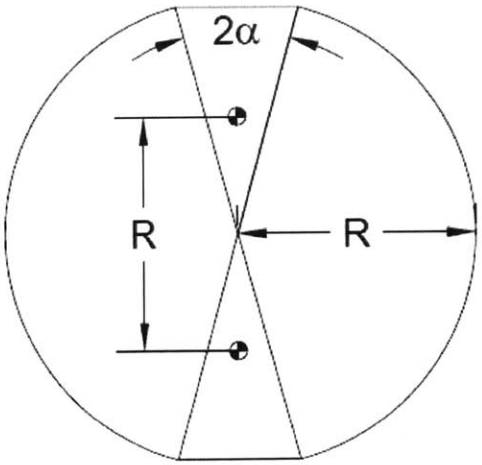

Figure 4.1. The position of the extensometer (Represented by two small circles)

Wang and Xing (1999) also proposed an equation for calculating the tensile strength from the peak loading:

$$\sigma_t = \sigma_G = \frac{2P}{\pi Dt}\left[\frac{(2cos^3\alpha + \cos\alpha + \sin\alpha/\alpha)^2}{8(\cos\alpha + \sin\alpha/\alpha)}\frac{\alpha}{\sin\alpha}\right] \quad (5.2)$$

Where P is the peak loading, D is the specimen diameter, t is the thickness and α is the flatness angle. The complete derivation process is shown in Section 2.2.2.2. However, Equation 5.2 is only applicable when 2α value is between 20° and 30° (Wang and Xing, 1999). Keles and Tutluoglu (2011) proposed an *empirical* equation:

$$\sigma_t = \frac{2P}{\pi Dt}(0.83\cos\alpha + 0.15) \quad (5.3)$$

where P is the peak loading, D is the specimen diameter, t is the thickness and α is the flattnes angle. Keles and Tutluoglu (2011) stated that Equation 5.3 is applicable when 2α is between 15° and 60°. Equation 5.3 is discussed in detail in Section 2.2.3.2.

Both methods assumed that the flattened specimen is subjected to a uniformly distributed loading (uniform stress over the flattened surface). In this research project, however, a point load was applied to the loading plate by the hydraulic jack (see Figure 4.2). As a result, the displacement along the flattened surface is uniform but the stress distribution along the flattened surface is non-uniform (see Figure 4.3), and additional numerical analysis is required to determine tensile stress accurately.

In this chapter, I will first describe the basic geometry of the nodes. Then, I will discuss the boundary conditions and the material input. Finally, I will discuss how to determine the elastic modulus and the tensile strength.

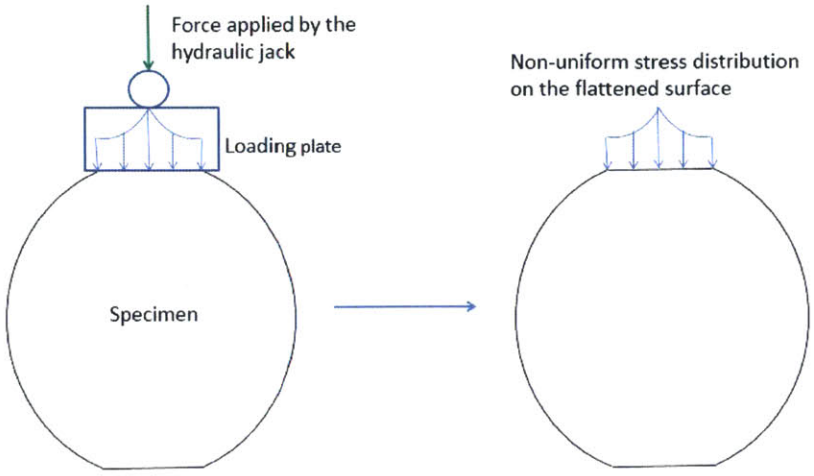

Figure 4.2 Non-uniform stress distribution on the flattened surface

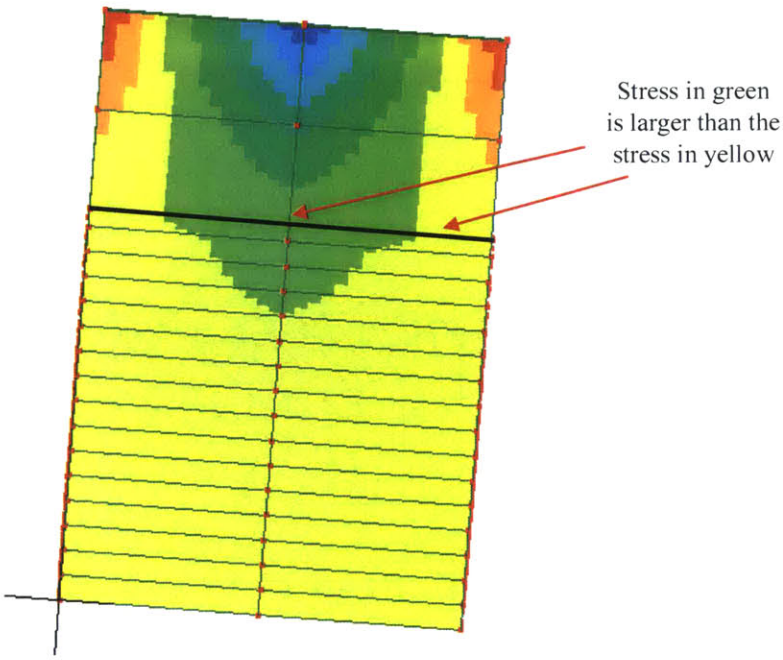

Figure 4.3 Vertical compressive stress distribution in the specimen (side view) obtained by numerical analysis. The black thick line represents the flattened surface and different colors represent different magnitudes of stress. On the flattened surface, the color changes, which illustrates that the stress distribution is non-uniform.

4.2 Basic geometry

The 'Lisa 8.0' software was used in the finite element analysis since it is relatively easy to learn and run. However, the maximum nodes for a model is limited to 1,300, and the software can only perform analysis under linear elastic deformation. Due to symmetry, I generated the mesh only for the first quadrant of the specimen (See Figure 4.4). Figure 4.4 is the undeformed mesh generated for the finite element analysis (z direction is perpendicular to the paper). Red dots represent the nodes and green lines form the mesh. The green arrow represents the loading applied by the hydraulic jack. The upper rectangle represents the loading plate and the lower part (a quadrant of the flattened specimen) represents the mortar specimen. In addition, the red triangles represent the boundary conditions which will be discussed next.

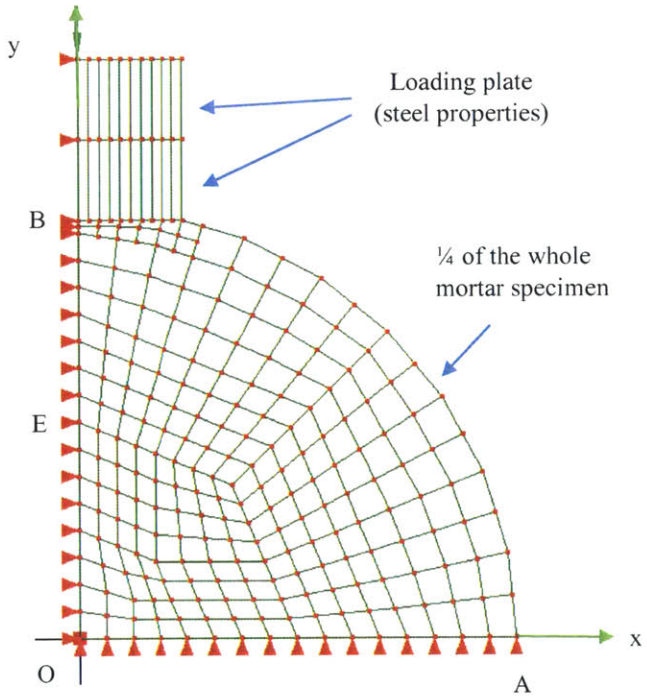

Figure 4.4 Mesh for finite element analysis (A quadrant)

4.3 Boundary conditions

Three boundary conditions are applied in the finite element analysis:

i. Zero vertical displacement in the y = 0 line (x-axis, see Figure 4.4). Due to specimen symmetry, there is no vertical displacement in line AA' (See Figure 4.5), which is the y = 0 line in Figure 4.4.

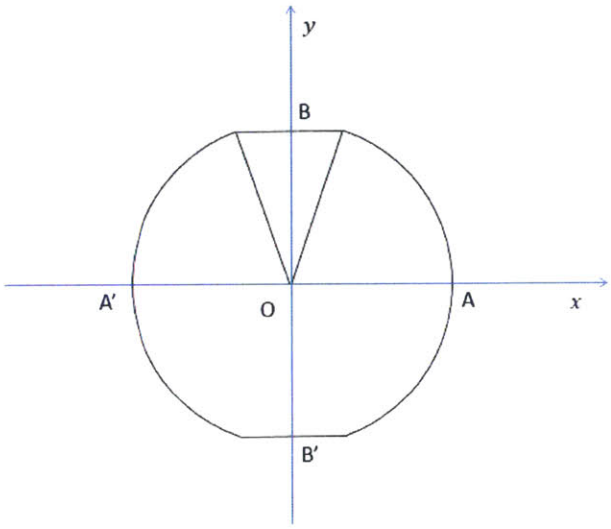

Figure 4.5 Geometry of the flattened sample

ii. Zero x-direction displacement in the x = 0 line (See Figure 4.4). Due to specimen symmetry, there is no x-direction displacement in line BB' (See Figure 4.5), which is the x = 0 line in Figure 4.4. However, in the experiments, if the crack does not initiate at the specimen center, the x-direction displacement in the x = 0 line will not be zero.

iii. There was no z-direction movement in point D (See Figure 4.6, the middle of OC line). Theoretically, point D is the geometrical center of the flattened specimen so point D should not have any displacements in the x, y, and z directions.

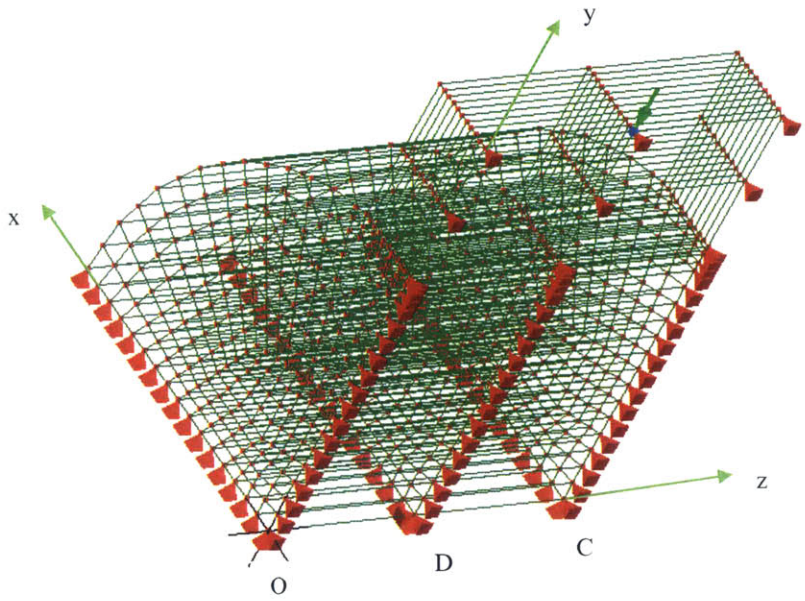

Figure 4.6 Side view of the sample (point D is in the middle of OC line and it is the specimen geometrical center)

4.4 Material input

In the finite element analysis, the inputs are the elastic modulus of the steel loading plate, the Poisson's ratio of both the loading plate and the mortar specimen. The elastic modulus of steel is suggested to be taken as 200GPa (Connor, 2012; Young, 2014; Au, 2012), and the Poisson's ratio of concrete and mortar is suggested to be taken as 0.2 (Swamy, 1971; Ulm, 2003; Kwan, 2004; Hong Kong Buildings Department, 2013).

The Poisson's ratio of steel usually varies between 0.27 and 0.32 (Young, 2014; Anand, 2014). In the numerical analysis, a brief investigation of the effect of the loading plate's Poisson's ratio was conducted (the Poisson's ratio varied from 0.25 to 0.35). It showed that the Poisson's ratio of the loading plate has little influence on the simulation results (elastic modulus and tensile strength of the mortar). For example, for one specimen, when the Poisson's ratio is 0.25, the elastic modulus is 17.50 GPa and the tensile strength is 4.18MPa; when the Poisson's ratio is 0.35, the elastic modulus is 17.30GPa and the tensile strength is 4.17MPa. Hence, the Poisson's ratio for steel was chosen as 0.3 for convenience.

4.5 Methods to determine the elastic modulus

The elastic modulus is determined first. The steps are listed below:

- In FE (Finite Element) software, set the applied loading (green arrow in Figure 4.4) equal to **half** of the crack initiation loading (loading at point A, see Figure 4.7). Due to symmetry, the loading in the FE specimen should be half of the applied loading in the experiments.
- Randomly choose an elastic modulus value of the mortar and input that value.
- Run the program and get the displacement between O and E (E is the mid-point of line OB; see Figure 4.4). Denote the displacement as δ_1.
- Adjust the elastic modulus value of the mortar and run the program **until δ_1 is equal to half of the averaged extensometer displacement at point A (see Figure 4.7).** Due to symmetry, the displacement between OE should be half of the displacement between two circles in Figure 4.1, which is the averaged extensometer displacement.
- The elastic modulus of mortar (E_{mortar}) is equal to the average slope of line OA (See Figure 4.7).

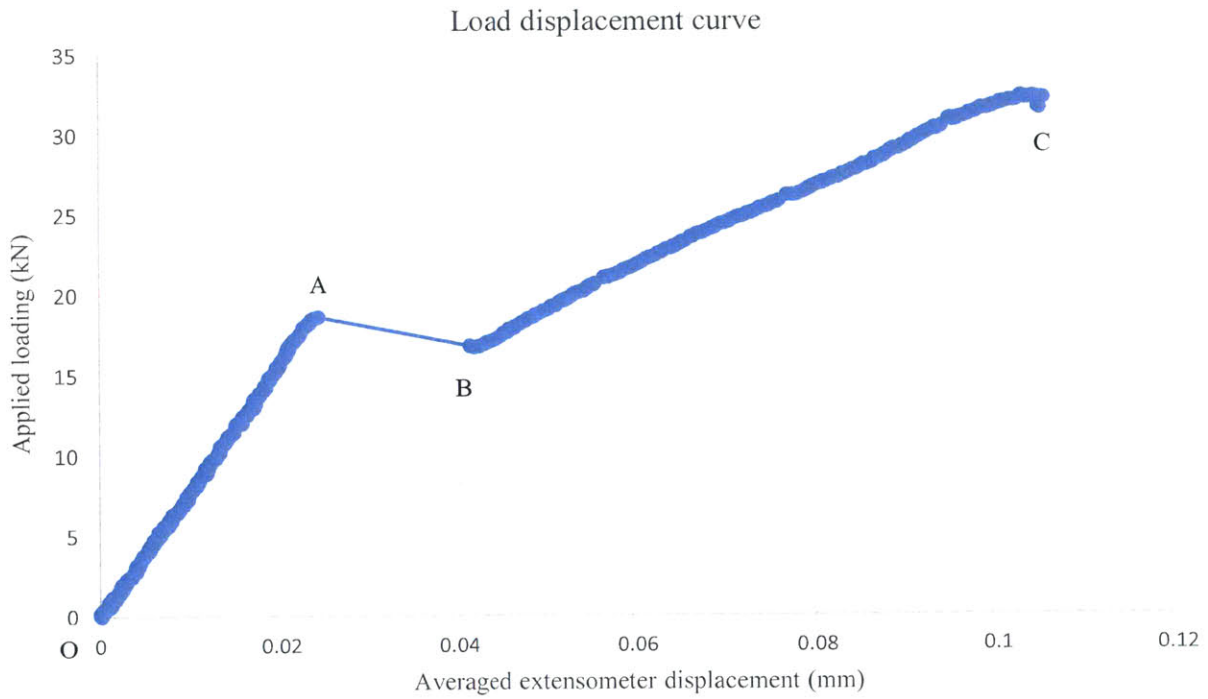

Figure 4.7 A typical load displacement curve

4.6 Methods to determine the tensile strength

The loading at point A (see Figure 4.7) is the loading required to generate tensile failure (initiate the tensile crack) so the tensile strength calculation should be based on the loading at point A. The tensile strength is obtained based on the E_{mortar} determined in Section 4.5:

- Set the applied loading (green arrow in Figure 4.4) equal to **half** of the crack initiation loading (loading at point A, see Figure 4.7). Based on the E_{mortar} determined in Section 4.5, calculate the stress distribution within the specimen.
- Take σ_{xx} at the specimen center (point O in Figure 4.4. σ_{xx} is the horizontal tensile stress in the x direction) as the tensile strength. As discussed in Chapter 2, when the 2α value is larger than 19.5°, the maximum tensile stress always occurs at the specimen center (Wang and Xing, 1999; Keles and Tutlougu, 2011).

It is worth noting that for all specimens, the simulation results satisfied $\sigma_{xx} \gg \sigma_{zz}$ (i.e. For one specimen, when σ_{xx} was 5.2MPa, σ_{zz} was only 0.36MPa). Thus, the principal stress in the z-direction can be neglected ($\sigma_{zz} \approx 0$). Mathematically, the plane stress condition is defined where one of the principal stresses is zero so therefore, the specimens can be assumed to be under plane stress conditions.

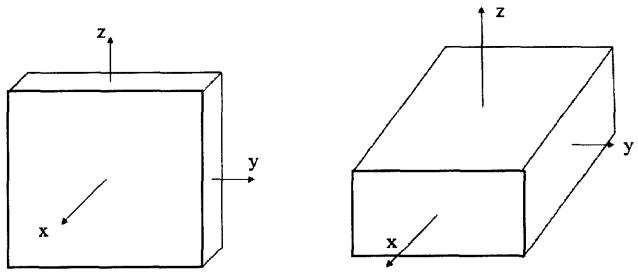

Figure 4.8 Plane stress condition and plane strain condition

This chapter only discusses the simulation approaches. The simulation results will be discussed, together with the experimental data, in Chapter 5.

Chapter 5 Experimental Results and Discussion

5.1 Introduction

This chapter presents and discusses the experimental results. In total, 126 flattened Brazilian tests (including two tests using the high speed camera and the high resolution camera) were carried out on mortar specimens with different sizes and different 2α angles. First, the result acceptance criteria and data interpretation methods will be introduced. Next, the experimental results will be presented. It will be discussed how the elastic modulus, tensile strength, fracture toughness, averaged applied compressive stress at crack initiation (the local maximum loading), and the averaged applied compressive stress when cracking stops (the local minimum loading) change with size. Finally, analyses of the high speed video and high resolution images will be given.

5.2 Result acceptance criteria

To get reliable experimental results, the following acceptance criteria were used:

- Ideally, the flattened surface should be a rectangle. However, during specimen cutting and flattening, for some specimens, the specimen sides were not exactly perpendicular to the specimen ends (See Figure 5.1). As a result, after flattening, the flattened surface was a trapezoid (See Figure 5.1). If the length of AB was less than 90% of the length of CD (AB and CD are the surface widths and AB is shorter than CD), the specimen was rejected.

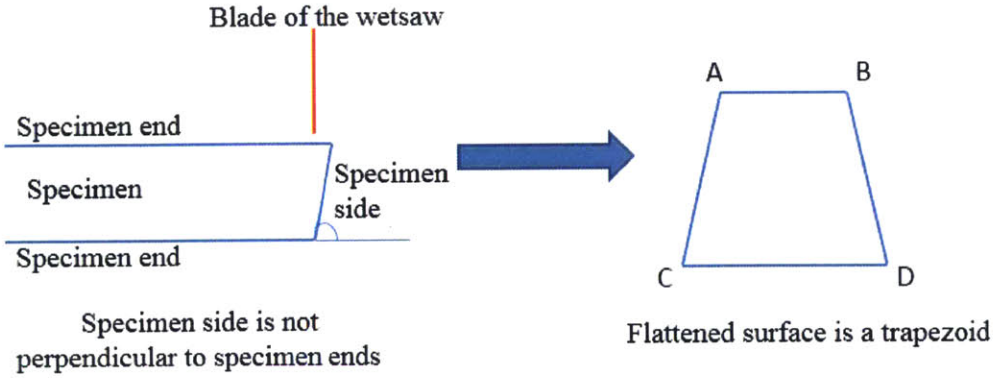

Figure 5.1 One trapezoid flattened surface

- Under ideal conditions, for the same specimen, two flattened surfaces should have the same width. However, for some specimens, after flattening, the widths for two surfaces were not the same. The specimens of which the shorter width was less than 90% of the longer width were discarded. Figure 5.2 illustrates two flattened surfaces having different widths.

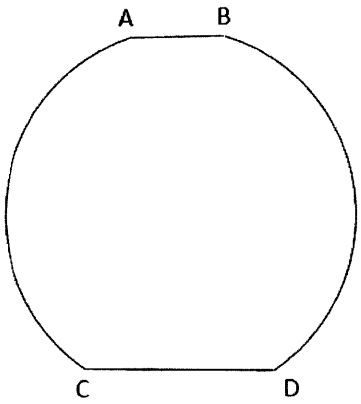

Figure 5.2. Two flattened surfaces having different widths (Exaggerated). AB represents one flattened surface and CD represents another flattened surface. The length of AB is shorter than the length of CD, which indicates that two flattened surfaces have different widths.

- The primary crack should initiate at the specimen center. If the primary crack did not initiate in the specimen central region, or secondary cracks (shear cracks) occurred before the primary crack, the testing results of that specimen were not accepted. Figure 5.3 and Figure 5.4 show a typical central crack.

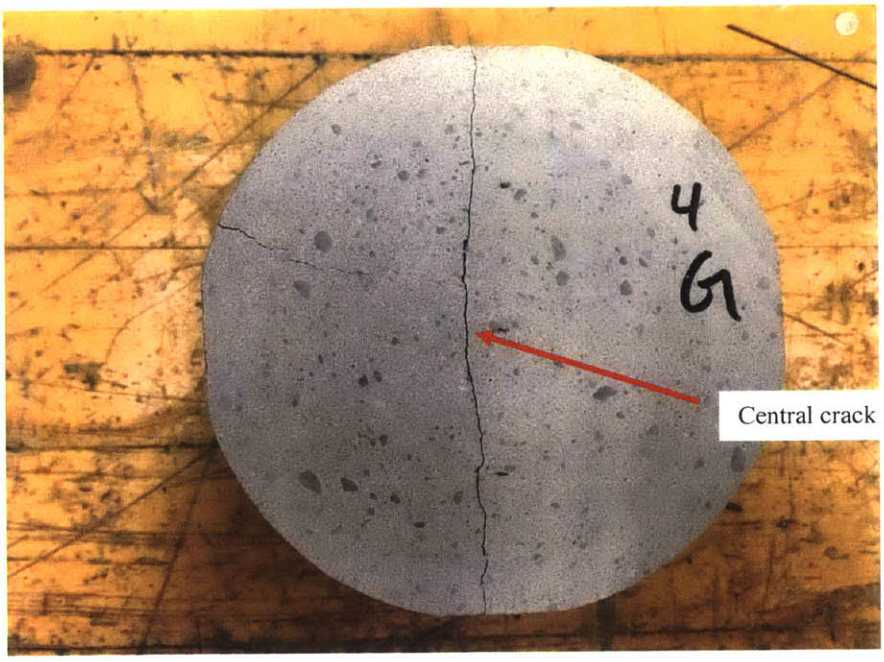

Figure 5.3 A central crack for three-inch specimen

Figure 5.4 The central crack is a typical tensile crack.

Under the above criteria, the testing results of 19 specimens were rejected, so the testing results of 107 specimens were accepted.

5.3 Data interpretation

During the experiments, specimen geometry (2α value, specimen diameter D and specimen thickness t), two extensometer displacements, local peak loading P_A (the loading when crack initiates, see point A in Figure 5.5) and local minimum loading P_B (the loading when tensile crack propagation stops, see point B in Figure 5.5) were measured. The two extensometer displacements were averaged as δ_{avg} ($\delta_{avg} = \frac{\delta_1+\delta_2}{2}$).

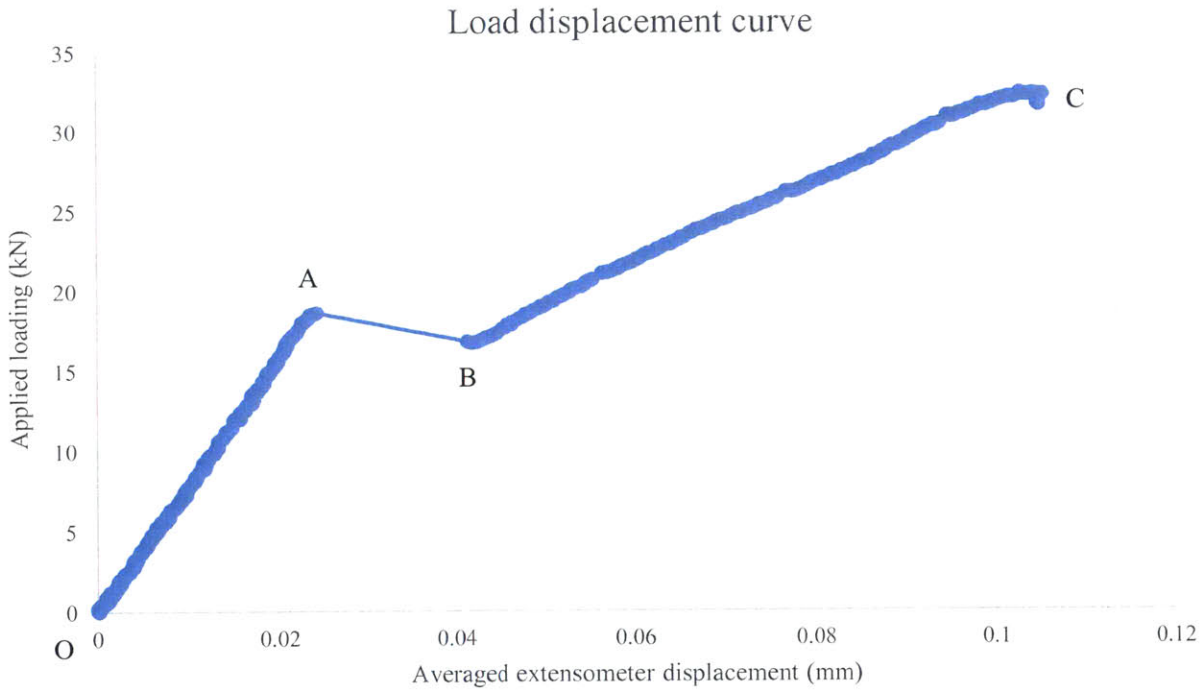

Figure 5.5 A typical load displacement curve of flattened Brazilian tests

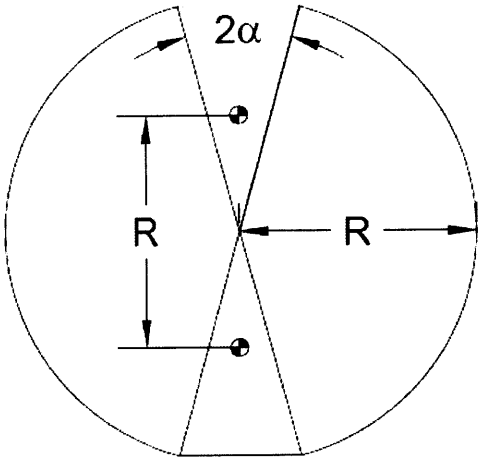

Figure 5.6 The position of the extensometer (Represented by two small circles)

Figure 5.5 shows that the load displacement curve is similar to the load displacement curve proposed by Wang and Xing (1999) (see Figure 5.7, which is also Figure 2.12). During the tests, the loading was displacement controlled, and a constant displacement rate was applied (this is explained in Chapter 3). As stated in Section 2.2.1.2, the testing procedure can be divided into three stages (Wang and Xing, 1999).

Stage 1 corresponds to segment OA in Figure 5.5 (which is also segment oa in Figure 5.7). The applied loading starts from zero to a local peak loading (point A), and when the loading reaches point A, a tensile crack initiates in the specimen central region. In addition, as shown in Figure 5.5, the specimen deforms linearly in stage 1 and the average slope of segment OA is used to calculate the elastic modulus.

Stage 2 corresponds to segment AB in Figure 5.5 (which is also segment ab in Figure 5.7). The displacement rate is kept the same throughout the test and the loading drop is caused by the crack propagation. At this stage, the crack propagates along the center line and the loading reaches the local minimum loading when the crack propagation stops. Stage 1 and stage 2 have been explained in details in Section 2.2.1.2.

Stage 3 corresponds to segment BC in Figure 5.5 (which is also segment bc in Figure 5.7). For stage 3, Figure 5.5 and Figure 5.7 are different. Wang and Wu (2004) stated that the specimen undergoes tensile total failure at point c and the loading at point c should be smaller than the loading at point a. However, this statement is disputable. In the testing, at stage 3 the specimen

central region is no longer under tensile stress because primary tensile cracking has occurred. Numerical analyses (see the methods in Section 4.5 and Section 4.6. The stress distribution within the specimen can be obtained) indicate that the specimen periphery (near the two flattened surfaces) is under a large vertical compressive stress and a relatively small horizontal stress (horizontal stress can be either compressive or tensile). For example, for a two-inch specimen with $2\alpha = 22.5°$, right after the primary crack initiation, the vertical compressive stress at the specimen periphery is 37.1MPa while the horizontal *compressive* stress is 8.2MPa (Compression is taken as positive). When the loading increases, the vertical compressive stress may increase much faster than the horizontal stress. As a result, the compressive strength may be reached before the tensile strength, although the compressive strength of mortar is larger than the tensile strength (Hong Kong Buildings Department, 2013; Au, 2012; Kwan, 2006). Therefore, the specimen may undergo compressive failure. One high speed video showed that the specimen underwent compressive failure. However, only one high speed video is not enough to support the compressive failure statement, and further investigations need to be carried out.

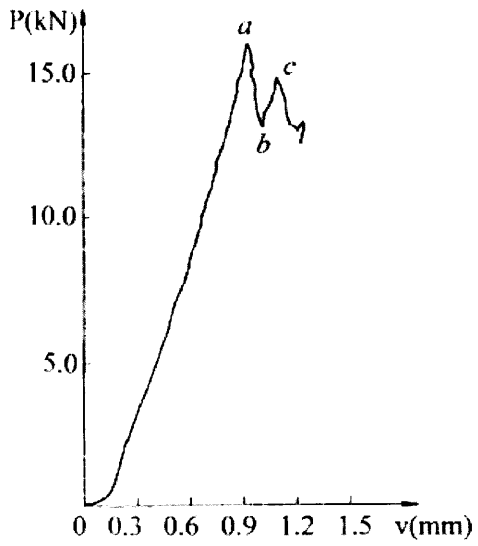

Figure 5.7 Load displacement curve proposed by Wang and Xing (1999)

5.3.1 Elastic modulus calculation

The elastic modulus E is determined as the averaged slope of segment OA (see Figure 5.5), and was discussed in Section 4.5.

5.3.2 Tensile strength calculation

The *magnitude* of tensile strength σ_t is calculated based on the specimen geometry and local peak loading P_A (see point A in Figure 5.5). P_A is used to determine tensile strength because stress at point A is the stress required to initiate the tensile crack. Section 4.6 discusses the σ_t calculation.

It is worth noting that, when the flatness angle 2α is around 39°, some specimens start to deform nonlinearly before tensile crack initiation, as illustrated in Figure 5.9. When the flatness angle 2α is around 39°, the specimen center is under relatively larger vertical compressive stress compared with the specimen center when 2α is 23° or 28°. For example, for three-inch diameter specimens, when 2α is 39°, the vertical compressive stress in the specimen center is around 15.50MPa; when 2α is 23° and 28°, the vertical compressive stresses are 10.45MPa and 12.50MPa, respectively (the vertical compressive stresses for each 2α is determined by averaging the vertical compressive stresses for ten specimens). Therefore, local compression yielding may occur in the specimen center, which means that the specimen already starts to yield before tensile crack initiation. Under this case, the loading at point D P_D (see Figure 5.9) should be used to calculate the tensile strength.

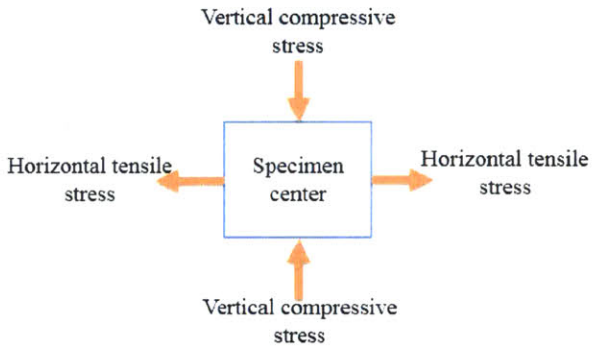

Figure 5.8 Stresses in the specimen center

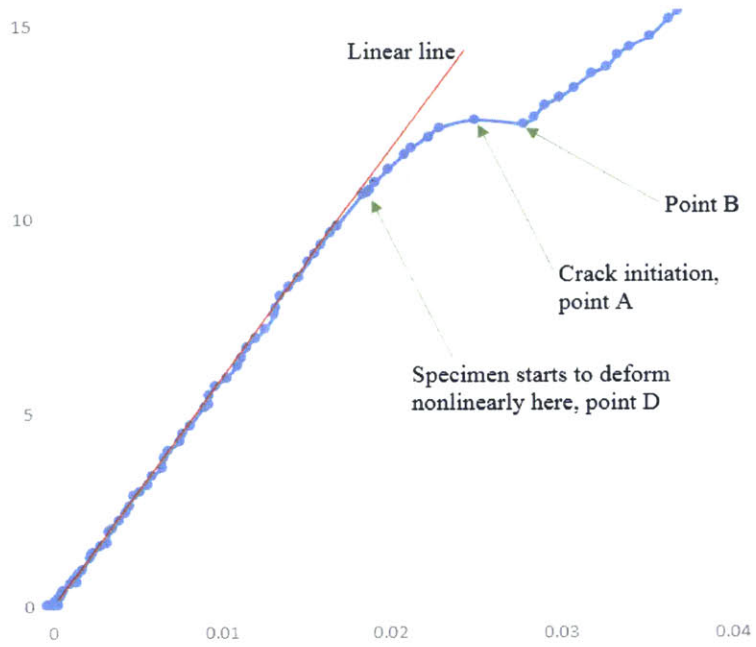

Figure 5.9 Local compression yielding before tensile crack initiation

5.3.3 Fracture toughness calculation

Wang and Xing (1999) proposed an equation for fracture toughness calculation:

$$K_{IC} = \frac{P_B}{\sqrt{R}t} \emptyset_{max} \tag{5.1}$$

where P_B is the loading at point B (see Figure 5.5), R is the specimen radius, t is the specimen thickness, ϕ_{max} is a factor, which is only dependent on 2α. Their analysis has been introduced in Section 2.2.3. As discussed in Section 2.2.3, their method is not convincing. In their analysis, they assumed that the crack starts to propagate when the loading is very near to the loading at point B. However, this is not verified by experiments. In addition, the ϕ_{max} value, which was determined by numerical analysis, has not been proved by tests. Therefore, their method will not be used.

Since ϕ_{max} is unknown, in the fracture toughness calculation ϕ_{max} is assumed to be 1. Therefore, Equation 5.1 becomes:

$$K_{ICA,B} = \frac{P_{A,B}}{\sqrt{R}t} \tag{5.2}$$

where P is the loading at either point A or point B (see Figure 5.5). The crack propagation may start at any point in the segment AB since no experiment has been conducted to explore where the crack starts to propagate. During the experiments, the loadings at A and B are the only two available loadings. Therefore, the loadings at point A and B are used to calculate the fracture toughness.

In flattened Brazilian tests, when the specimen diameter R and specimen thickness t is kept constant, the loading for crack propagation P may be dependent on 2α. Thus, a factor that is dependent on 2α may needs to be included in the fracture toughness calculation. However, ϕ is not included in Equation 5.2 because ϕ could not be determined in the current work. Therefore, the fracture toughness can be compared only if the specimens have the same 2α (so the effect of ϕ on fracture toughness can be eliminated).

5.4 Experimental results for specimens with $2\alpha \approx 28°$ (first three batches of mortar specimens)

5.4.1 Experimental results for the first three batches of mortar specimens

The 2α was approximately 28° for the first three batches of mortar specimens, 23° for the fourth and fifth batches, and 39° for the sixth and seventh batches. The experimental results for the first three batches of mortar are presented in Table A.1 through Table A.15 in Appendix A1. The elastic modulus E, tensile strength σ_t, σ_A (the *averaged compressive stress* acting on the flattened surfaces at point A, see Figure 5.5), σ_B (the *averaged compressive stress* acting on the flattened surfaces at point B, see Figure 5.5), K_{ICA} (fracture toughness based on P_A, see Figure 5.5), and K_{ICB} (fracture toughness based on P_B, see Figure 5.5) changing with size are summarized in Table 5.1 and Table 5.2, and Figure 5.10 through Figure 5.15 below.

Table 5.1 Summary of experimental results for the first three batches of mortar ($2\alpha = 28°$)

Size	Mean of E (GPa)	SD of E (GPa)	Mean of σ_t (MPa)	SD of σ_t (MPa)	Mean of σ_A (MPa)	SD of σ_A (MPa)	Mean of σ_B (MPa)	SD of σ_B (MPa)	No. of specimens
2-inch	18.35	2.42	4.60	0.55	31.89	3.41	27.63	4.16	15
3-inch	16.03	1.42	3,81	0.42	26.90	2.79	24.74	2.81	14
4-inch	18.27	1.87	3.20	0.30	22.99	2.59	20.77	2.41	15

Note: SD means standard deviation.

Table 5.2 Summary of experimental results for the first three batches of mortar ($2\alpha = 28°$)

Size	Mean of K_{ICA} ($MPam^{0.5}$)	SD of K_{ICA} ($MPam^{0.5}$)	Mean of K_{ICB} ($MPam^{0.5}$)	SD of K_{ICB} ($MPam^{0.5}$)	No. of specimens
2-inch	2.47	0.27	2.14	0.33	15
3-inch	2.52	0.24	2.32	0.30	14
4-inch	2.48	0.23	2.23	0.22	15

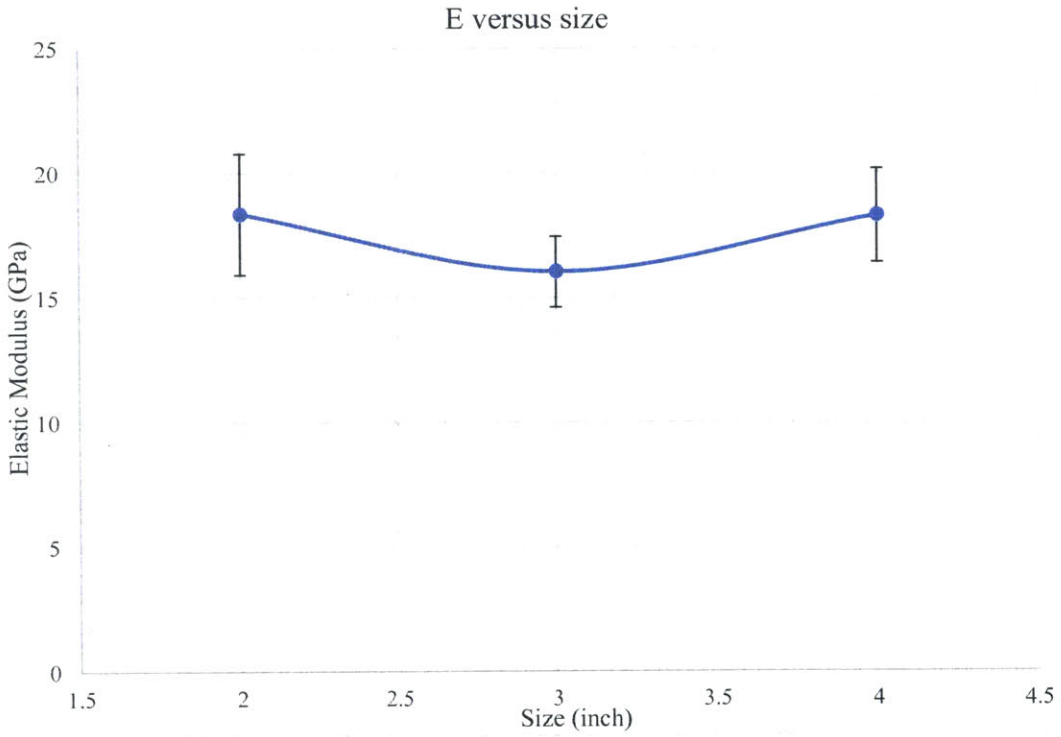

Figure 5.10 Elastic Modulus changing with size (error bars represent standard deviation)

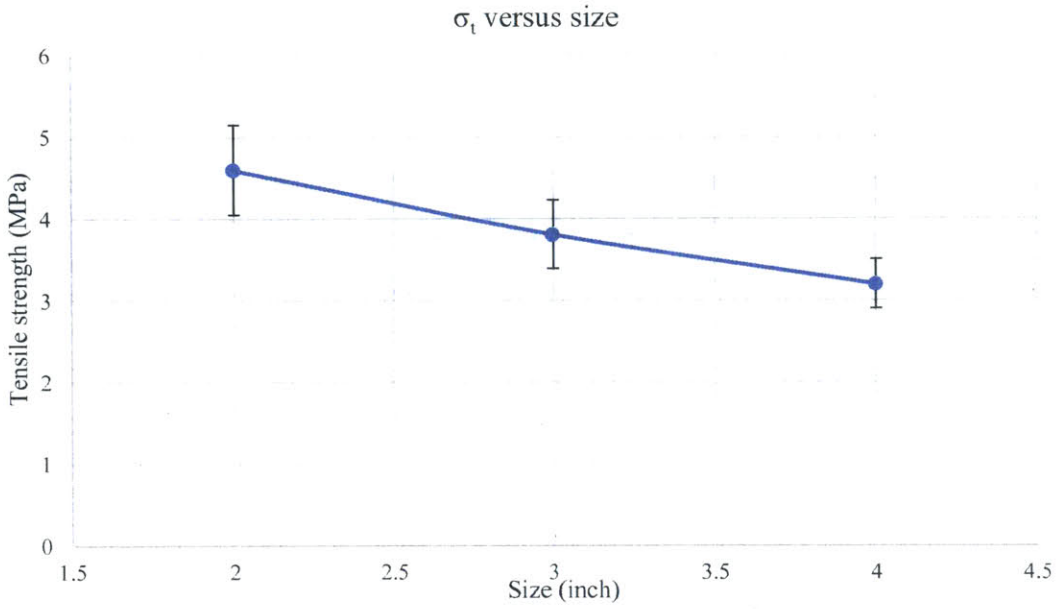

Figure 5.11 Tensile strength changing with size (error bars represent standard deviation)

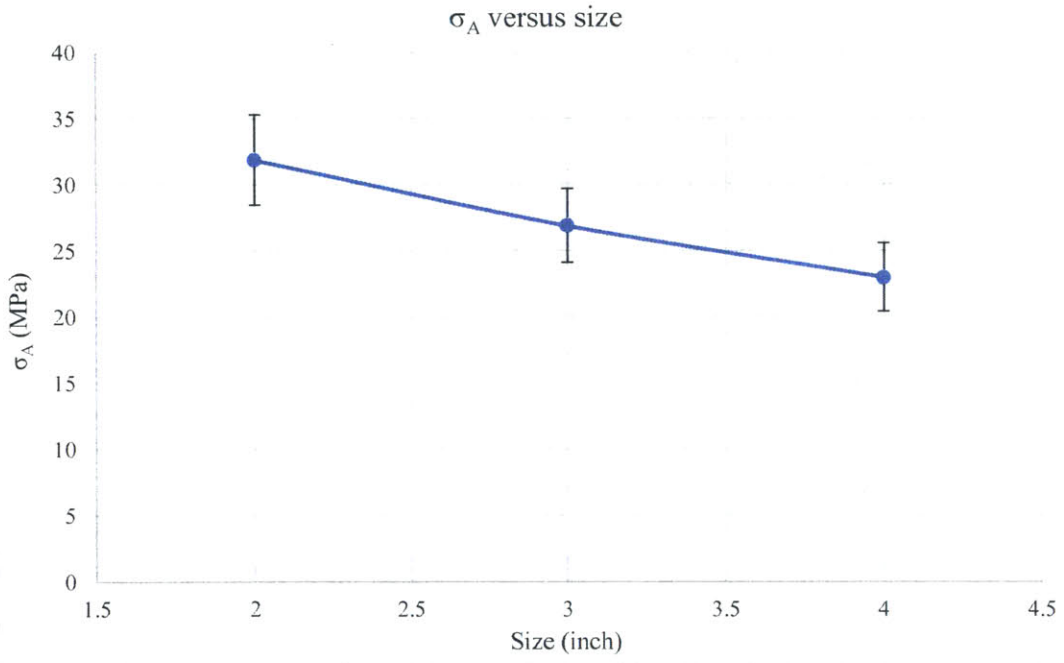

Figure 5.12 σ_A changing with size (error bars represent standard deviation)

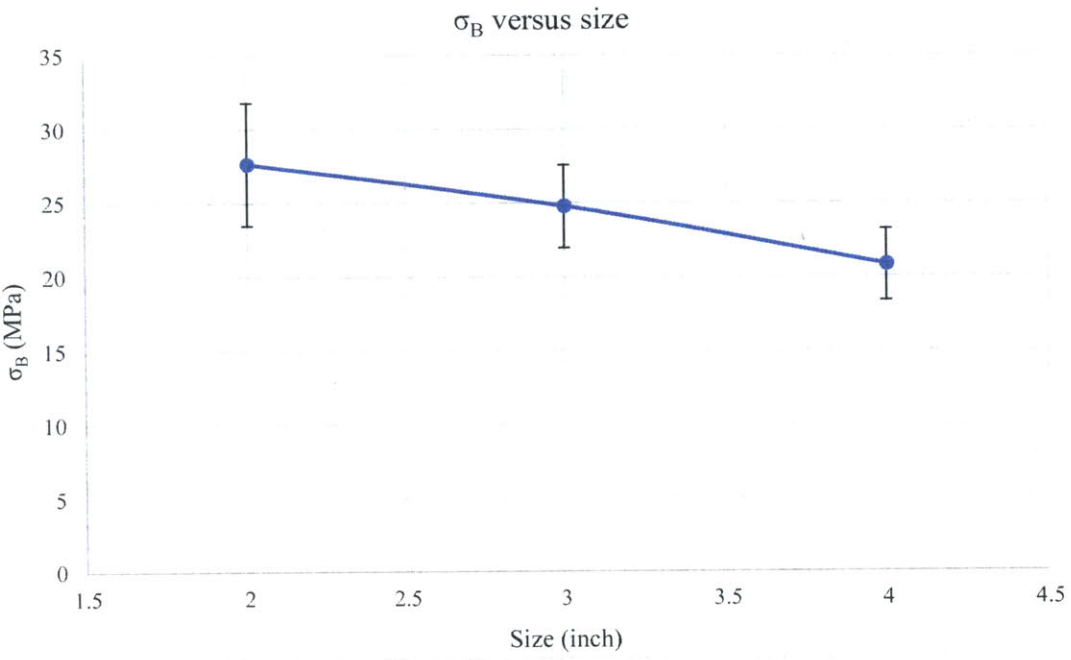

Figure 5.13 σ_B changing with size (error bars represent standard deviation)

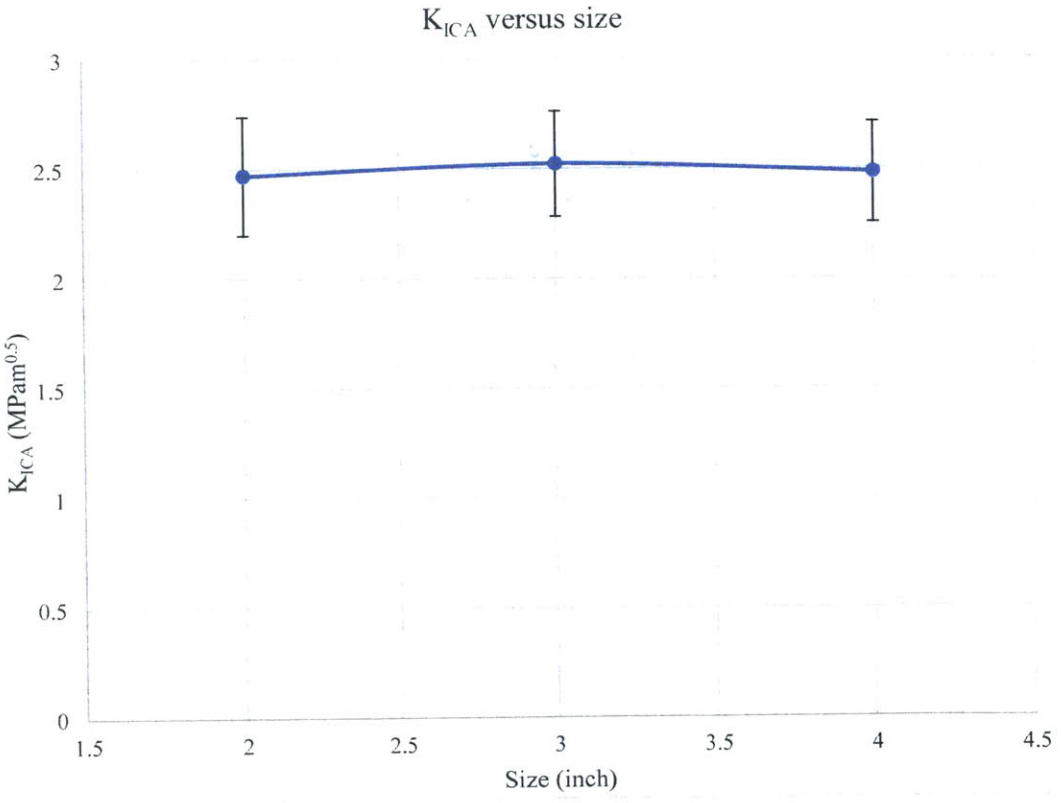

Figure 5.14 K_{ICA} changing with size (error bars represent standard deviation)

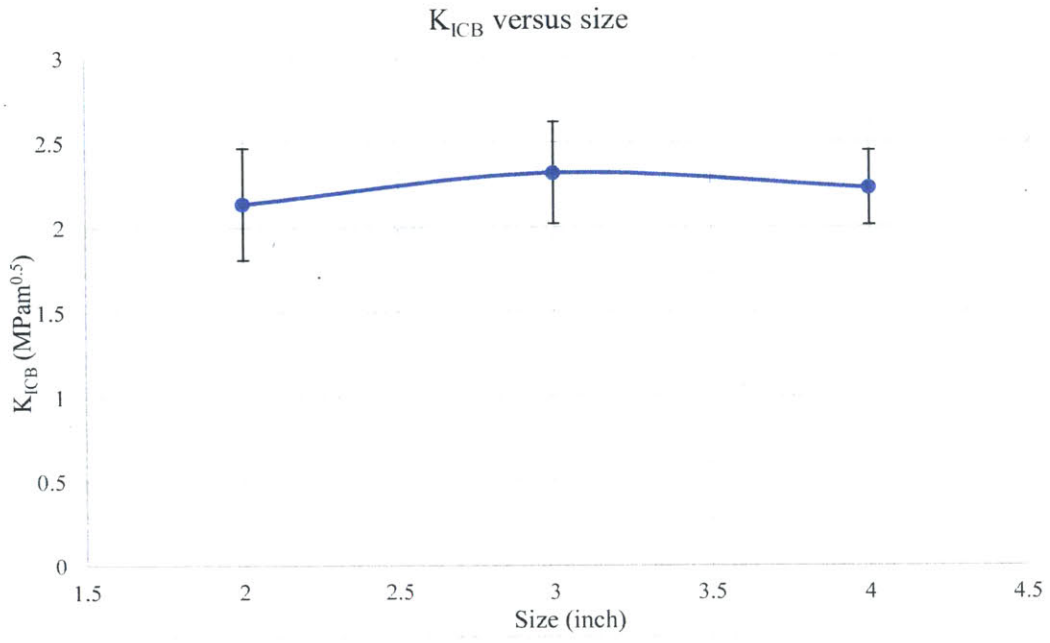

Figure 5.15 K_{ICB} changing with size (error bars represent standard deviation)

5.4.2 Discussion

Figure 5.10 illustrates that the elastic modulus decreases (from 18.35GPa to 16.03GPa) when the specimen size increases from two inches to three inches; then increases again (from 16.03GPa to 18.27GPa) when the specimen size increases from three inches to four inches. Elastic modulus is always considered to be a material property (Demkowicz, 2012; Anand, 2014). All the specimens (with different sizes) are cast from the same materials and with the same process. Therefore, the Elastic modulus for specimens with different sizes should be the same. The difference may be due to the installation of extensometers. As shown in Figure 5.16, the extensometers were attached to the specimen surface by rubber bands, and it was assumed that there is no relative movement between extensometers and the specimen surfaces. However, for the two-inch and four-inch specimens, the rubber bands used to attach the extensometers were relatively loose; while for the three-inch specimens, the rubber bands were relatively tight. Thus, for the two-inch and four-inch specimens, the extensometers might not be attached tightly and there might be relative movements (see Figure 5.16, Figure 5.17 and Figure 5.18). The measured displacement might be

underestimated due to the relative movement, so therefore, the elastic modulus might be overestimated.

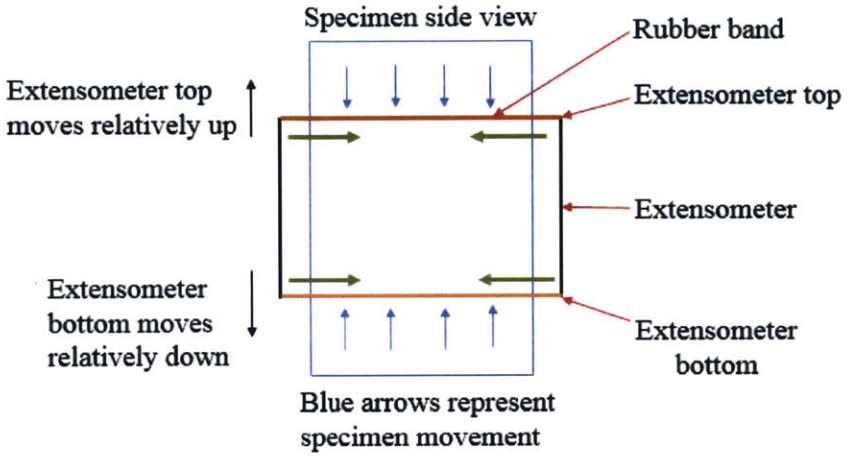

Figure 5.16 Illustration of the extensometer relative movements. Blue arrows represent the specimen movement during the tests (specimen is compressed). The orange lines represent the rubber bands, the black lines represent the extensometers, and the green arrows represent the force that the rubber bands exert on the extensometer tops and bottoms. For two-inch and four-inch specimens, the force exerted by the rubber bands might not be large enough. As a result, there might be relative movement between the extensometers and the specimen. The movements measured by the extensometers might be smaller than the actual specimen displacements, so therefore, the elastic modulus might be overestimated.

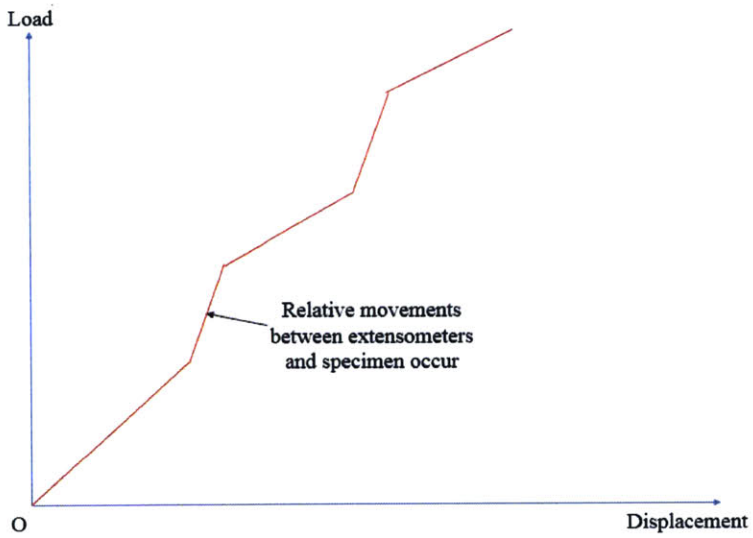

Figure 5.17 The load displacement curve (exaggerated) when relative movements occur. When relative movements occur, the measured displacement is lower than the real displacement. As a result, the slope becomes steeper.

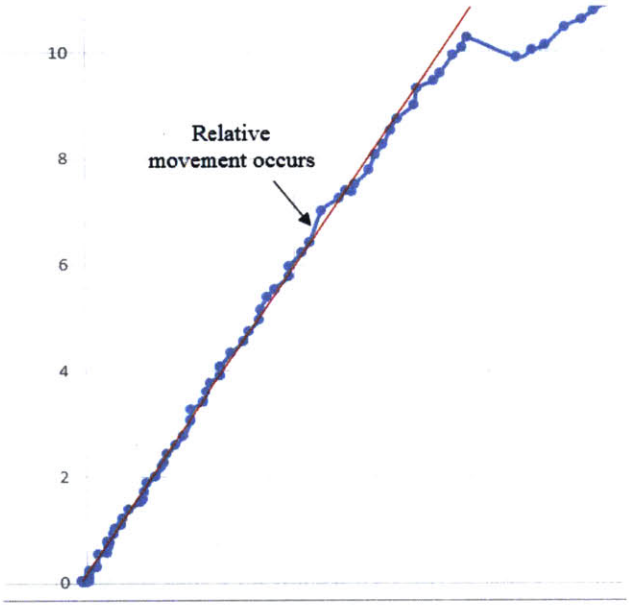

Figure 5.18 The load displacement curve for one test (the specimen size was two-inch). The red line is the averaged slope. In the test relative movements occurred (the black arrow shows a typical example for relative movements).

Figure 5.11 shows that the tensile strength is decreasing with increasing specimen size (the tensile strength for four-inch specimen is 69.6% of the tensile strength for two-inch specimen). This is in excellent agreement with the size effect theory: the tensile strength decreases with increasing size (Weibull, 1951; Glucklich and Cohen, 1967; Glucklich and Cohen, 1968; Einstein, 1970; Einstein, 1981; Demkowicz, 2012). The size effect theory has been explained in detail in Section 2.1.9.

Figure 5.12 shows that σ_A also decreases with size (the σ_A for four-inch specimen is 72.1% of the σ_A for two-inch specimen). In addition, Figure 5.13 shows that σ_B decreases with increasing size (the σ_B for four-inch specimen is 75.2% of the σ_B for two-inch specimen). Further investigations are required to explain these phenomena.

Table 5.2 and Figure 5.14 indicate that K_{ICA} is almost constant with different specimen sizes. On the contrary, Figure 5.15 shows that K_{ICB} increases slightly (from 2.14 $MPam^{0.5}$ to 2.32 $MPam^{0.5}$)

when the specimen size increases from two inches to three inches; then decreases slightly (from 2.32 $MPam^{0.5}$ to 2.23 $MPam^{0.5}$) when the specimen size increases from three inches to four inches. The averaged K_{ICB} for three-inch specimens is within the standard deviation range of K_{ICB} for two-inch specimens, so therefore, the size effect is not very obvious. In the fracture toughness calculation (see Equation 5.2), the term $1/\sqrt{R}$ may help to reduce the size effect. It is worth noting that the calculated fracture toughness is much higher than the fracture toughness of concrete. Demkowicz (2012) stated that the fracture toughness of concrete is usually taken as $1.2MPam^{0.5}$. Therefore, the reduction factor ϕ, which is dependent on 2α, may be eventually needed. The ϕ will not be correct until the fracture toughness is below $1.5MPam^{0.5}$. Further investigations need to be carried out to explain the change of K_{ICA} and K_{ICB}.

5.5 Experimental results for specimens with $2\alpha \approx 39°$ (the fourth and fifth batches of mortar specimens)

5.5.1 Experimental results for the fourth and five batches of mortar specimens

The experimental results for the fourth and fifth batches of mortar specimens are presented in Table A.16 through Table A.25 in Appendix A1. The E, σ_t, σ_A, σ_B, K_{ICA}, and K_{ICB} changing with size is summarized in Table 5.3 and Table 5.4, and Figure 5.19 through Figure 5.24 below.

Table 5.3 Summary of experimental results for the fourth and fifth batches of mortar ($2\alpha = 39°$)

Size	Mean of E (GPa)	SD of E (GPa)	Mean of σ_t (MPa)	SD of σ_t (MPa)	Mean of σ_A (MPa)	SD of σ_A (MPa)	Mean of σ_B (MPa)	SD of σ_B (MPa)	No. of specimens
2-inch	18.65	1.63	4.66	0.81	27.76	3.89	27.12	3.70	10
3-inch	16.79	1.63	3.75	0.38	22.68	1.76	22.08	1.62	10
4-inch	18.78	1.67	3.17	0.45	19.33	2.38	18.66	2.21	10

Table 5.4 Summary of experimental results for the fourth and fifth batches of mortar ($2\alpha = 39°$)

Size	Mean of K_{ICA} ($MPam^{0.5}$)	SD of K_{ICA} ($MPam^{0.5}$)	Mean of K_{ICB} ($MPam^{0.5}$)	SD of K_{ICB} ($MPam^{0.5}$)	No. of specimens
2-inch	3.04	0.39	2.97	0.38	10
3-inch	2.98	0.23	2.90	0.21	10
4-inch	2.87	0.35	2.77	0.32	10

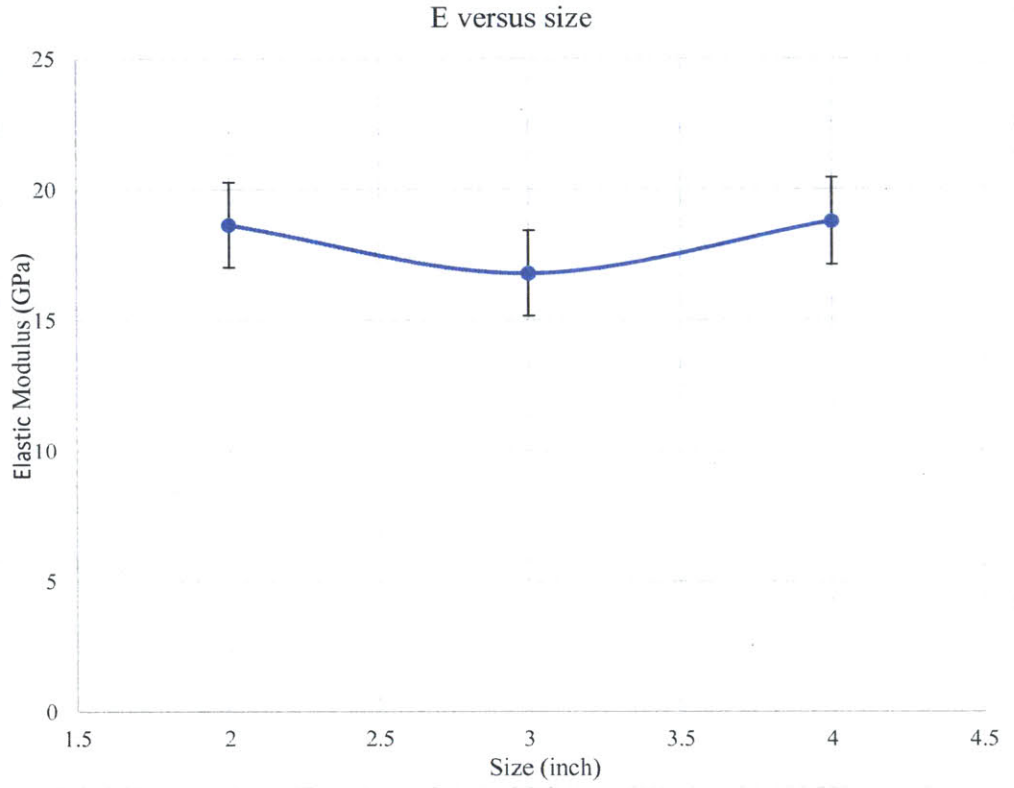

Figure 5.19 Elastic Modulus changing with size (error bars represent standard deviation)

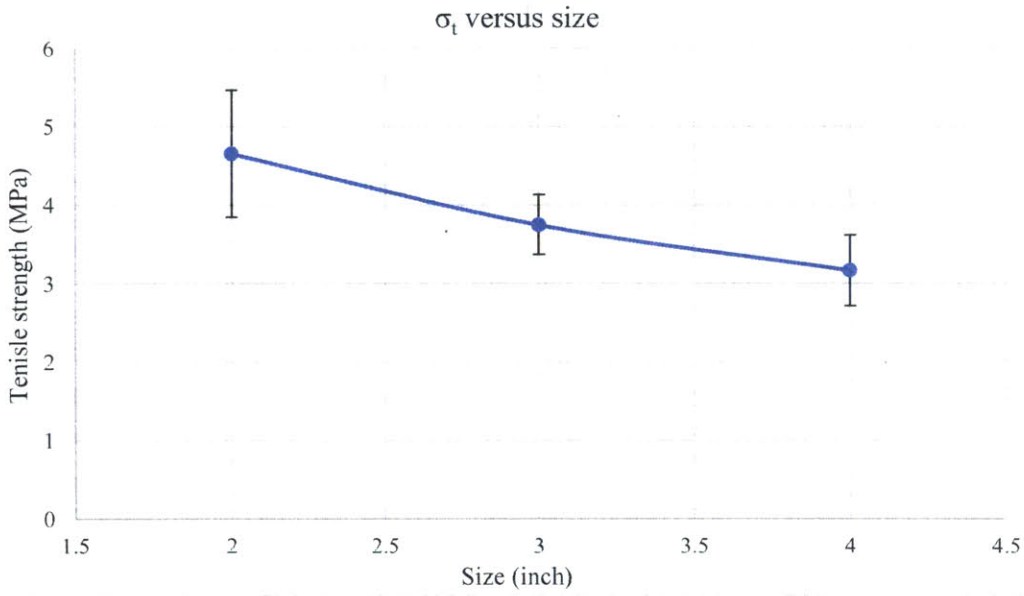

Figure 5.20 Tensile strength σ_t changing with size (error bars represent standard deviation)

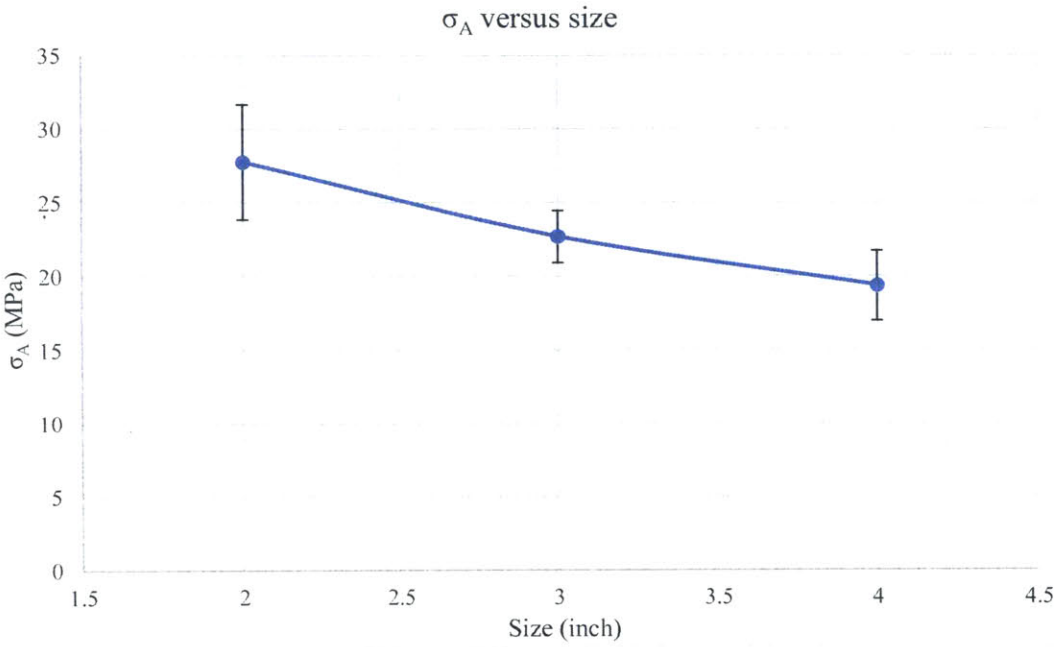

Figure 5.21 σ_A changing with size (error bars represent standard deviation)

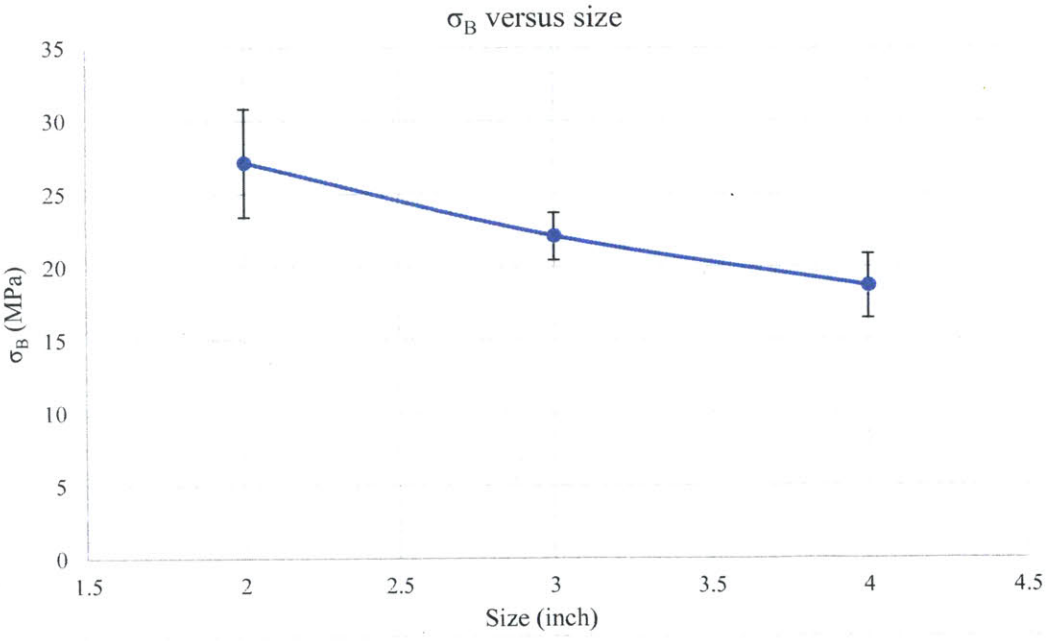

Figure 5.22 σ_B changing with size (error bars represent standard deviation)

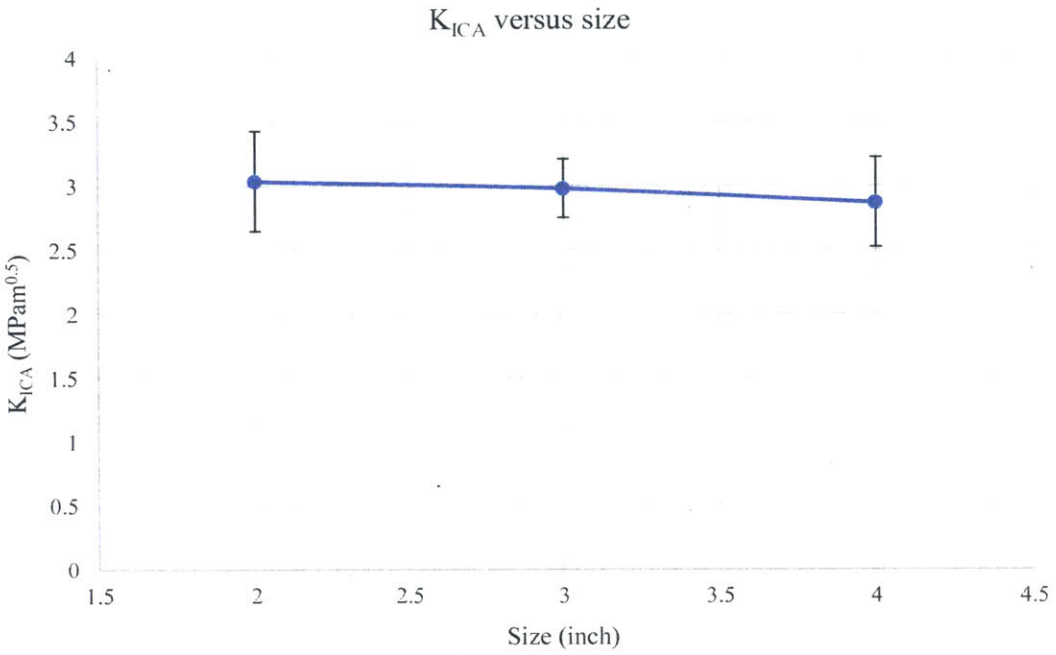

Figure 5.23 K_{ICA} changing with size (error bars represent standard deviation)

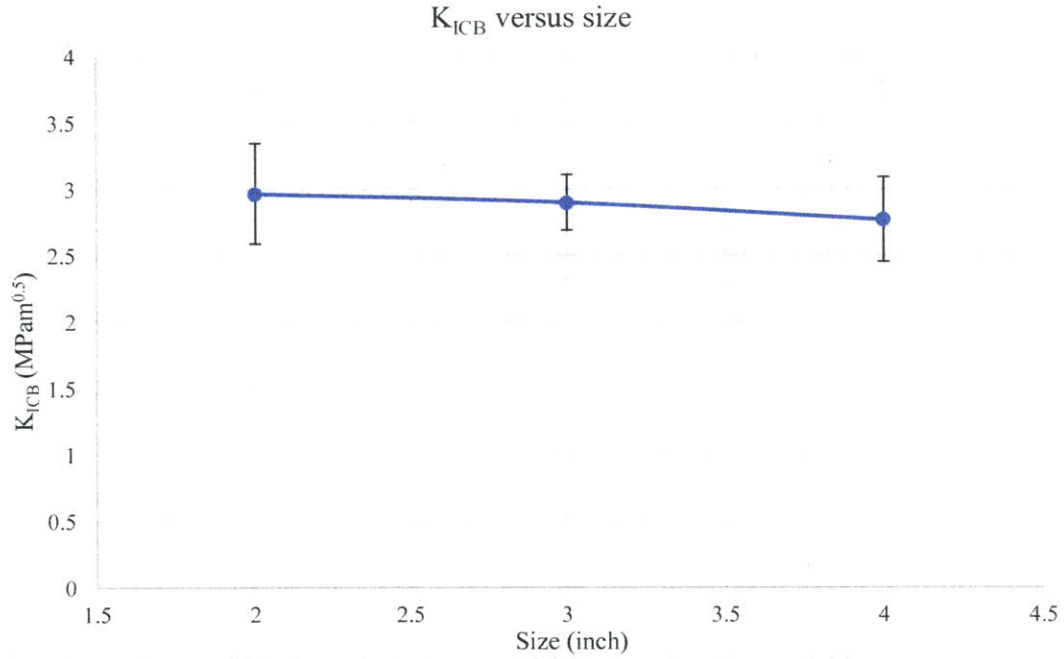

Figure 5.24 K_{ICB} changing with size (error bars represent standard deviation)

5.5.2 Discussion

Figure 5.19 shows that that the elastic modulus decreases (from 18.65GPa to 16.79GPa) when the specimen size increases from two inches to three inches; then increases again (from 16.79GPa to 18.78GPa) when the specimen size increases from three inches to four inches. This is similar to the E changing with size for the first three batches of mortar, and the reason has been discussed in Section 5.4.2.

Figure 5.20 shows that the tensile strength is decreasing with increasing specimen size (the tensile strength for four-inch specimen is 68.0% of the tensile strength for two-inch specimen). This is in excellent agreement with the size effect theory: the tensile strength decreases with increasing size (Weibull, 1951; Glucklich and Cohen, 1967; Glucklich and Cohen, 1968; Einstein, 1970; Einstein, 1981; Demkowicz, 2012). The size effect theory has been explained in detail in Section 2.1.9.

Figure 5.21 shows that σ_A also decreases with size (the σ_A for four-inch specimen is 69.6% of the σ_A for two-inch specimen); and Figure 5.22 shows that σ_B decreases with increasing size (the σ_B for four-inch specimen is 68.8% of the σ_B for two-inch specimen). Further investigations need to be conducted to explain these phenomena.

Figure 5.23 shows that K_{ICA} also decreases slightly with size (the K_{ICA} for four-inch specimen is 94.41% of the K_{ICA} for two-inch specimen). The size effect is not obvious since the averaged K_{ICA} for four-inch specimens is within the standard deviation range of the K_{ICA} for two-inch specimens. Figure 5.24 shows that K_{ICB} decreases with increasing size (the K_{ICB} for four-inch specimen is 93.27% of the K_{ICB} for two-inch specimen). Similar to K_{ICA}, the size effect is also not prominent since the averaged K_{ICB} for four-inch specimens is within the standard deviation range of the K_{ICB} for two-inch specimens. In the fracture toughness calculation (see Equation 5.2), the term $1/\sqrt{R}$ may help to reduce the size effect. It is worth noting that the calculated fracture toughness is much higher than the fracture toughness of concrete. Demkowicz (2012) stated that the fracture toughness of concrete is usually taken as $1.2MPam^{0.5}$. Therefore, the reduction factor ϕ, which is dependent on 2α, may be eventually needed. The ϕ will not be correct until the fracture toughness is below $1.5MPam^{0.5}$. Further investigations need to be carried out to explain the fracture toughness change.

5.6 Experimental results for specimens with $2\alpha \approx 23°$ (the sixth and seventh batches of mortar specimens)

5.6.1 Experimental results summary for the sixth and seventh batches of mortar

The experimental results for the sixth and seventh batches of mortar specimens are presented in Table A.26 through Table A.35 in Appendix A1. The E, σ_t, σ_A, σ_B, K_{ICA}, and K_{ICB} changing with size is summarized in Table 5.5 and Table 5.6, and Figure 5.25 through Figure 5.30 below.

Table 5.5 Summary of experimental results for the sixth and seventh batches of mortar ($2\alpha = 23°$)

Size	Mean of E (GPa)	SD of E (GPa)	Mean of σ_t (MPa)	SD of σ_t (MPa)	Mean of σ_A (MPa)	SD of σ_A (MPa)	Mean of σ_B (MPa)	SD of σ_B (MPa)	No. of specimens
2-inch	19.28	1.54	4.58	0.44	35.19	3.43	31.59	3.08	10
3-inch	18.51	2.69	3.86	0.32	30.84	2.90	27.43	2.76	9
4-inch	18.87	1.82	3.19	0.30	25.38	2.52	22.86	2.17	10

Table 5.6 Summary of experimental results for the sixth and seventh batches of mortar ($2\alpha = 23°$)

Size	Mean of K_{ICA} ($MPam^{0.5}$)	SD of K_{ICA} ($MPam^{0.5}$)	Mean of K_{ICB} ($MPam^{0.5}$)	SD of K_{ICB} ($MPam^{0.5}$)	No. of specimens
2-inch	2.30	0.22	2.06	0.22	10
3-inch	2.39	0.20	2.13	0.20	9
4-inch	2.24	0.23	2.02	0.20	10

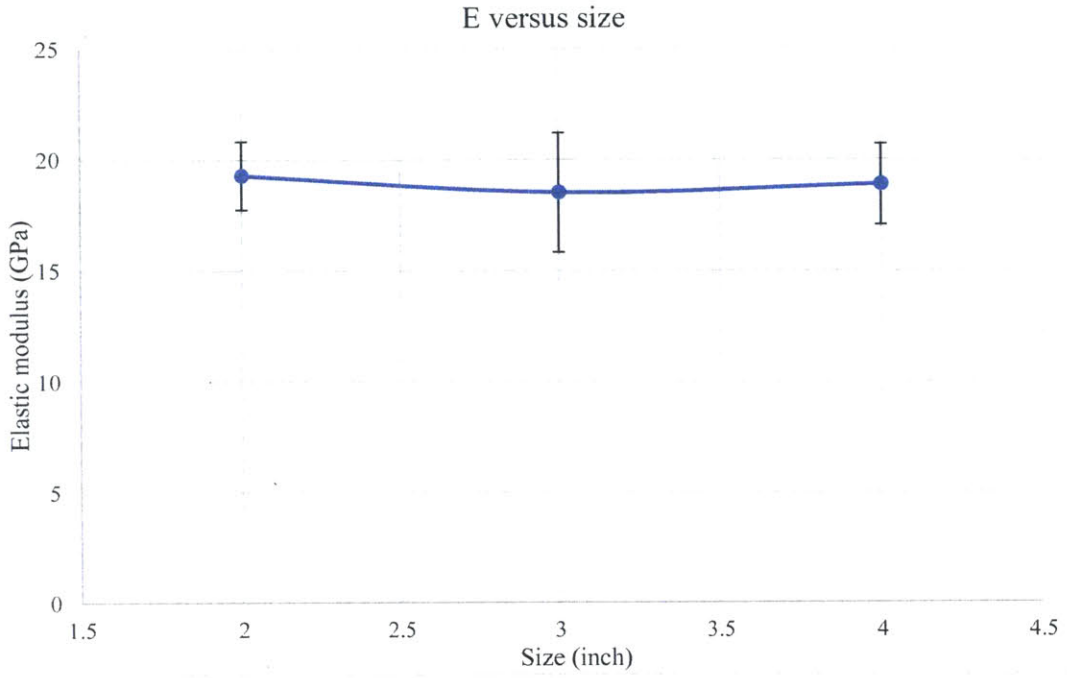

Figure 5.25 Elastic modulus changing with size (error bars represent standard deviation)

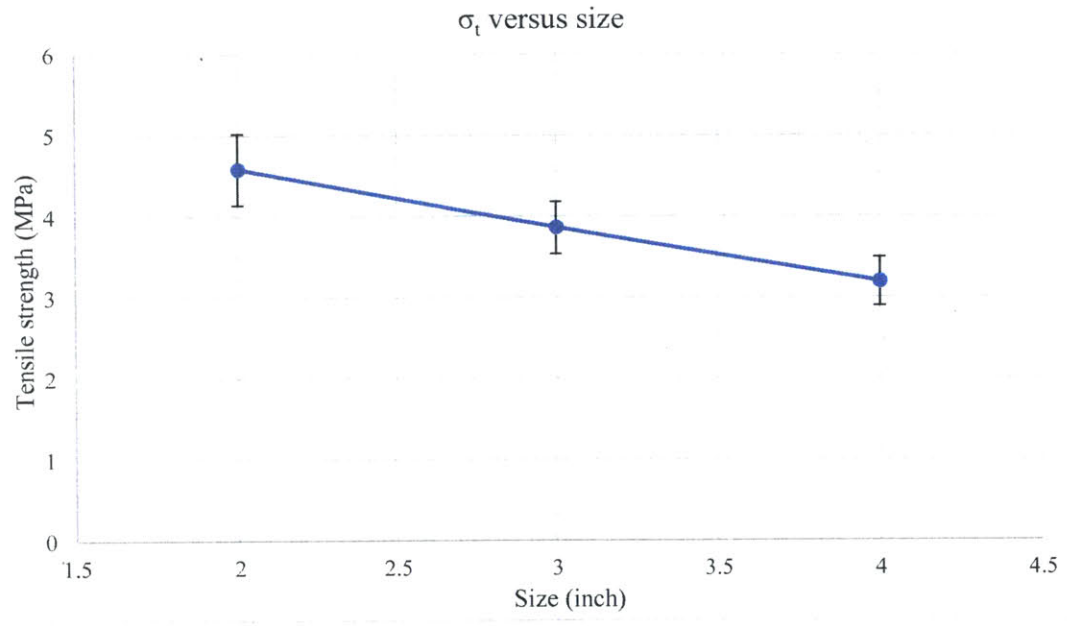

Figure 5.26 Tensile strength changing with size (error bars represent standard deviation)

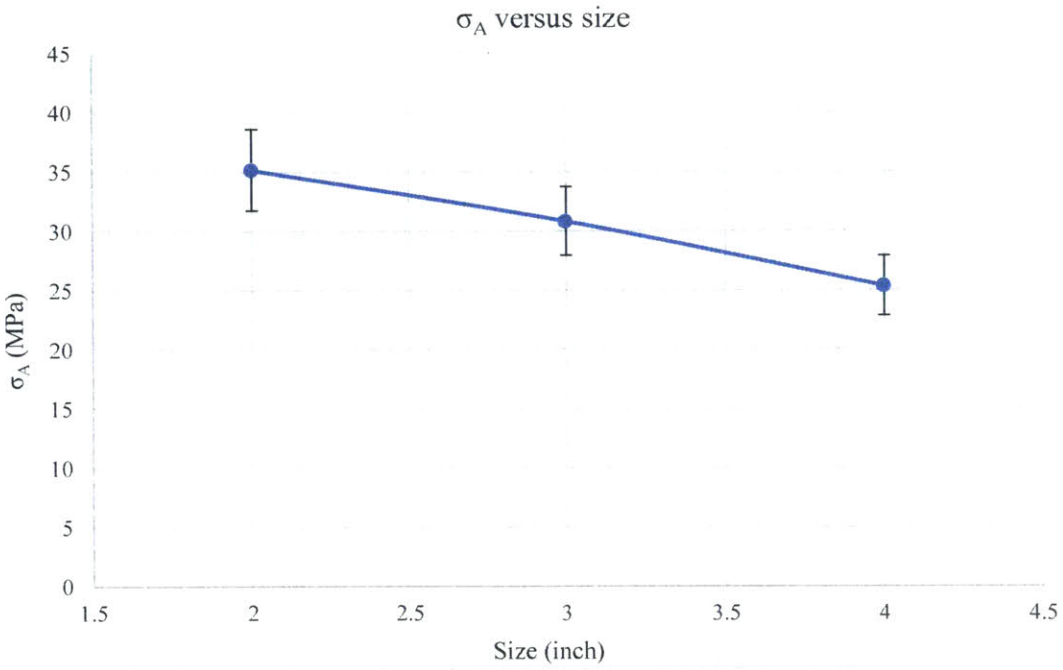

Figure 5.27 σ_A changing with size (error bars represent standard deviation)

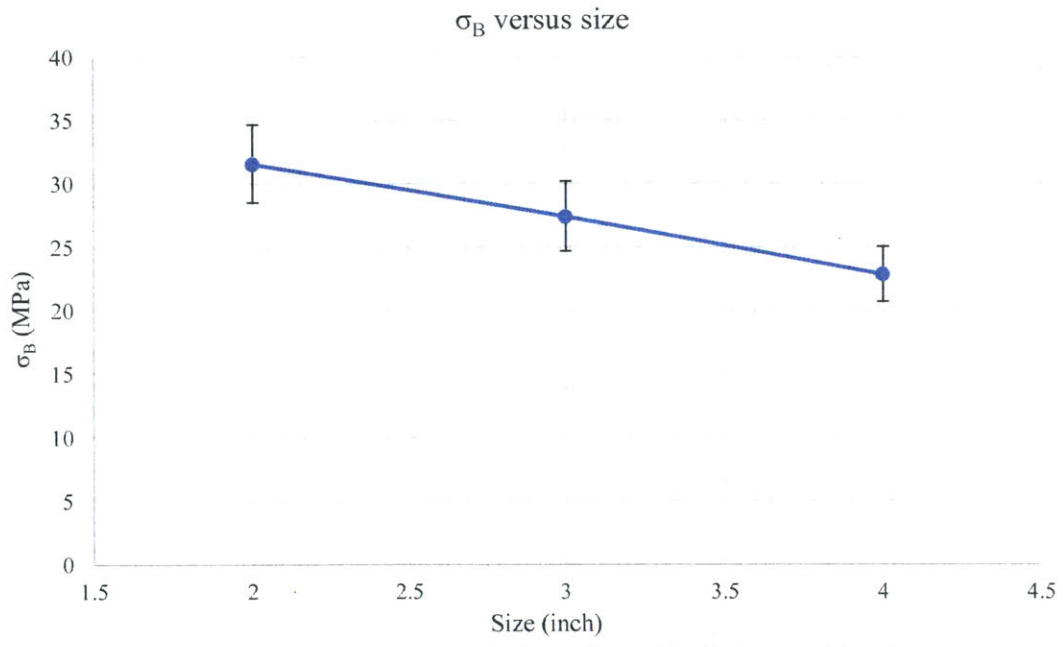

Figure 5.28 σ_B changing with size (error bars represent standard deviation)

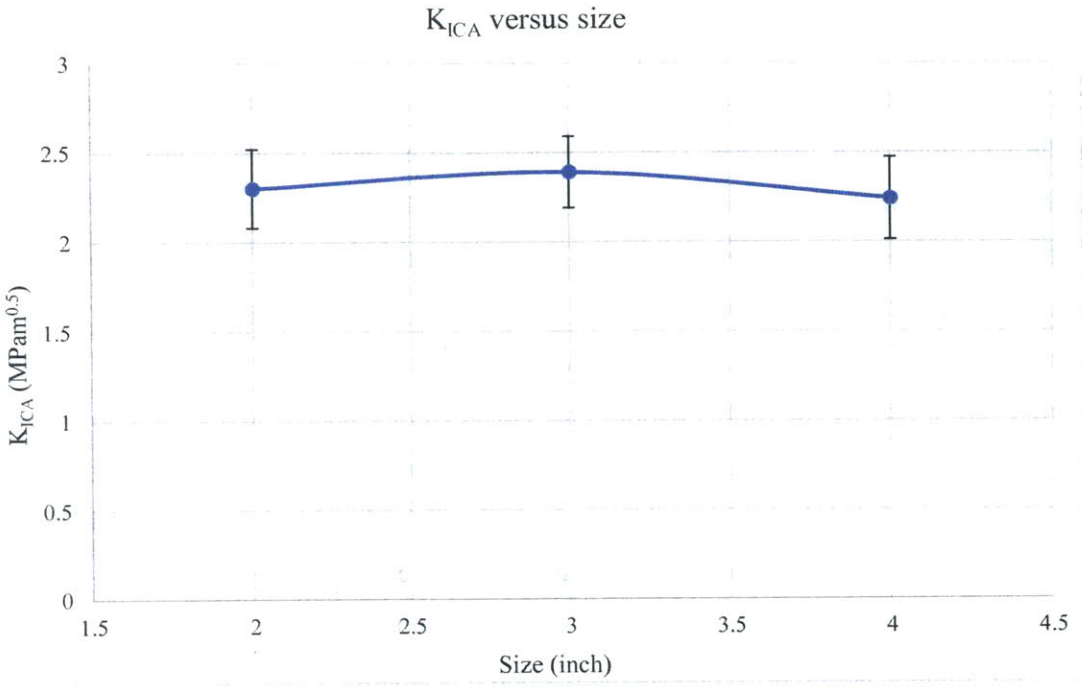

Figure 5.29 K_{ICA} changing with size (error bars represent standard deviation)

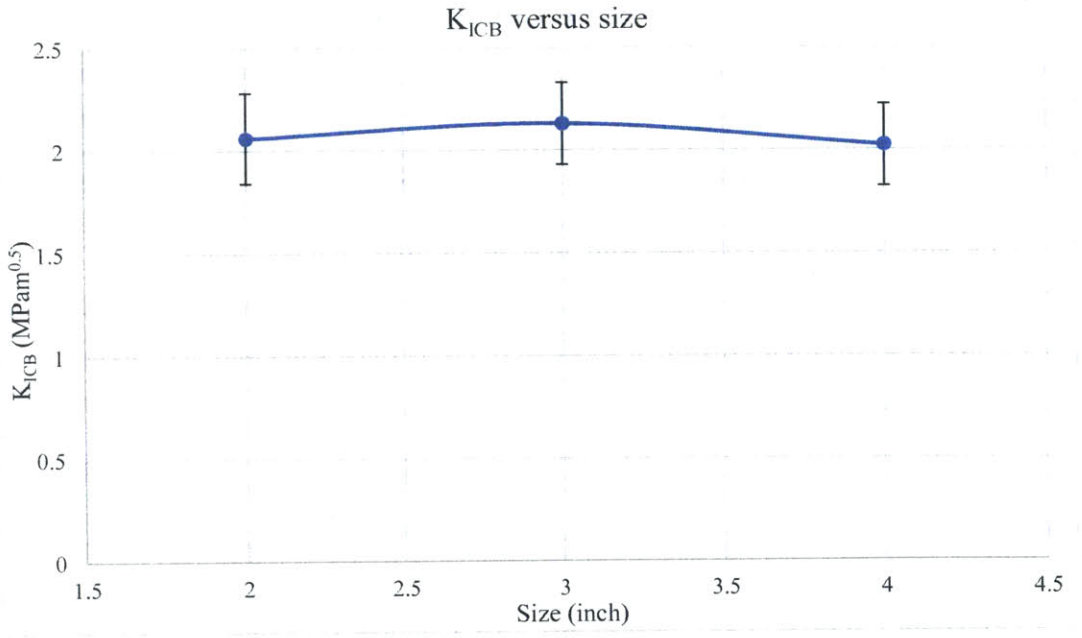

Figure 5.30 K_{ICB} changing with size (error bars represent standard deviation)

5.6.2 Discussion

Figure 5.25 illustrates that the elastic modulus decreases slightly (from 19.28GPa to 18.51GPa) when the specimen size increases from two-inch to three-inch; then increases slightly (from 18.51GPa to 18.87GPa) when the specimen size increases from three-inch to four-inch. It is worth noting that the difference between the elastic modulus of the two-inch specimens and the three-inch specimens for 23° specimens is less than the difference for 28° specimens or 39° specimens. As discussed in Section 5.4.2, for the two-inch and four-inch specimens, the extensometers might not be attached tightly by the rubber bands. The measured displacements might be lower than the real displacements so the elastic modulus might be overestimated. For the three-inch specimens of the sixth and seventh batches of mortar, relatively loose rubber bands were used to attach the extensometers, instead of the tight rubber bands which were used for the three-inch specimens of the first five batches of mortar. As a result, the elastic modulus for the three-inch specimens might also be overestimated so the difference became relatively smaller.

Figure 5.26 shows that the tensile strength is decreasing with increasing specimen size (the tensile strength for four-inch specimen is 69.7% of the tensile strength for two-inch specimen). This is in excellent agreement with the size effect theory: the tensile strength decreases with increasing size (Weibull, 1951; Glucklich and Cohen, 1967; Glucklich and Cohen, 1968; Einstein, 1970; Einstein, 1981; Demkowicz, 2012). The size effect theory has been explained in detail in Section 2.1.9.

Figure 5.27 illustrates that σ_A decreases with size (σ_A for four-inch specimen is 72.1% of σ_A for two-inch specimen). Figure 5.28 shows that σ_B also decreases with increasing size (σ_B for four-inch specimen is 72.4% of σ_B for two-inch specimen). Further investigations need to be conducted to explain these phenomena.

Figure 5.29 shows that K_{ICA} increases slightly (from 2.30MPam$^{0.5}$ to 2.39MPam$^{0.5}$) when the specimen size increases from two-inch to three-inch; then decreases slightly (from 2.39MPam$^{0.5}$ to 2.24MPam$^{0.5}$) when the specimen size increases from three-inch to four-inch. The size effect for K_{ICA} is not significant because the averaged K_{ICA} for four-inch specimens is within the standard deviation range of the K_{ICA} for three-inch specimens. Figure 5.30 shows that K_{ICB} increases slightly (from 2.06MPam$^{0.5}$ to 2.13MPam$^{0.5}$) when the specimen size increases from two-inch to three-inch; then decreases slightly (from 2.13MPam$^{0.5}$ to 2.02MPam$^{0.5}$) when the specimen size

increases from three-inch to four-inch. The size effect for K_{ICB} is also not remarkable because the averaged K_{ICB} for four-inch specimens is also within the standard deviation range of the K_{ICB} for three-inch specimens. In the fracture toughness calculation (see Equation 5.2), the term $1/\sqrt{R}$ may help to reduce the size effect. It is worth noting that the calculated fracture toughness is much higher than the fracture toughness of concrete. Demkowicz (2012) stated that the fracture toughness of concrete is usually taken as $1.2MPam^{0.5}$. Therefore, the reduction factor ϕ, which is dependent on 2α, may be eventually needed. The ϕ will not be correct until the fracture toughness is below $1.5MPam^{0.5}$. Further investigations need to be carried out to explain the fracture toughness change.

5.7 Elastic modulus, tensile strength, σ_A and σ_B changing with 2α

5.7.1 Elastic modulus changing with 2α

The elastic modulus changing with 2α is summarized in Table 5.7 and Figure 5.31 below.

Table 5.7 Elastic modulus changing with 2α

Size (inch)	Averaged E (GPa)		
	23°	28°	39°
2	19.28	18.35	18.65
3	18.51	16.03	16.79
4	18.87	18.27	18.78

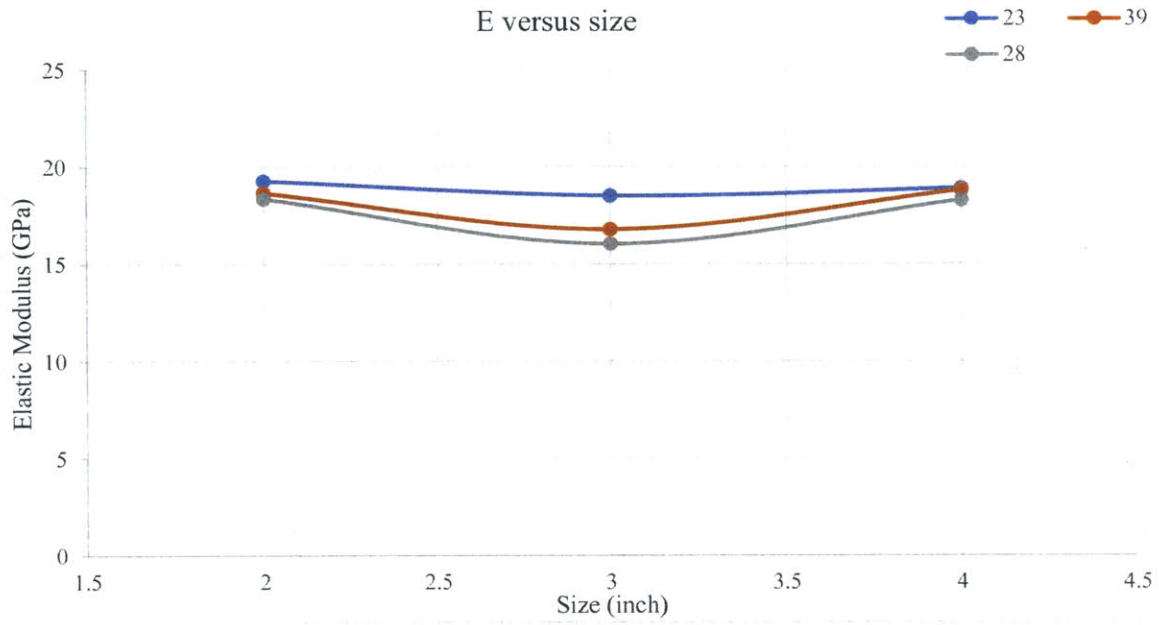

Figure 5.31 Elastic modulus changing with 2α (Blue line represents 23°, grey line represents 28°, and orange line represents 39°)

From Figure 5.31, the elastic modulus (E) is almost independent on 2α when the specimen size is two-inch or four-inch. For three-inch specimens, the elastic modulus for 23° specimens is slightly larger than the elastic modulus for 28° or 39° specimens. The reasons have been explained in Section 5.6.2.

5.7.2 Tensile strength changing with 2α

The tensile strength changing with 2α is summarized in Table 5.8 and Figure 5.32 below.

Table 5.8 Tensile strength changing with 2α

Size (inch)	σ_t (MPa)		
	23°	28°	39°
2	4.58	4.60	4.66
3	3.86	3.81	3.75
4	3.19	3.20	3.17

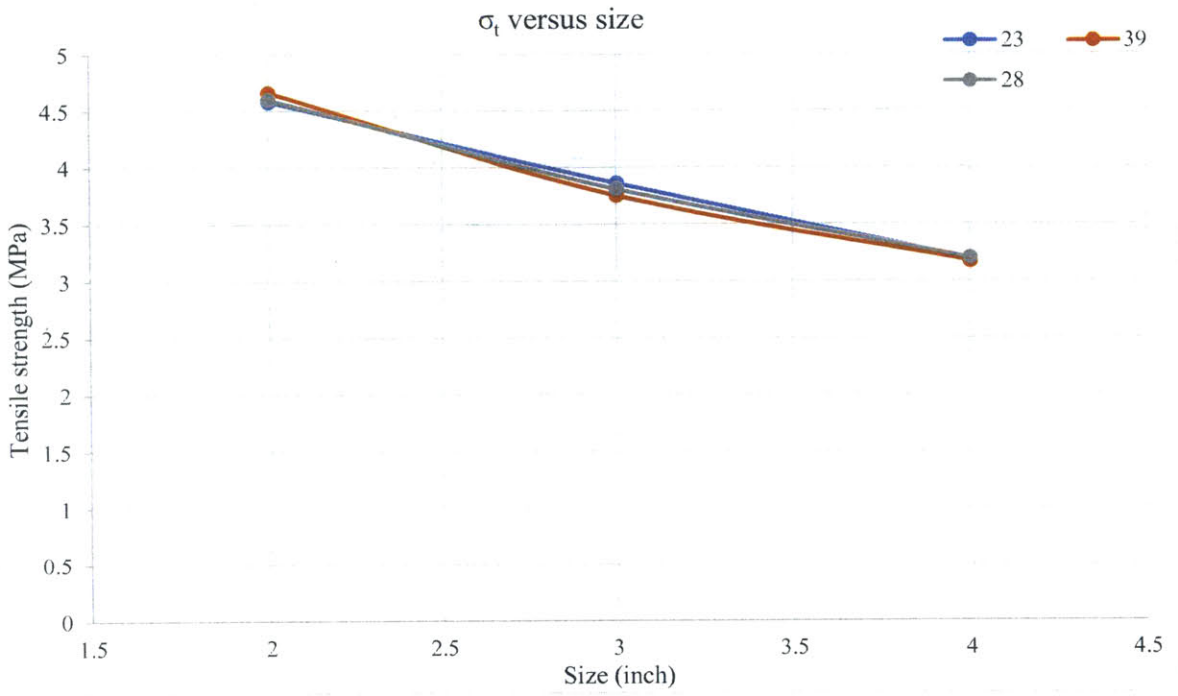

Figure 5.32 Tensile strength changing with 2α (Blue line represents 23°, grey line represents 28°, and orange line represents 39°)

Figure 5.32 shows that the tensile strength is almost independent of 2α.

5.7.3 σ_A changing with 2α

σ_A changing with 2α is summarized in Table 5.9 and Figure 5.33 below.

Table 5.9 σ_A changing with 2α

Size (inch)	σ_A (MPa)		
	23°	28°	39°
2	35.19	31.89	27.76
3	30.84	26.90	22.68
4	25.38	22.99	19.33

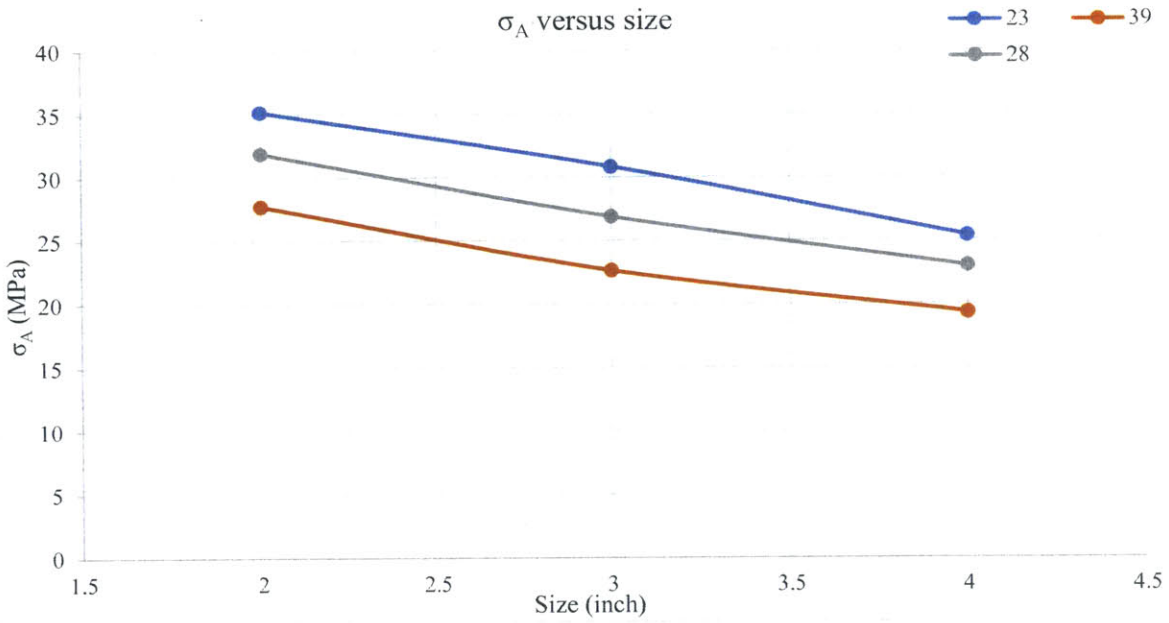

Figure 5.33 σ_A changing with 2α (Blue line represents 23°, grey line represents 28° and orange line represents 39°)

Figure 5.33 shows that σ_A decreases with increasing 2α. This means that when 2α is increasing, the averaged vertical compressive stress required to initiate the tensile crack is decreasing. Hence, σ_A varies with both size and 2α, while σ_t only varies with size. Further investigations are required to explain this phenomenon.

5.7.4 σ_B changing with 2α

σ_B changing with 2α is summarized in Table 5.10 and Figure 5.34 below.

Table 5.10 σ_B changing with 2α

Size (inch)	σ_B (MPa)		
	23°	28°	39°
2	31.59	27.63	27.12
3	27.43	24.74	22.08
4	22.86	20.77	18.66

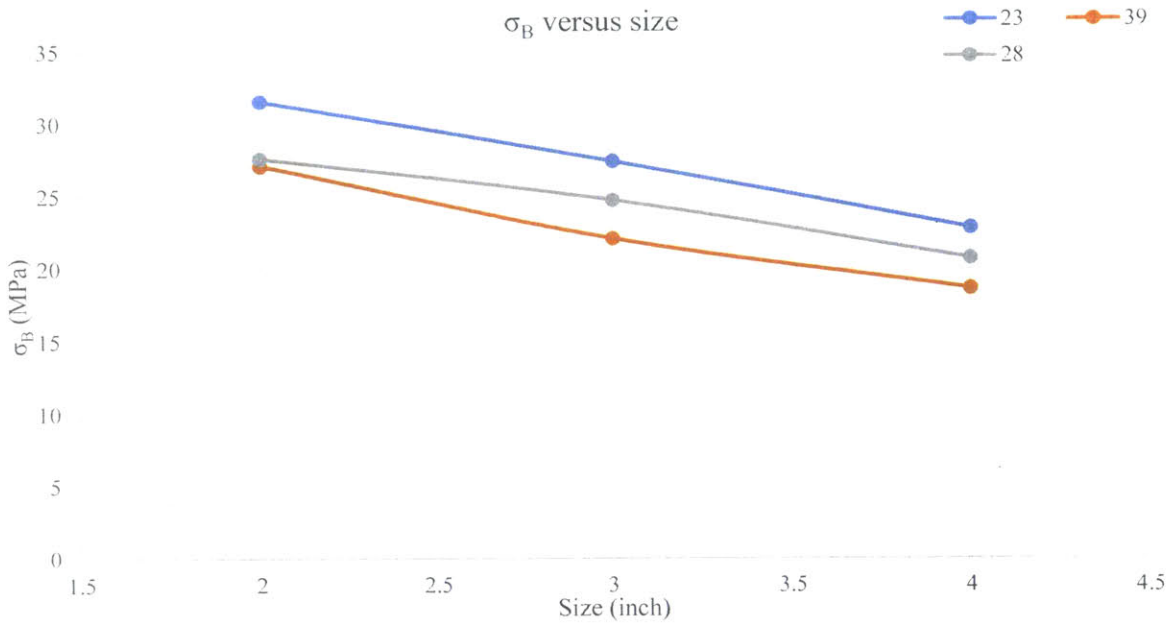

Figure 5.34 σ_B changing with 2α (Blue line represents 23°, grey line represents 28° and orange line represents 39°)

Figure 5.34 shows that σ_B decreases with increasing 2α. Further investigations need to be conducted to explain the change.

5.8 High speed camera and high resolution camera

A high speed camera and a high resolution camera were used for two three-inch specimens (with $2\alpha \approx 28°$) to examine the crack initiation position and the crack length. Both tests verified that the crack initiated at the specimen center, and the crack length was approximately 70% of the specimen diameter.

5.8.1 Specimen one

The high resolution image showing the crack initiation position and the primary tensile crack after the crack propagation is shown in Figure 5.35. Then, the crack initiation and propagation are traced from the high speed video. The traces of crack initiation and propagation are shown in Figure 5.36

through Figure 5.38. It is difficult to see the crack propagation from the snapshots of high speed video, so only the traces are shown here.

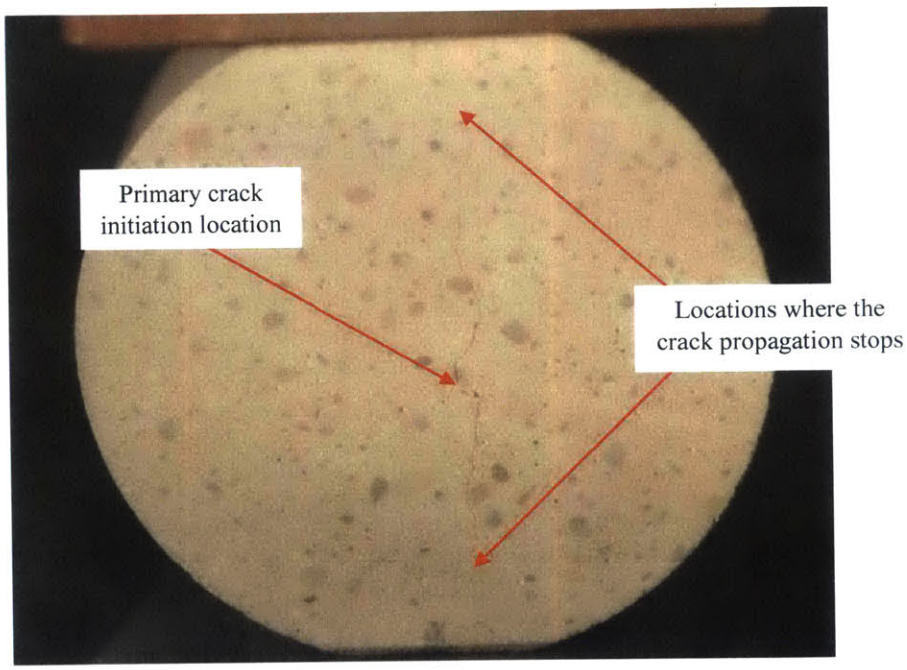

Figure 5.35 Primary tensile crack after crack propagation

Figure 5.36 Trace of crack initiation. Two parallel lines at the top and bottom represent the flattened surfaces (for the trace length and location reference).

Figure 5.37 Trace of the crack during the crack propagation

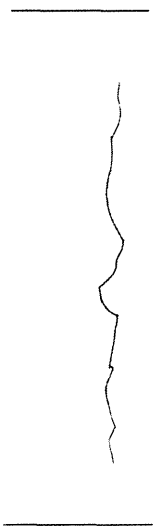

Figure 5.38 Trace of the crack right after the crack propagation

The camera was stopped before the total failure occurred. Therefore, there is no photo showing the total failure for specimen one. Also, the stress strain curve is wrong. In this test, a mistake was

made that the actuator was not turned on. As a result, the loading became loading rate controlled instead of displacement rate controlled (the loading was increased throughout the test instead of the displacement) so therefore, the loading drop cannot be seen in the stress strain curve. In addition, the displacement measured by the machine is wrong. Figure 5.39 shows the stress strain curve. For some parts of the curve, when the stress increases, the strain decreases, which is not realistic. Therefore, the stress strain curve cannot be used so the trace of the crack initiation and propagation cannot be related to the stress strain curve.

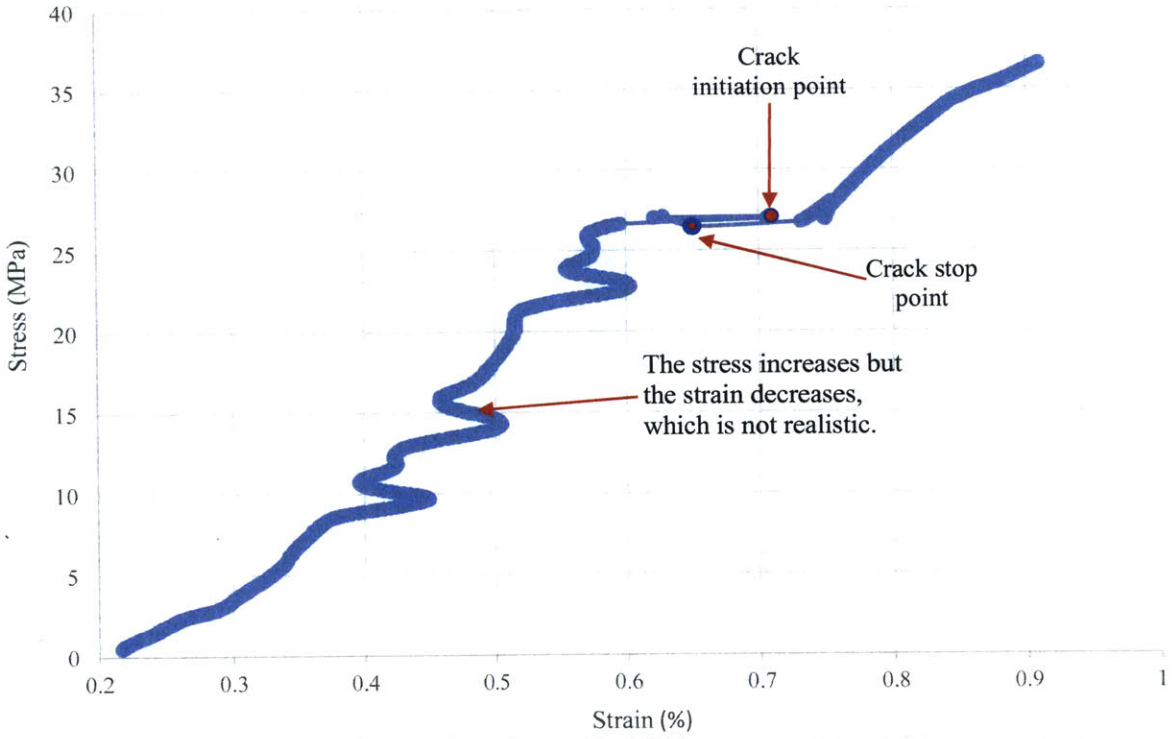

Figure 5.39 The stress strain curve for specimen one

5.8.2 Specimen two

The crack initiation position and the primary tensile crack after the crack propagation are shown in Figure 5.40. Figure 5.40 verifies that crack initiates in the central region, and the crack propagates along the center line. Figure 5.41 shows the final failure of the specimen and this failure can be considered as compressive failure.

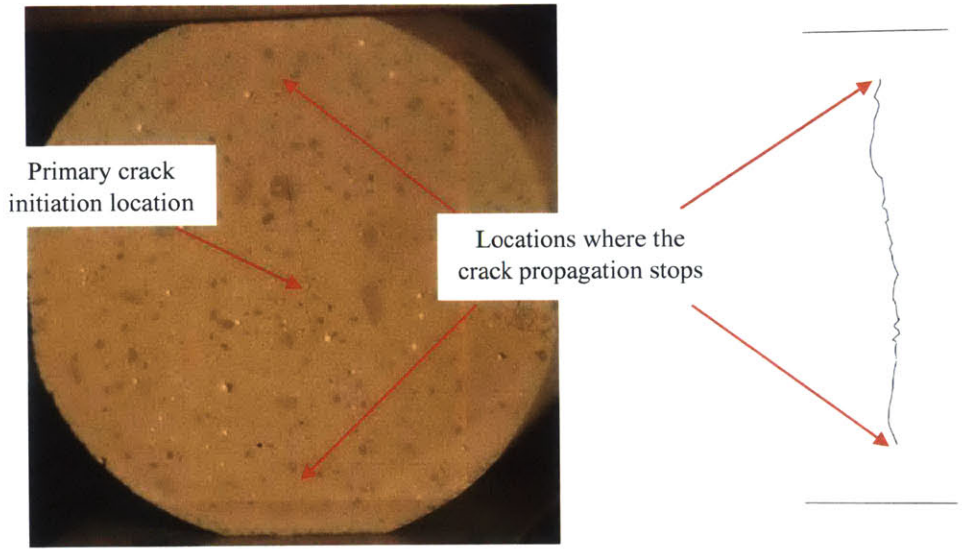

Figure 5.40 High resolution image and trace of primary tensile crack after the crack propagation

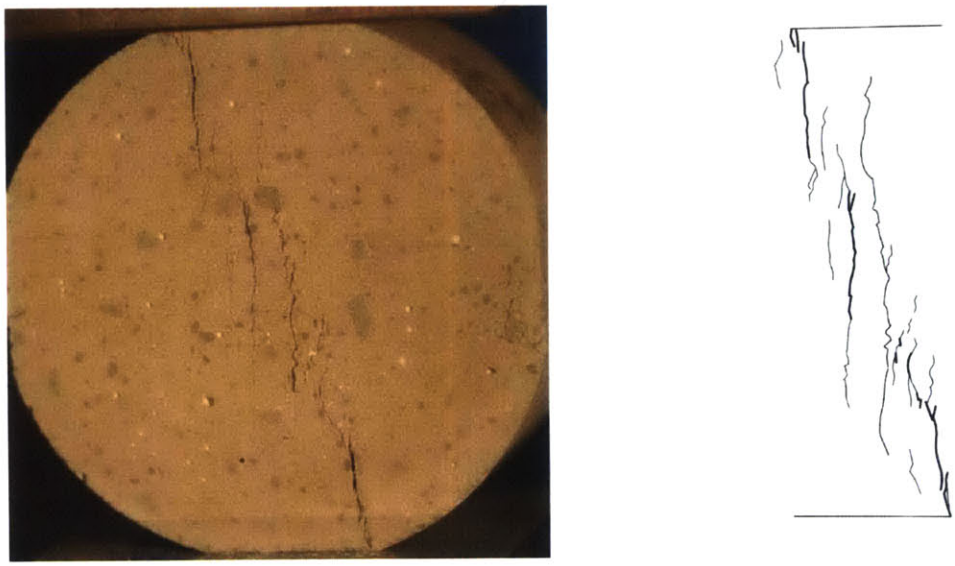

Figure 5.41 High resolution image and trace of total compressive failure.

In both two experiments, the high speed camera was continuously recording and once it was triggered by the laptop, the last 1.8 seconds of high speed frames was stored (Chapter 3 discusses this in detail). In this experiment, unfortunately, the high speed camera was triggered so late that the primary tensile crack initiation and propagation occurred before the last 1.8 seconds. As a result, the crack initiation and propagation were not captured by the high speed video. The crack initiation

point and the crack stopping point cannot be related to the stress strain curve, so the stress strain curve becomes useless. Thus, the stress strain curve is not shown, so the traces in Figure 5.40 and Figure 5.41 are not related to the stress strain curve.

It is worth noting that during the tests, the hydraulic jack also deformed linearly, so the hydraulic jack acted as a spring (see Figure 5.42). During the crack propagation, the vertical displacement of the specimen increased. As a result, the hydraulic jack might expand vertically, and some stored elastic energy might be released. The released energy might go into the specimen and drive the crack to propagate even further.

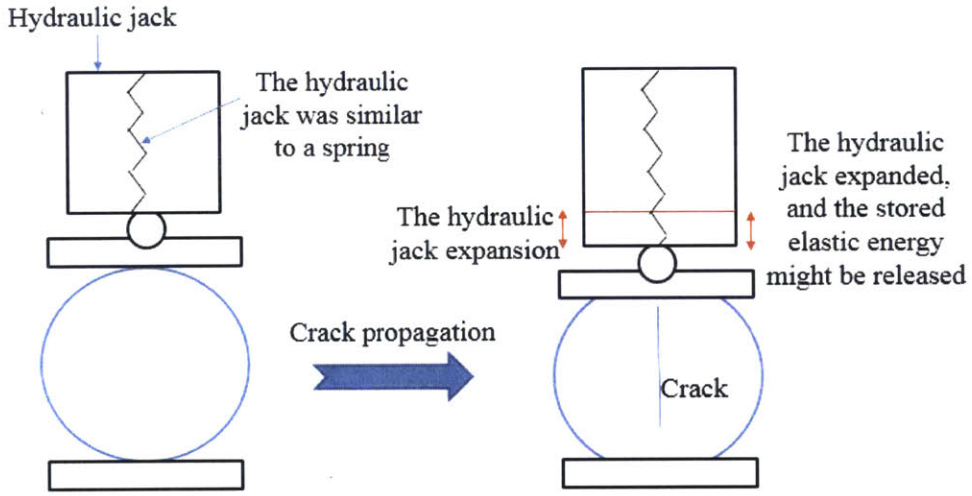

Figure 5.42 Hydraulic jack expansion

5.9 The measurement error in P_B (Loading at point B, see Figure 5.5)

During the test, the real loading right after the crack initiation might not be captured due to low sampling frequency. The high speed video proves that the primary crack propagation (the load drop) is within 0.1 seconds. However, the loading sampling rate for the first five batches of mortar is 1Hz and for the last two batches of mortar is 0.1Hz. Therefore, the loading may start to increase again before the data acquisition system measures the loading after crack initiation (see Figure 5.43).

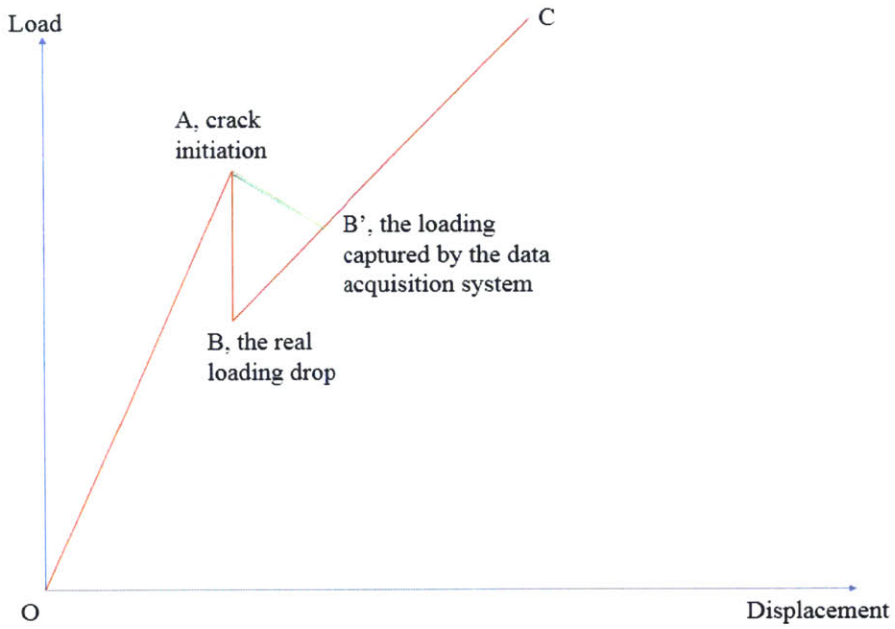

Figure 5.43 Illustration of the possible problem in loading capture

Figure 5.43 illustrates the possible problem in the loading capture process. In the figure, the red line represents the *assumed* load displacement curve and the green line represents the *measured* load displacement curve. As stated above, the loading drops within a very short time and the data acquisition system fails to capture the loading at point B. Instead, the loading at point B' is measured when the loading starts to increase again. Therefore, the loading at point B' becomes the measured P_B, and the green line is the measured load displacement curve. Thus, P_B may be overestimated and as a result, σ_B (the *averaged compressive stress* acting on the flattened surfaces at point B) will also be overestimated.

5.10 Summary

In short, σ_t, σ_A, and σ_B decrease with increasing specimen sizes. On the contrary, K_{ICA} and K_{ICB} do not change much with size. The two tests with high speed camera and high resolution camera verified that the primary crack initiated at the center of the specimen and propagated along the vertical center line.

Chapter 6 Conclusions and Future Research

6.1 Summary and conclusions

This research intends to investigate the size effect on fracture toughness of mortar through flattened Brazilian tests. To achieve this goal, a literature review, numerical analyses, and experiments were conducted.

Basic fracture mechanics, which include Linear Elastic Fracture Mechanics, and fracture of brittle and quasi-brittle materials, were reviewed. In addition, the methods for calculating elastic modulus, tensile strength, and fracture toughness were examined. The fracture toughness calculation methods discussed in previous articles are not convincing, since the underlying assumptions have not been verified by experiments. Specifically, whether the crack starts to propagate near the local minimum loading (see P_B in Figure 5.5) has not been verified by experiments.

Then, numerical analyses were carried out because the methods for tensile strength- and elastic modulus calculation reported in the literature are not satisfactory. The methods for tensile strength- and elastic modulus calculation assume that the flattened specimen is subjected to a uniformly distributed loading (uniform stress over the flattened surface). In this research project, however, a point load was applied to the loading plate by the hydraulic jack (see Figure 4.2). As a result, the displacement along the flattened surface was uniform but the stress distribution along the flattened surface was non-uniform. Thus, numerical analyses were required to determine the tensile strength and elastic modulus accurately. During the tests, the extensometer displacements and the local maximum loading (see P_A in Figure 5.5) were measured. With them, the elastic modulus and tensile strength were determined by finite element analysis.

Next, experimental results were shown. Cylindrical mortar specimens were cast from Type III Portland cement, fine-grained silt, and water, at a weight ratio of cement: silt: water = 2:2:1. The cylindrical specimens were then cut into small disks and flattened. The Brazilian tests were conducted by loading the flattened disks at a constant displacement rate, and the loading as well as the displacement (of mortar alone) were measured. 126 experiments with different specimen sizes (two-inch, three-inch and four inch) and different flatness angles (23°, 28°, and 39°) were run, from which 107 experimental results were accepted. Specifically, the load displacement curve

was used to determine the local maximum and minimum loading (see P_A and P_B in Figure 5.5). These loads were then used to calculate the fracture toughness, based on the local maximum loading, K_{ICA}, and the local minimum loading, K_{ICB}. In addition, the elastic modulus E, tensile strength σ_t, averaged compressive stress at local maximum loading σ_A, and averaged compressive stress at local minimum loading σ_B were determined. Two tests with high speed camera and high resolution camera were conducted. They showed that the primary crack initiated at the center of the specimen and propagated along the vertical center line.

The change of K_{ICA} and K_{ICB} with size and flatness angle was analyzed. Most importantly, the effect of size and flatness angle on E, σ_t, σ_A, and σ_B were investigated. The results indicate that σ_t, σ_A, and σ_B decrease with increasing specimen sizes. On the contrary, E, K_{ICA}, and K_{ICB} do not change much with size. In addition, σ_t appears to be independent on 2α, while σ_A and σ_B decrease with increasing 2α.

6.2 Recommendations for future research

The recommendations are summarized below:

1. A high speed camera should be used to examine where the crack starts to propagate between P_A and P_B.
2. Numerical analyses are required to verify the Wang's (2004) ϕ versus a/R curve.
3. Numerical work and analytical work needs to be conducted to derive an empirical or analytical formula to calculate the fracture toughness for flattened Brazilian tests.
4. Data with higher sampling frequency should be used to measure P_B more accurately.
5. More specimens need to be tested (at least 15 more per each 2α per each size) so the experimental results will be statistically convincing.

References

1) Agaiby, S. S. W. (2013) *Fracture Characterization of Clays and Clay-Like Materials Using Flattened Brazilian Test*. SM. Thesis. Massachusetts Institute of Technology.
2) Anand, L. (2014) Chapter 17: Linear Elastic Fracture Mechanics. *Lecture notes: 2.071 Mechanics of Solids*, Massachusetts Institute of Technology.
3) Anderson, T. L. (2005) *Fracture Mechanics: Fundamentals and Applications*, Edition 3, CRC Press, Boca Raton, FL.
4) Akazawa, T. (1943) New test method for evaluating internal stress due to compression of concrete: the splitting tension test. J Japan Soc Civil Eng 29: 777-787.
5) Akazawa, T. (1953) International association of testing and research laboratories for materials and structures, RILEM Bull; 13:13-23.
6) Au, F. T. K., Leung, C. Y. C., Zeng, Y. (2012) Analysis of in-situ stitches in precast concrete segmental bridges, IES Journal Part A: Civil & Structural Engineering, Vol. 5, No. 1, pp. 1-15.
7) Backers and Tobias (2004) Fracture toughness determination and micromechanics of rock under Mode I and Mode II loading. Diss. Postdam.
8) Barenblatt, G. I. (1959) The formation of equilibrium cracks during brittle fracture. General ideas and hypotheses. Axially symmetric rocks. *Journal of Applied Mathematics and Mechanics*, 23(3): 434-444.
9) Brooks, Z. (2010) *A Nanomechanical Investigation of the Crack Tip Process Zone of Marble*. SM. Thesis. Massachusetts Institute of Technology.
10) Brooks, Z. (2013) *Fracture Process Zone: Microstructure and Nanomechanics in Quaisi-brittle Materials*. PhD. Thesis. Massachusetts Institute of Technology.
11) Carneiro, FLLB (1943) A new method to determine the tensile strength of concrete. In: paper presented at the Proceedings of the 5th meeting of the Brazilian Association for Technical Rules ('Associacao Brasileire de Normas Tecnicas – ABNT'). 3d. section.
12) Carneiro, F. and Barcellos, A. (1953) International association of testing and research laboratories for materials and structures. RILEM Bull; 13:99-125.
13) Connor, J. J. and Faraji, S. (2012) *Fundamentals of Structural Engineering*, 1st edition, Springer, New York, pp. 443-462.

14) Demkowicz, M. J. (2012) Lecture 19: Brittle Fracture. *Lecture notes: 3.22 Mechanical Behavior of Materials*, Massachusetts Institute of Technology.

15) Demkowicz, M. J. (2012) Lecture 20: Linear Elastic Fracture Mechanics. *Lecture notes: 3.22 Mechanical Behavior of Materials*, Massachusetts Institute of Technology.

16) Dugdale, D. S. (1960) Yielding of steel sheets containing slits. *Journal of Mechanics and Physics of Solids*, 8: 100-104.

17) Epstein, B. (1948) Statistical aspects of fracture problems, *Journal of Applied Physics*, Vol. 19, pp. 140-147.

18) Einstein, H. H., Baecher, G. B., Hirschfeld, R. C. (1970) The effect of size on the strength of brittle rock, *Proceedings of 2nd International Congress on Rock Mechanics*, Belgrade.

19) Einstein, H. H. and Baecher, G. B. (1981) Size effect in rock testing, *Geophysical Research Letters*, Vol. 8, No. 7, Pages 671-674.

20) Einstein, H. H. (2015) *Lecture notes: 1.381 Rock Mechanics*, Massachusetts Institute of Technology.

21) Evans, B. (2015) Lecture 5: Brief review of mechanical properties of rocks, Lecture Notes: 12.533 Rock Physics, Massachusetts Institute of Technology.

22) Fowler, D. W. and Hsu, M. (1985) *Creep and Fatigue of Polymer Concrete*, Publication SP – American Concrete Institute, pp. 323-341.

23) Germaine, J. T., Einstein, H. H., Rudolph, S. (2015) Personal Communication.

24) Germaine, J. T. and Germaine, A. V. (2009) *Geotechnical Laboratory Measurements for Engineers*, John Wiley & Sons.

25) Glucklich, J. and Cohen, L. J. (1967) Size as a factor in the brittle-ductile transition and the strength of some materials, *International Journal of Fracture Mechanics*, Dec, pp. 278-289.

26) Glucklich, J. and Cohen, L. J. (1968) Strain energy and size effects in a brittle material, *Materials Research and Standards*, Vol 8 No. 10, pp. 17-22.

27) Griffith, A. A. (1921) The phenomena of rupture and flow in solids, Philosophical Transactions of the Royal Society of London, Series A (containing papers of a mathematical or physical character), pp. 163-198.

28) Griffith, A. A. (1924) Theory of rupture. *Proc. 1st Int. Congr. Appl. Mech.*, 55-63.

29) Guan, J. (2013) Conventional Brazilian tests, *Presentation slides: CIVL 2102 Engineering Geology and Rock Mechanics*, the University of Hong Kong.

30) Hoek, E. (1968) Brittle failure of rock, *Chapter 4 in Rock Mechanics in Engineering Practice*, ed. Stagg and Zienkiewicz, J. Wiley and Sons, London, pp. 99-124.

31) Hoek, E. and Brown, E. T. (1980) Empirical strength criterion for rock masses. *Journal of Geotechnical Engineering Divisions*. ASCE 106, 1013-1035.

32) Hoek, E. and Brown, E. T. (1980) Underground excavations in rock. The Institute of Mining and Metallurgy, London.

33) Hong Kong Buildings Department (2013) *Code of Practice for Structural Use of Concrete 2013*, Hong Kong.

34) Irwin, G. R. (1957) Analysis of stresses and strains near the end of a crack traversing a plate. *Journal of Applied Mechanics*, (24): 361-364.

35) Irwin, G. R. (1958) Discussion. *Journal of Applied Mechanics*, 25(2): 299-303.

36) Irwin, G. R. (1960) Plastic zone near a crack and fracture toughness. *Proceedings of the Seventh Sagamore Ordnance Materials Research Conference: Mechanical and Metallurgical Behavior of Sheet Materials*, pages IV63-78.

37) ISRM (1978) Suggested methods for determining tensile strength of rock materials. *International Journal of Rock Mechanics and Mining Sciences & Geomechanics Abstracts*, 15: 99-103.

38) Keles, C. and Tutluoglu, L. (2011) Investigation of proper specimen geometry for Mode I fracture toughness testing with flattened Brazilian disc method. *International Journal of Fracture*, 169: 61-75.

39) Kwan, A. K. H., Au, F. T. K., Chau, S. L. (2004) Theoretical study on effect of confinement on flexural ductility of normal and high-strength concrete beams, *Magazine of Concrete Research*, Vol. 56, No. 5, pp. 299-309.

40) Kwan, A. K. H. (2006) *Concrete Code Handbook: An Explanatory Handbook to the Code of Practice for Structural Use of Concrete 2004*, Structural Division, Hong Kong Institute of Engineers, Hong Kong.

41) Kwan, A. K. H. (2012) *Lecture notes: CIVL 1013 Engineering Mechanics and Materials*, the University of Hong Kong.

42) Leguillon, D., Martin, E., Lafarie-Frenot, M. C. (2015) Flexural vs tensile strength in brittle materials, *Comptes Rendus – Mecanique*, Vol. 343, Issue 4, pp. 275-281.

43) Morgan, S. P. (2011) *The Effect of Complex Inclusion Geometries on Fracture and Crack Coalescence Behavior in Brittle Material*. SM. Thesis. Massachusetts Institute of Technology.

44) Morgan, S. P. (2015) *An Experimental and Numerical Study on the Fracturing Processes in Opalinus Shale*. PhD. Thesis. Massachusetts Institute of Technology.

45) Muskhelishvili, N. I. (1963) *Some Basic Problems of the Mathematical Theory of Elasticity*, 2nd English edition, Springer Science, BV.

46) Pei, J. (2008) *Strength of Transversely Isotropic Rocks*. PhD. Thesis. Massachusetts Institute of Technology.

47) Swamy, R. N. (1971) Dynamic Poisson's ratio of Portland cement paste, mortar and concrete, *Cement and Concrete Research*, Vol. 1, pp. 559-583.

48) Timoshenko, S. and Goodier, J. N. (1970) *Theory of Elasticity*. New York: McGraw-Hill.

49) Trollope, D. H. and Brown, E. T. (1965) Pressure distribution in some discontinua, *Water Power*, August.

50) Trollope, D. H. and Brown, E. T. (1966) Effective stress criteria of failure of rock masses, Proceedings, 1st International Congress on Rock Mechanics, Lisbon, 1, 515.

51) Ulm, F. J., Bernand, O., Lemarchand, E. (2003) A multiscale micromechanics – hydration model for the early-aged elastic properties of cement-based materials, *Cement and Concrete Research*, No. 33, pp. 1293-1309.

52) Wang, Q. Z. and Xing, L. (1999) Determination of fracture toughness K_{IC} by using the flattened Brazilian disk specimen for rocks. *Engineering Fracture Mechanics*, 64: 193-201.

53) Wang, Q. Z., Jia, X. M., Kou, S. Q., Zhang, Z. X., Lindqvist, P. A. (2004) The flattened Brazilian disc specimen used for testing elastic modulus, tensile strength and fracture toughness of brittle rocks: analytical and numerical results. *International Journal of Rock Mechanics and Mining Sciences*, 41: 245-253.

54) Wang, Q. Z., Wu, L. Z. (2004) The flattened Brazilian disc specimen used for determining elastic modulus, tensile strength and fracture toughness of brittle rocks: experimental results. *International Journal of Rock Mechanics and Mining Sciences*, 41(3):1-5.

55) Weibull, W. (1939) A statistical theory of the strength of materials, Ingeniorsvetenskapakademiens Handlingar, Nr. 151, pp. 5-45.

56) Weibull, W. (1951) A statistical distribution function of wide applicability, Proceedings of the annual meeting of ASME in 1951, No. 51-A6.

57) Westergaard, H. M. (1939) Bearing pressures and carcks. *Journal of Applied Mechanics*, 61: A39-A53.

58) Whitney, J. M. and Knight, M. (1980) The relationship between tensile strength and flexure strength in fiber-reinforced composites, *Experimental Mechanics*, Vol. 20, Issue 6, July 1980, pp. 211-216.

59) Whittaker, B. N., Singh, R. N., Sun, G. (1992) *Rock Fracture Mechanics: Principles, Design and Applications*. Elsevier, Amsterdam.

60) Wong, L. N. Y. and Li, D. (2013) The Brazilian disc test for rock mechanics applications: review and new insights. *Rock Mechanics and Rock Engineering*, 46: 269-287.

61) Wright, P. J. F. (1955) Comments on an indirect tensile test on concrete cylinders, *Magazine of Concrete Research*, July 1955, pp. 87-96.

62) Yang, J. (2012) Lecture 5: Rock testing techniques, *Lecture notes: CIVL 2012 Engineering Geology and Rock Mechanics*, the University of Hong Kong.

63) Young, B., Ellobody, E., Feng, R. (2014) *Finite Element Analysis and Design of Metal Structures*, Waltham, MA: Butterworth – Heinemann.

64) Zhang, X. L., Kou, S. Q., Lindqvist, P. A., Yu, Y. (1998) *The relationship between the fracture toughness and tensile strength of rock. Strength Theories: Application, Development and Prospects for 21st Century*. Science Press, Beijing, 215-219.

Appendix A Experimental Results

In this appendix, the experimental results of all the seven batches of mortar will be presented.

Table A.1 Experimental results for the two-inch specimens for the first batch of mortar (The extensometer displacement was averaged from two measured displacements)

Experimental results for two-inch specimen							
Items	No.1	No.2	No.3	No.4	No.5	Mean	SD
Gauge length (mm)	25.4	25.4	25.4	25.4	25.4	25.4	0
Angle 2a	28.21	27.77	27.77	27.77	28.26	27.96	0.23
Specimen Diameter D (mm)	50.55	50.80	50.80	50.80	50.80	50.75	0.10
Specimen Thickness t (mm)	26.72	26.04	26.06	25.48	26.62	26.18	0.45
P_B (kN)	10.64	7.71	7.76	9.57	7.21	8.58	1.31
P_A (kN)	11.99	8.39	9.44	10.43	8.98	9.85	1.26
E (GPa)	**16.40**	**14.60**	**13.20**	**14.80**	**18.35**	**15.47**	**1.76**
σ_t (MPa)	**5.33**	**3.73**	**4.20**	**4.64**	**3.99**	**4.38**	**0.56**
σ_A (MPa)	**36.43**	**26.45**	**29.71**	**33.57**	**27.21**	**30.67**	**3.81**
σ_B (MPa)	**32.33**	**24.29**	**24.43**	**30.81**	**21.83**	**26.74**	**4.08**
K_{ICA} (MPam$^{0.5}$)	**2.82**	**2.02**	**2.27**	**2.57**	**2.12**	**2.36**	**0.30**
K_{ICB} (MPam$^{0.5}$)	**2.50**	**1.86**	**1.87**	**2.36**	**1.70**	**2.06**	**0.31**
Extensometer displacement (mm)	0.0302	0.0239	0.0359	0.0291	0.0190	0.0276	0.00577

Note: SD means standard deviation. σ_A represents the *averaged compressive stress* acting on the flattened surfaces at point A (see Figure 5.6), σ_B represents the *averaged compressive stress* acting on the flattened surfaces at point B (see Figure 5.6), σ_t represents the *magnitude of tensile strength*, K_{ICA} represents the *fracture toughness* based on P_A, and K_{ICB} represents the *fracture toughness* based on P_B.

Table A.2 Experimental results for the three-inch specimens for the first batch of mortar

Experimental results for three-inch specimen						
Items	No.1	No.2	No.3	No.4	Mean	SD
Gauge length (mm)	38.1	38.1	38.1	38.1	38.1	0
Angle 2a	26.02	28.26	28.45	22.29	26.26	2.48
Specimen Diameter D (mm)	76.44	75.95	76.48	76.20	76.27	0.21
Specimen Thickness t (mm)	36.93	36.86	37.41	37.39	37.15	0.26
P_B (kN)	13.72	14.90	13.72	14.59	14.24	0.52
P_A (kN)	18.01	16.92	15.19	17.22	16.83	1.03
E (GPa)	**16.90**	**15.60**	**16.10**	**17.45**	**16.51**	**0.71**
σ_t (MPa)	**3.60**	**3.38**	**3.04**	**3.44**	**3.37**	**0.20**
σ_A (MPa)	**28.34**	**24.76**	**21.61**	**31.27**	**26.49**	**3.65**
σ_B (MPa)	**21.60**	**21.81**	**19.52**	**26.49**	**22.35**	**2.55**
K_{ICA} (MPam$^{0.5}$)	**2.49**	**2.36**	**2.08**	**2.36**	**2.32**	**0.15**
K_{ICB} (MPam$^{0.5}$)	**1.90**	**2.08**	**1.88**	**2.00**	**1.96**	**0.08**
Extensometer displacement (mm)	0.0294	0.0298	0.0259	0.0269	0.0280	0.0016

Table A.3 Experimental results for the four-inch specimens for the first batch of mortar

Experimental results for four-inch specimen							
Items	No.1	No.2	No.3	No.4	No.5	Mean	SD
Gauge length (mm)	50.8	50.8	50.8	50.8	50.8	50.8	0
Angle 2a	27.41	27.92	28.29	27.70	28.29	27.92	0.34
Specimen Diameter D (mm)	101.85	101.09	101.85	101.35	101.85	101.60	0.32
Specimen Thickness t (mm)	45.62	49.20	46.71	50.24	50.50	48.45	1.95
P_B (kN)	20.40	24.71	24.75	25.83	25.31	24.20	1.94
P_A (kN)	25.03	28.30	27.75	29.45	27.59	27.62	1.45
E (Gpa)	**15.35**	**16.95**	**14.95**	**16.70**	**16.00**	**15.99**	**0.76**
σ_t (Mpa)	**2.81**	**3.17**	**3.11**	**3.30**	**3.09**	**3.10**	**0.16**
σ_A (MPa)	**22.74**	**23.59**	**23.87**	**24.17**	**21.95**	**23.27**	**0.81**
σ_B (MPa)	**18.53**	**20.60**	**21.29**	**21.19**	**21.14**	**20.35**	**1.00**
K_{ICA} (MPam$^{0.5}$)	**2.43**	**2.56**	**2.63**	**2.60**	**2.42**	**2.53**	**0.09**
K_{ICB} (MPam$^{0.5}$)	**1.98**	**2.23**	**2.35**	**2.28**	**2.22**	**2.21**	**0.12**
Extensometer displacement (mm)	0.0334	0.0341	0.0379	0.0359	0.0351	0.0353	0.0016

Table A.4 Summary of experimental results for the first batch of mortar

Size	Mean E (GPa)	SD of E (GPa)	Mean of σ_t (MPa)	SD of σ_t (MPa)	Mean of σ_A (MPa)	SD of σ_A (MPa)	Mean of σ_B (MPa)	SD of σ_B (MPa)
2-inch	15.47	1.76	4.38	0.56	30.67	3.81	26.74	4.08
3-inch	16.51	0.71	3.37	0.20	26.49	3.65	22.35	2.55
4-inch	15.99	0.76	3.10	0.16	23.27	0.81	20.35	1.00

Table A.5 Summary of experimental results for the first batch of mortar

Size	Mean of K_{ICA} ($MPam^{0.5}$)	SD of K_{ICA} ($MPam^{0.5}$)	Mean of K_{ICB} ($MPam^{0.5}$)	SD of K_{ICB} ($MPam^{0.5}$)
2-inch	2.36	0.30	2.06	0.31
3-inch	2.32	0.15	1.96	0.08
4-inch	2.53	0.09	2.21	0.12

Table A.6 Experimental results for two-inch specimens for the second batch of mortar

Experimental results for two-inch specimen							
Items	No.1	No.2	No.3	No.4	No.5	Mean	SD
Gauge length (mm)	25.4	25.4	25.4	25.4	25.4	25.4	0
Angle 2a	29.5	28.39	27.82	28.81	28.69	28.64	0.55
Specimen Diameter D (mm)	50.88	50.80	50.98	50.55	50.62	50.76	0.16
Specimen Thickness t (mm)	26.85	24.79	26.16	26.16	26.31	26.06	0.68
P_B (kN)	10.68	7.86	7.47	6.30	9.02	8.266	1.49
P_A (kN)	11.74	9.23	9.24	9.14	10.33	9.936	1.00
E (GPa)	**20.50**	**18.10**	**19.70**	**18.45**	**19.40**	**19.23**	**0.87**
σ_t (MPa)	**5.22**	**4.10**	**4.11**	**4.06**	**4.59**	**4.42**	**0.45**
σ_A (MPa)	**33.76**	**29.89**	**28.82**	**27.79**	**31.30**	**30.31**	**2.08**
σ_B (MPa)	**30.71**	**25.45**	**23.30**	**19.15**	**27.33**	**25.19**	**3.88**
K_{ICA} ($MPam^{0.5}$)	**2.74**	**2.34**	**2.21**	**2.20**	**2.47**	**2.39**	**0.20**
K_{ICB} ($MPam^{0.5}$)	**2.49**	**1.99**	**1.79**	**1.51**	**2.15**	**1.99**	**0.33**
Extensometer displacement (mm)	0.0232	0.0206	0.0191	0.0201	0.0217	0.0209	0.00141

Table A.7 Experimental results for three-inch specimens for the second batch of mortar

Experimental results for three-inch specimen							
Items	No.1	No.2	No.3	No.4	No.5	Mean	SD
Gauge length (mm)	38.1	38.1	38.1	38.1	38.1	38.1	0
Angle 2a	28.29	28.08	28.61	28.71	29.75	28.69	0.58
Specimen Diameter D (mm)	76.28	76.20	76.40	75.95	76.20	76.21	0.15
Specimen Thickness t (mm)	37.11	37.47	37.21	37.54	38.15	37.50	0.36
P_B (kN)	18.64	17.92	15.15	21.47	19.32	18.50	2.05
P_A (kN)	19.12	19.09	16.58	23.03	19.99	19.56	2.07
E (GPa)	**15.00**	**14.80**	**14.90**	**14.70**	**13.55**	**14.59**	**0.53**
σ_t (MPa)	**3.82**	**3.81**	**3.31**	**4.60**	**3.99**	**3.91**	**0.41**
σ_A (MPa)	**27.64**	**27.57**	**23.61**	**32.58**	**26.79**	**27.64**	**2.88**
σ_B (MPa)	**29.95**	**25.88**	**21.57**	**30.38**	**25.89**	**26.13**	**2.82**
K_{ICA} (MPam$^{0.5}$)	**2.64**	**2.61**	**2.28**	**3.15**	**2.68**	**2.67**	**0.28**
K_{ICB} (MPam$^{0.5}$)	**2.57**	**2.45**	**2.08**	**2.93**	**2.59**	**2.53**	**0.27**
Extensometer displacement (mm)	0.0350	0.0354	0.0306	0.0429	0.0404	0.0369	0.0043

Table A.8 Experimental results for four-inch specimens for the second batch of mortar

Experimental results for four-inch specimen							
Items	No.1	No.2	No.3	No.4	No.5	Mean	SD
Gauge length (mm)	50.8	50.8	50.8	50.8	50.8	50.8	0
Angle 2a	25.53	28.04	25.48	27.32	26.02	26.48	1.03
Specimen Diameter D (mm)	101.04	101.19	101.35	101.24	101.75	101.32	0.24
Specimen Thickness t (mm)	51.46	53.21	53.11	52.93	53.39	52.82	0.70
P_B (kN)	27.58	25.25	25.72	22.35	31.83	26.55	3.13
P_A (kN)	31.33	28.42	28.17	24.12	34.61	29.33	3.50
E (GPa)	**19.50**	**18.90**	**19.75**	**19.10**	**20.70**	**19.59**	**0.63**
σ_t (MPa)	**3.51**	**3.18**	**3.16**	**2.70**	**3.88**	**3.29**	**0.39**
σ_A (MPa)	**27.27**	**21.79**	**23.73**	**19.06**	**28.30**	**24.03**	**3.43**
σ_B (MPa)	**24.01**	**19.36**	**21.67**	**17.66**	**26.03**	**21.75**	**3.03**
K_{ICA} (MPam$^{0.5}$)	**2.71**	**2.37**	**2.36**	**2.03**	**2.87**	**2.47**	**0.30**
K_{ICB} (MPam$^{0.5}$)	**2.38**	**2.11**	**2.15**	**1.88**	**2.64**	**2.23**	**0.26**
Extensometer displacement (mm)	0.0324	0.0305	0.0289	0.0257	0.0339	0.0303	0.0029

Table A.9 Summary of experimental results for the second batch of mortar

Size	Mean E (GPa)	SD of E (GPa)	Mean of σ_t (MPa)	SD of σ_t (MPa)	Mean of σ_A (MPa)	SD of σ_A (MPa)	Mean of σ_B (MPa)	SD of σ_B (MPa)
2-inch	19.23	0.87	4.42	0.45	30.31	2.08	25.19	3.88
3-inch	14.59	0.53	3.91	0.41	27.64	2.88	26.13	2.82
4-inch	19.59	0.63	3.29	0.39	24.03	3.43	21.75	3.03

Table A.10 Summary of experimental results for the second batch of mortar

Size	Mean of K_{ICA} ($MPam^{0.5}$)	SD of K_{ICA} ($MPam^{0.5}$)	Mean of K_{ICB} ($MPam^{0.5}$)	SD of K_{ICB} ($MPam^{0.5}$)
2-inch	2.39	0.20	1.99	0.33
3-inch	2.67	0.28	2.53	0.27
4-inch	2.47	0.30	2.23	0.26

Table A.11 Experimental results for two-inch specimens for the third batch of mortar

Experimental results for two-inch specimen							
Items	No.1	No.2	No.3	No.4	No.5	Mean	SD
Gauge length (mm)	25.4	25.4	25.4	25.4	25.4	25.4	0
Angle 2a	28.23	26.54	27.72	28.66	28.29	27.89	0.74
Specimen Diameter D (mm)	50.77	50.65	50.62	50.57	50.83	50.69	0.10
Specimen Thickness t (mm)	26.85	26.14	26.62	26.80	26.77	26.63	0.26
P_B (kN)	9.82	8.80	10.35	10.56	10.90	10.09	0.73
P_A (kN)	10.96	10.10	12.31	11.05	11.99	11.28	0.79
E (GPa)	**20.70**	**20.10**	**20.90**	**21.20**	**18.80**	**20.34**	**0.85**
σ_t (MPa)	**4.87**	**4.49**	**5.47**	**4.91**	**5.33**	**5.01**	**0.35**
σ_A (MPa)	**32.97**	**33.24**	**38.14**	**32.95**	**36.06**	**34.67**	**2.09**
σ_B (MPa)	**29.54**	**28.96**	**32.07**	**31.49**	**32.78**	**30.97**	**1.47**
K_{ICA} ($MPam^{0.5}$)	**2.56**	**2.43**	**2.91**	**2.59**	**2.81**	**2.66**	**0.17**
K_{ICB} ($MPam^{0.5}$)	**2.30**	**2.12**	**2.44**	**2.48**	**2.55**	**2.38**	**0.16**
Extensometer displacement (mm)	0.0214	0.0204	0.0237	0.0210	0.0259	0.0225	0.0020

Table A.12 Experimental results for three-inch specimens for the third batch of mortar

Experimental results for three-inch specimen							
Items	No.1	No.2	No.3	No.4	No.5	Mean	SD
Gauge length (mm)	38.1	38.1	38.1	38.1	38.1	38.1	0
Angle 2a	28.83	27.94	28.20	28.25	28.18	28.28	0.30
Specimen Diameter D (mm)	76.28	76.02	75.97	75.97	76.23	76.09	0.13
Specimen Thickness t (mm)	41.15	41.50	40.26	41.81	42.09	41.36	0.63
P_B (kN)	20.69	20.93	18.19	18.60	18.61	19.40	1.16
P_A (kN)	21.17	22.10	18.84	19.71	20.03	20.37	1.14
E (GPa)	**16.60**	**17.45**	**14.95**	**18.85**	**17.50**	**17.07**	**1.28**
σ_t (MPa)	**4.23**	**4.42**	**3.76**	**3.94**	**4.06**	**4.08**	**0.23**
σ_A (MPa)	**27.10**	**29.02**	**25.29**	**25.43**	**25.65**	**26.50**	**1.42**
σ_B (MPa)	**26.48**	**27.48**	**24.42**	**24.00**	**23.83**	**25.24**	**1.47**
K_{ICA} (MPam$^{0.5}$)	**2.63**	**2.73**	**2.40**	**2.42**	**2.44**	**2.52**	**0.13**
K_{ICB} (MPam$^{0.5}$)	**2.57**	**2.59**	**2.32**	**2.28**	**2.26**	**2.41**	**0.14**
Extensometer displacement (mm)	0.0350	0.0347	0.0345	0.0287	0.0315	0.0329	0.0024

Table A.13 Experimental results for four-inch specimens for the third batch of mortar

Experimental results for four-inch specimen							
Items	No.1	No.2	No.3	No.4	No.5	Mean	SD
Gauge length (mm)	50.8	50.8	50.8	50.8	50.8	50.8	0
Angle 2a	28.7	28.43	29.72	28.21	29.38	28.89	0.57
Specimen Diameter D (mm)	101.09	102.01	101.63	102.01	101.73	101.69	0.34
Specimen Thickness t (mm)	51.79	53.62	51.77	50.69	52.73	52.12	0.99
P_B (kN)	23.59	27.62	29.00	29.32	22.56	26.42	2.81
P_A (kN)	25.94	29.46	30.98	31.32	25.33	28.61	2.51
E (GPa)	**19.20**	**19.30**	**18.15**	**18.00**	**21.55**	**19.24**	**1.27**
σ_t (MPa)	**2.91**	**3.30**	**3.47**	**3.51**	**2.84**	**3.21**	**0.28**
σ_A (MPa)	**19.99**	**21.94**	**22.97**	**24.86**	**18.62**	**21.68**	**2.19**
σ_B (MPa)	**18.18**	**20.57**	**21.50**	**23.27**	**16.59**	**20.02**	**2.38**
K_{ICA} (MPam$^{0.5}$)	**2.23**	**2.43**	**2.65**	**2.74**	**2.13**	**2.44**	**0.23**
K_{ICB} (MPam$^{0.5}$)	**2.03**	**2.28**	**2.49**	**2.56**	**1.90**	**2.25**	**0.26**
Extensometer displacement (mm)	0.0274	0.0311	0.0348	0.0355	0.0239	0.0305	0.0044

Table A.14 Summary of experimental results for the third batch of mortar

Size	Mean E (GPa)	SD of E (GPa)	Mean of σ_t (MPa)	SD of σ_t (MPa)	Mean of σ_A (MPa)	SD of σ_A (MPa)	Mean of σ_B (MPa)	SD of σ_B (MPa)
2-inch	20.34	0.85	5.01	0.35	34.67	2.09	30.97	1.47
3-inch	17.07	1.28	4.08	0.23	26.50	1.42	25.24	1.47
4-inch	19.24	1.27	3.21	0.28	21.68	2.19	20.02	2.38

Table A.15 Summary of experimental results for the third batch of mortar

Size	Mean of K_{ICA} ($MPam^{0.5}$)	SD of K_{ICA} ($MPam^{0.5}$)	Mean of K_{ICB} ($MPam^{0.5}$)	SD of K_{ICB} ($MPa{\cdot}m^{0.5}$)
2-inch	2.66	0.17	2.38	0.16
3-inch	2.52	0.13	2.41	0.14
4-inch	2.44	0.23	2.25	0.26

Table A.16 Experimental results for the two-inch specimens for the fourth batch of mortar

Experimental results for two-inch specimen							
Items	No.1	No.2	No.3	No.4	No.5	Mean	SD
Gauge length (mm)	25.4	25.4	25.4	25.4	25.4	25.4	0
Angle 2a	39.08	40.86	40.85	37.81	40.79	39.88	1.24
Specimen Diameter D (mm)	50.80	51.23	50.60	50.83	50.95	50.88	0.21
Specimen Thickness t (mm)	27.05	27.31	27.20	27.28	27.23	27.21	0.09
P_B (kN)	13.36	14.33	12.49	14.00	14.50	13.74	0.73
P_A (kN)	13.82	14.45	12.58	14.54	14.71	14.02	0.78
P_D (kN)	13.28	13.30	9.89	13.83	13.32	12.72	1.43
E (GPa)	**19.60**	**17.55**	**19.15**	**18.85**	**17.80**	**18.59**	**0.79**
σ_t (MPa)	**5.28**	**5.29**	**3.93**	**5.50**	**5.30**	**5.06**	**0.57**
σ_A (MPa)	**30.07**	**29.60**	**26.19**	**32.37**	**30.43**	**29.73**	**2.01**
σ_B (MPa)	**29.07**	**29.35**	**26.00**	**31.17**	**29.99**	**29.12**	**1.72**
K_{ICA} ($MPam^{0.5}$)	**3.21**	**3.31**	**2.91**	**3.34**	**3.38**	**3.23**	**0.17**
K_{ICB} ($MPam^{0.5}$)	**3.10**	**3.28**	**2.89**	**3.22**	**3.34**	**3.16**	**0.16**
End-to-end displacement (mm)	0.0253	0.0304	0.0240	0.0281	0.0300	0.0276	0.0025

Note: P_D is the loading at point D where the specimen starts to deform nonlinearly (see Figure 5.9). σ_t is calculated based on P_D instead of P_C (it is discussed in 5.3.2).

Table A.17 Experimental results for the three-inch specimens for the fourth batch of mortar

Experimental results for three-inch specimen							
Items	No.1	No.2	No.3	No.4	No.5	Mean	SD
Gauge length (mm)	38.1	38.1	38.1	38.1	38.1	38.1	0
Angle 2a	39.41	39.30	39.74	38.53	38.14	39.02	0.59
Specimen Diameter D (mm)	76.25	76.23	76.50	76.07	76.71	76.35	0.23
Specimen Thickness t (mm)	39.57	39.14	39.60	39.52	39.40	39.45	0.17
P_B (kN)	24.38	23.52	21.92	23.76	21.23	22.96	1.19
P_A (kN)	24.92	24.16	22.27	24.54	22.23	23.62	1.15
P_D (kN)	21.92	22.65	17.32	22.61	20.31	20.96	2.05
E (GPa)	**18.40**	**17.25**	**14.20**	**17.15**	**14.60**	**16.32**	**1.63**
σ_t (MPa)	**3.88**	**4.01**	**3.09**	**4.00**	**3.93**	**3.78**	**0.35**
σ_A (MPa)	**24.50**	**24.08**	**21.63**	**24.74**	**22.52**	**23.49**	**1.21**
σ_B (MPa)	**23.96**	**23.45**	**21.29**	**23.95**	**21.50**	**22.83**	**1.19**
K_{ICA} (MPam$^{0.5}$)	**3.23**	**3.16**	**2.88**	**3.18**	**2.88**	**3.07**	**0.15**
K_{ICB} (MPam$^{0.5}$)	**3.16**	**3.08**	**2.83**	**3.08**	**2.75**	**2.98**	**0.16**
Extensometer displacement (mm)	0.0327	0.0337	0.0378	0.0345	0.0366	0.0351	0.0019

Table A.18 Experimental results for the four-inch specimens for the fourth batch of mortar

Experimental results for four-inch specimen							
Items	No.1	No.2	No.3	No.4	No.5	Mean	SD
Gauge length (mm)	50.8	50.8	50.8	50.8	50.8	50.8	0
Angle 2a	39.47	38.39	38.40	40.07	38.33	38.93	0.71
Specimen Diameter D (mm)	101.63	101.73	102.16	101.90	102.54	101.99	0.33
Specimen Thickness t (mm)	51.84	51.66	51.87	51.94	51.97	51.86	0.11
P_B (kN)	34.00	29.03	32.25	32.99	33.05	32.26	1.71
P_A (kN)	35.37	30.97	33.12	33.08	34.11	33.33	1.45
P_D (kN)	35.37	28.91	30.92	30.59	32.40	31.64	2.17
E (GPa)	**21.35**	**20.20**	**16.55**	**18.65**	**17.25**	**18.80**	**1.79**
σ_t (MPa)	**3.53**	**2.88**	**3.08**	**3.05**	**3.23**	**3.15**	**0.22**
σ_A (MPa)	**19.88**	**17.93**	**19.01**	**18.24**	**19.50**	**18.91**	**0.74**
σ_B (MPa)	**19.11**	**16.80**	**18.51**	**18.19**	**18.89**	**18.30**	**0.82**
K_{ICA} (MPam$^{0.5}$)	**3.03**	**2.66**	**2.83**	**2.82**	**2.90**	**2.85**	**0.12**
K_{ICB} (MPam$^{0.5}$)	**2.91**	**2.49**	**2.75**	**2.81**	**2.81**	**2.75**	**0.14**
Extensometer displacement (mm)	0.0296	0.0274	0.0358	0.0317	0.0353	0.0319	0.0033

Table A.19 Summary of the experimental results of the fourth batch of mortar

Size	Mean E (GPa)	SD of E (GPa)	Mean of σ_t (MPa)	SD of σ_t (MPa)	Mean of σ_A (MPa)	SD of σ_A (MPa)	Mean of σ_B (MPa)	SD of σ_B (MPa)
2-inch	18.59	0.79	5.06	0.57	29.73	2.01	29.12	1.72
3-inch	16.32	1.63	3.78	0.35	23.49	1.21	22.83	1.19
4-inch	18.80	1.79	3.15	0.22	18.91	0.74	18.30	0.82

Table A.20 Summary of experimental results for the fourth batch of mortar

Size	Mean of K_{ICA} ($MPam^{0.5}$)	SD of K_{ICA} ($MPam^{0.5}$)	Mean of K_{ICB} ($MPam^{0.5}$)	SD of K_{ICB} ($MPam^{0.5}$)
2-inch	3.23	0.17	3.16	0.16
3-inch	3.07	0.15	2.98	0.16
4-inch	2.85	0.12	2.75	0.14

Table A.21 Experimental results for the two-inch specimens for the fifth batch of mortar

Experimental results for two-inch specimen							
Items	No.1	No.2	No.3	No.4	No.5	Mean	SD
Gauge length (mm)	25.4	25.4	25.4	25.4	25.4	25.4	0
Angle 2a	40.82	40.18	41.24	40.10	41.05	40.68	0.46
Specimen Diameter D (mm)	50.67	50.85	50.98	50.62	50.98	50.82	0.15
Specimen Thickness t (mm)	26.75	27.08	27.05	27.15	27.00	27.01	0.139
P_B (kN)	9.88	11.74	9.96	14.44	13.84	11.97	1.900
P_A (kN)	10.26	11.97	10.00	14.78	14.45	12.29	2.017
P_D (kN)	8.74	9.90	8.68	13.74	12.39	10.69	2.03
E (GPa)	**20.40**	**21.20**	**15.00**	**17.95**	**19.00**	**18.71**	**2.17**
σ_t (MPa)	**3.48**	**3.94**	**3.47**	**5.47**	**4.94**	**4.26**	**0.81**
σ_A (MPa)	**21.71**	**25.31**	**20.59**	**31.37**	**29.95**	**25.79**	**4.30**
σ_B (MPa)	**20.91**	**24.83**	**20.51**	**30.64**	**28.68**	**25.11**	**4.06**
K_{ICA} ($MPam^{0.5}$)	**2.41**	**2.77**	**2.32**	**3.42**	**3.35**	**2.85**	**0.46**
K_{ICB} ($MPam^{0.5}$)	**2.32**	**2.72**	**2.31**	**3.34**	**3.21**	**2.78**	**0.43**
Extensometer displacement (mm)	0.0182	0.0204	0.0240	0.0298	0.0275	0.0240	0.004

Table A.22 Experimental results for the three-inch specimens for the fifth batch of mortar

Experimental results for three-inch specimen							
Items	No.1	No.2	No.3	No.4	No.5	Mean	SD
Gauge length (mm)	38.1	38.1	38.1	38.1	38.1	38.1	0
Angle 2a	38.85	40.83	39.41	39.41	39.27	39.55	0.670
Specimen Diameter D (mm)	76.23	76.43	76.63	76.07	76.10	76.29	0.212
Specimen Thickness t (mm)	39.75	39.55	39.24	39.57	39.83	39.59	0.202
P_B (kN)	20.68	22.92	18.94	23.90	22.50	21.79	1.766
P_A (kN)	21.03	23.55	19.29	24.91	22.94	22.34	1.972
P_D (kN)	18.98	21.97	17.48	23.88	22.08	20.88	2.32
E (GPa)	**16.35**	**17.90**	**14.85**	**18.20**	**19.00**	**17.26**	**1.48**
σ_t (MPa)	**3.39**	**3.89**	**3.13**	**4.28**	**3.93**	**3.72**	**0.41**
σ_A (MPa)	**20.87**	**22.34**	**19.03**	**24.54**	**22.53**	**21.86**	**1.84**
σ_B (MPa)	**20.52**	**21.74**	**18.68**	**23.55**	**22.10**	**21.32**	**1.64**
K_{ICA} (MPam$^{0.5}$)	**2.71**	**3.05**	**2.51**	**3.23**	**2.95**	**2.89**	**0.25**
K_{ICB} (MPam$^{0.5}$)	**2.66**	**2.96**	**2.47**	**3.10**	**2.90**	**2.82**	**0.22**
Extensometer displacement (mm)	0.0310	0.0317	0.0313	0.0328	0.0290	0.0312	0.001

Table A.23 Experimental results for the four-inch specimens for the fifth batch of mortar

Calculation Results for four-inch specimen							
Items	No.1	No.2	No.3	No.4	No.5	Mean	SD
Gauge length (mm)	50.8	50.8	50.8	50.8	50.8	50.8	0
Angle 2a	37.88	37.36	38.20	38.18	37.89	37.90	0.30
Specimen Diameter D (mm)	102.46	101.73	101.68	101.73	101.78	101.87	0.30
Specimen Thickness t (mm)	53.42	53.26	52.50	49.12	54.10	52.48	1.75
P_B (kN)	32.66	29.44	27.36	32.47	43.34	33.05	5.51
P_A (kN)	32.91	30.62	28.42	33.93	45.58	34.29	5.96
P_D (kN)	28.75	28.70	26.82	31.98	42.87	31.82	5.77
E (GPa)	**19.80**	**18.80**	**16.30**	**18.05**	**20.85**	**18.76**	**1.55**
σ_t (MPa)	**2.87**	**2.86**	**2.71**	**3.19**	**4.33**	**3.19**	**0.59**
σ_A (MPa)	**18.53**	**17.65**	**16.27**	**20.76**	**25.50**	**19.74**	**3.23**
σ_B (MPa)	**18.39**	**16.97**	**15.67**	**19.87**	**24.25**	**19.03**	**2.97**
K_{ICA} (MPam$^{0.5}$)	**2.72**	**2.55**	**2.40**	**3.06**	**3.73**	**2.89**	**0.47**
K_{ICB} (MPam$^{0.5}$)	**2.70**	**2.45**	**2.31**	**2.93**	**3.55**	**2.79**	**0.44**
Extensometer displacement (mm)	0.0297	0.0290	0.0312	0.0336	0.0390	0.0325	0.004

Table A.24 Summary of the experimental results for the fifth batch of mortar

Size	Mean E (GPa)	SD of E (GPa)	Mean of σ_t (MPa)	SD of σ_t (MPa)	Mean of σ_A (MPa)	SD of σ_A (MPa)	Mean of σ_B (MPa)	SD of σ_B (MPa)
2-inch	18.71	2.17	4.26	0.81	25.79	4.30	25.11	4.06
3-inch	17.26	1.48	3.72	0.41	21.86	1.84	21.32	1.64
4-inch	18.76	1.55	3.19	0.59	19.74	3.23	19.03	2.97

Table A.25 Summary of experimental results for the fifth batch of mortar

Size	Mean of K_{ICA} ($MPam^{0.5}$)	SD of K_{ICA} ($MPam^{0.5}$)	Mean of K_{ICB} ($MPam^{0.5}$)	SD of K_{ICB} ($MPam^{0.5}$)
2-inch	2.85	0.46	2.78	0.43
3-inch	2.89	0.25	2.82	0.22
4-inch	2.89	0.47	2.79	0.44

Table A.26 Experimental results for the two-inch specimens for the sixth batch of mortar

Experimental results for two-inch specimen							
Items	No.1	No.2	No.3	No.4	No.5	Mean	SD
Gauge length (mm)	25.4	25.4	25.4	25.4	25.4	25.4	0
Angle 2a	25.24	23.77	25.07	24.19	23.12	24.28	0.795
Specimen Diameter D (mm)	50.75	50.77	50.88	50.83	51.33	50.91	0.215
Specimen Thickness t (mm)	27.15	26.97	27.00	27.25	27.13	27.10	0.103
P_B (kN)	10.62	8.81	9.25	8.11	7.25	8.81	1.131
P_A (kN)	11.42	9.48	9.90	9.44	8.40	9.73	0.980
E (GPa)	**20.55**	**18.45**	**17.70**	**21.40**	**19.85**	**19.59**	**1.35**
σ_t (MPa)	**5.27**	**4.37**	**4.56**	**4.35**	**3.87**	**4.48**	**0.45**
σ_A (MPa)	**37.93**	**33.61**	**33.21**	**32.53**	**30.10**	**33.48**	**2.54**
σ_B (MPa)	**35.28**	**31.24**	**31.03**	**27.94**	**25.98**	**30.29**	**3.18**
K_{ICA} ($MPam^{0.5}$)	**2.64**	**2.21**	**2.30**	**2.17**	**1.93**	**2.25**	**0.23**
K_{ICB} ($MPam^{0.5}$)	**2.46**	**2.05**	**2.15**	**1.87**	**1.67**	**2.04**	**0.27**
Extensometer displacement (mm)	0.0233	0.0215	0.0234	0.0183	0.0177	0.0209	0.002

Table A.27 Experimental results for the three-inch specimens for the sixth batch of mortar

Experimental results for three-inch specimen							
Items	No.1	No.2	No.3	No.4	No.5	Mean	SD
Gauge length (mm)	38.1	38.1	38.1	38.1	38.1	38.1	0
Angle 2a	23.17	24.34	22.95	22.34	22.58	23.08	0.694
Specimen Diameter D (mm)	76.38	75.97	76.56	76.45	76.43	76.36	0.202
Specimen Thickness t (mm)	40.44	40.41	40.16	40.39	40.56	40.39	0.132
P_B (kN)	16.00	16.74	16.86	16.05	15.39	16.21	0.538
P_A (kN)	17.38	18.63	19.20	18.85	16.84	18.18	0.909
E (GPa)	**16.55**	**21.30**	**17.30**	**22.75**	**14.90**	**18.56**	**2.97**
σ_t (MPa)	**3.56**	**3.81**	**3.93**	**3.86**	**3.45**	**3.72**	**0.18**
σ_A (MPa)	**28.02**	**28.79**	**31.40**	**31.52**	**27.75**	**29.49**	**1.64**
σ_B (MPa)	**25.80**	**25.87**	**27.57**	**26.84**	**25.36**	**26.29**	**0.81**
K_{ICA} (MPam$^{0.5}$)	**2.20**	**2.37**	**2.44**	**2.39**	**2.12**	**2.30**	**0.12**
K_{ICB} (MPam$^{0.5}$)	**2.02**	**2.13**	**2.15**	**2.03**	**1.94**	**2.05**	**0.07**
Extensometer displacement (mm)	0.0292	0.0243	0.0308	0.0230	0.0314	0.0277	0.003

Table A.28 Experimental results of four-inch specimen for the sixth batch of mortar

Experimental results for four-inch specimen							
Items	No.1	No.2	No.3	No.4	No.5	Mean	SD
Gauge length (mm)	50.8	50.8	50.8	50.8	50.8	50.8	0
Angle 2a	23.51	22.39	22.71	21.83	22.09	22.51	0.58
Specimen Diameter D (mm)	101.78	101.57	101.30	102.36	102.08	101.82	0.37
Specimen Thickness t (mm)	55.50	55.17	55.02	54.99	55.09	55.15	0.18
P_B (kN)	25.58	25.10	29.86	23.45	23.63	25.52	2.32
P_A (kN)	27.35	28.20	32.83	25.64	26.66	28.14	2.49
E (GPa)	**20.85**	**19.75**	**21.15**	**19.80**	**19.35**	**20.18**	**0.69**
σ_t (MPa)	**3.15**	**3.25**	**3.78**	**2.95**	**3.07**	**3.24**	**0.29**
σ_A (MPa)	**23.77**	**25.92**	**29.92**	**24.06**	**24.75**	**25.68**	**2.25**
σ_B (MPa)	**22.23**	**23.07**	**27.22**	**22.00**	**21.93**	**23.29**	**2.01**
K_{ICA} (MPam$^{0.5}$)	**2.18**	**2.27**	**2.65**	**2.06**	**2.14**	**2.26**	**0.21**
K_{ICB} (MPam$^{0.5}$)	**2.04**	**2.02**	**2.41**	**1.88**	**1.90**	**2.05**	**0.19**
Extensometer displacement (mm)	0.0271	0.0295	0.032	0.0267	0.0284	0.0287	0.002

Table A.29 Summary of the experimental results for the sixth batch of mortar

Size	Mean E (GPa)	SD of E (GPa)	Mean of σ_t (MPa)	SD of σ_t (MPa)	Mean of σ_A (MPa)	SD of σ_A (MPa)	Mean of σ_B (MPa)	SD of σ_B (MPa)
2-inch	19.59	1.35	4.48	0.45	33.48	2.54	30.29	3.18
3-inch	18.56	2.97	3.72	0.18	29.49	1.64	26.29	0.81
4-inch	20.18	0.69	3.24	0.29	25.68	2.25	23.29	2.01

Table A.30 Summary of experimental results for the sixth batch of mortar

Size	Mean of K_{ICA} ($MPam^{0.5}$)	SD of K_{ICA} ($MPam^{0.5}$)	Mean of K_{ICB} ($MPam^{0.5}$)	SD of K_{ICB} ($MPam^{0.5}$)
2-inch	2.25	0.23	2.04	0.27
3-inch	2.30	0.12	2.05	0.07
4-inch	2.26	0.21	2.05	0.19

Table A.31 Experimental results for the two-inch specimens for the seventh batch of mortar

Experimental results for two-inch specimen							
Items	No.1	No.2 (sand)	No.3 (wax)	No.4 (wax)	No.5 (sand)	Mean	SD
Gauge length (mm)	25.4	25.4	25.4	25.4	25.4	25.4	0
Angle 2a	23.86	23.41	23.37	22.77	21.32	22.95	0.884
Specimen Diameter D (mm)	51.16	51.23	50.93	50.80	50.80	50.98	0.180
Specimen Thickness t (mm)	27.23	27.03	27.13	26.92	27.20	27.10	0.114
P_B (kN)	9.70	8.10	9.90	8.60	8.85	9.03	0.676
P_A (kN)	10.80	8.70	11.20	9.70	10.24	10.13	0.876
E (GPa)	**17.80**	**20.00**	**16.65**	**19.00**	**21.40**	**18.97**	**1.66**
σ_t (MPa)	**4.98**	**4.01**	**5.16**	**4.47**	**4.72**	**4.67**	**0.40**
σ_A (MPa)	**37.51**	**30.98**	**40.03**	**35.93**	**40.06**	**36.90**	**3.36**
σ_B (MPa)	**33.69**	**28.84**	**35.39**	**31.86**	**34.62**	**32.88**	**2.34**
K_{ICA} ($MPam^{0.5}$)	**2.48**	**2.01**	**2.59**	**2.26**	**2.36**	**2.34**	**0.20**
K_{ICB} ($MPam^{0.5}$)	**2.23**	**1.87**	**2.29**	**2.00**	**2.04**	**2.09**	**0.15**
Extensometer displacement (mm)	0.0254	0.0182	0.0281	0.0214	0.0187	0.0224	0.0038

Table A.32 Experimental results for the three-inch specimens for the seventh batch of mortar

Experimental results for three-inch specimen						
Items	No.1	No.2	No.3 (wax)	No.4 (sand)	Mean	SD
Gauge length (mm)	38.1	38.1	38.1	38.1	38.1	0
Angle 2a	23.32	22.95	22.03	22.72	22.76	0.47
Specimen Diameter D (mm)	76.68	76.33	76.63	76.33	76.49	0.17
Specimen Thickness t (mm)	40.13	40.56	40.54	40.21	40.36	0.19
P_B (kN)	14.32	19.95	18.27	17.66	17.55	2.05
P_A (kN)	16.96	21.74	20.85	19.37	19.73	1.81
E (GPa)	**18.50**	**20.00**	**14.70**	**20.55**	**18.44**	**2.28**
σ_t (MPa)	**3.47**	**4.45**	**4.27**	**3.97**	**4.04**	**0.37**
σ_A (MPa)	**27.27**	**35.30**	**35.13**	**32.05**	**32.44**	**3.25**
σ_B (MPa)	**23.03**	**32.39**	**30.78**	**29.22**	**28.85**	**3.55**
K_{ICA} (MPam$^{0.5}$)	**2.16**	**2.74**	**2.63**	**2.47**	**2.50**	**0.22**
K_{ICB} (MPam$^{0.5}$)	**1.82**	**2.52**	**2.30**	**2.25**	**2.22**	**0.25**
Extensometer displacement (mm)	0.0255	0.0302	0.0395	0.0262	0.0303	0.0056

Table A.33 Experimental results for the four-inch specimens for the seventh batch of mortar

Experimental results for four-inch specimen							
Items	No.1	No.2 (wax)	No.3 (wax)	No.4 (sand)	No.5 (sand)	Mean	SD
Gauge length (mm)	50.8	50.8	50.8	50.8	50.8	50.8	0
Angle 2a	22.07	23.43	23.93	22.14	21.74	22.66	0.86
Specimen Diameter D (mm)	101.50	101.35	102.29	101.98	102.11	101.84	0.36
Specimen Thickness t (mm)	55.17	54.61	55.35	52.10	55.19	54.48	1.22
P_B (kN)	20.65	24.45	26.66	26.75	23.55	24.41	2.25
P_A (kN)	22.95	26.76	29.35	30.41	26.90	27.27	2.58
E (GPa)	**15.40**	**16.80**	**17.15**	**20.40**	**18.05**	**17.56**	**1.66**
σ_t (MPa)	**2.64**	**3.08**	**3.38**	**3.50**	**3.10**	**3.14**	**0.30**
σ_A (MPa)	**21.42**	**23.82**	**25.01**	**29.81**	**25.31**	**25.07**	**2.74**
σ_B (MPa)	**19.27**	**21.76**	**22.72**	**26.23**	**22.16**	**22.43**	**2.24**
K_{ICA} (MPam$^{0.5}$)	**1.85**	**2.18**	**2.34**	**2.59**	**2.16**	**2.22**	**0.24**
K_{ICB} (MPam$^{0.5}$)	**1.66**	**1.99**	**2.13**	**2.27**	**1.89**	**1.99**	**0.21**
Extensometer displacement (mm)	0.0308	0.0330	0.0354	0.0308	0.0308	0.0322	0.002

Table A.34 Summary of the experimental results for the seventh batch of mortar

Size	Mean E (GPa)	SD of E (GPa)	Mean of σ_t (MPa)	SD of σ_t (MPa)	Mean of σ_A (MPa)	SD of σ_A (MPa)	Mean of σ_B (MPa)	SD of σ_B (MPa)
2-inch	18.97	1.66	4.67	0.40	36.90	3.36	32.88	2.34
3-inch	18.44	2.28	4.04	0.37	32.44	3.25	28.85	3.55
4-inch	17.56	1.66	3.14	0.30	25.07	2.74	22.43	2.24

Table A.35 Summary of experimental results for the seventh batch of mortar

Size	Mean of K_{ICA} ($MPam^{0.5}$)	SD of K_{ICA} ($MPam^{0.5}$)	Mean of K_{ICB} ($MPam^{0.5}$)	SD of K_{ICB} ($MPam^{0.5}$)
2-inch	2.34	0.20	2.09	0.15
3-inch	2.50	0.22	2.22	0.25
4-inch	2.22	0.24	1.99	0.21